nagra.

Arbeitsbericht NAB 23-10

A Radionuclide Release Model for Spent UO_2 and MOX Fuel for Safety Assessment with Application to Waste to be Disposed of in a Deep Geological Repository in Switzerland

February 2023

National Cooperative
for the Disposal of
Radioactive Waste

Hardstrasse 73
P.O. Box
5430 Wettingen
Switzerland
Tel. +41 56 437 11 11

nagra.ch

nagra.

Arbeitsbericht NAB 23-10

A Radionuclide Release Model for Spent UO_2 and MOX Fuel for Safety Assessment with Application to Waste to be Disposed of in a Deep Geological Repository in Switzerland

February 2023

L.H. Johnson[1], E. Curti[2] & K. Spahiu[3]

[1] Independent consultant, Winnipeg, Manitoba, Canada
[2] Paul Scherrer Institut, Villigen PSI
[3] Kaspa Consult AB, Täby, Sweden

KEYWORDS

Spent fuel, UO_2 fuel, MOX fuel, Instant release fraction, dissolution rate, safety assessment

National Cooperative
for the Disposal of
Radioactive Waste

Hardstrasse 73
P.O. Box
5430 Wettingen
Switzerland
Tel. +41 56 437 11 11

nagra.ch

Nagra Arbeitsberichte ("Working Reports") present the results of work in progress that have not necessarily been subject to a comprehensive review. They are intended to provide rapid dissemination of current information.
This report was prepared on behalf of Nagra. The viewpoints presented and conclusions reached are those of the author(s) and do not necessarily represent those of Nagra.

Table of Contents

List of Tables

List of Figures

List of Acronyms

ADOPT fuel	Cr- and Al-doped UO_2 fuel
am	Amorphous phase
aq	Aqueous phase
BPW	Bentonite pore water
BWR	Boiling water reactor
BU	Burnup
CANDU fuel	Canada Deuterium Uranium fuel
CEC	Cation exchange capacity
cr	Crystalline phase
DDL	Diffuse double layer
DGR	Deep geological repository
ENSI	Eidgenössisches Nuklearsicherheitsinpektorat (Swiss regulator)
EOC	End-of-cycle
EOL	End of life
ε-particles	Noble metal phases in spent fuel
E3-BPW-Ref	Reference Bentonite Porewater for Nagra's licensing step
fcc	Face centred cubic phase
FE	Full scale emplacement experiment
FCR	Fraction of canister reacted
FGR	Fission gas release
FIAP	Fraction of inventory in the aqueous phase
HBU	High burnup fuel
HLW	High-level waste (spent fuel assemblies and vitrified high-level)
HWR	Heavy water reactor
ICP-MS	Inductively coupled Plasma mass spectrometry
ICW	Inside canister water
IRF	Instant release fraction
JO	Jura Ost (considered siting region for DGR)
LWR	Light water reactor
LHR	Linear heat rating
LPR	Linear power rating

MOX	Mixed oxide fuel
NL	Nördlich Lägern (proposed siting region for DGR)
NPP	Nuclear power plant
OPAw	Opalinus Clay porewater
PWR	Pressurised water reactor
s	Solid phase
SF	Spent fuel assemblies
T	Temperature
TH	Thermo-hydraulic model
ZNO	Zürich Nordost (considered siting region for DGR)

1 Introduction

The main objective of the present report is to provide a model for the release of radionuclides from spent fuel for safety assessment calculations that support the general licence application for a repository for HLW in Switzerland, including the definition and justification of parameter values for the model. This goal is achieved based on a detailed literature review, auxiliary calculations and expert judgement. The review includes data from studies published in peer-reviewed articles, as well as in public reports from waste management organizations and EURATOM projects dedicated to spent fuel, up to "FIRST-Nuclides". With few exceptions, the results from the recently finalized DisCo project could not be included in the present review because most of the data produced have not yet been evaluated in a finalised form.

The heterogeneous distribution of radionuclides within spent fuel rods strongly influences the timing and kinetics of their release into pore water after eventual breaching of disposal canisters. This report provides both the basis for assessing the distribution of radionuclides associated with the spent fuel matrix and the model for the kinetics of their release.

The model for release of radionuclides considers the following processes:

a) Release of the so-called IRF (instant release fraction) from the fuel – This applies to a small subset of volatile radionuclides and is defined as

   $IRF = IRF_G + IRF_{GB}$,

   where IRF_G represents the fraction of the total inventory of the radionuclides in the fuel that is released from the gap (the interconnected void space in the fuel rod) and IRF_{GB} is the fraction of the total inventory of the radionuclide in the fuel that is released from grain boundaries. Release from the gap is highly correlated to fission gas release (FGR) since gaseous species accumulate in open spaces at the end of fuel irradiation in the reactor. The term IRF is used in most of the waste management literature because the duration of release is very short (within a few months) relative to the duration of UO_2 matrix dissolution, thus it is represented in safety assessment calculations as an instantaneous term. The assumption that IRF_{GB} is also instantaneously released is pessimistic, as discussed in Section 4.2. The relatively rapid release upon exposure to water of a small fraction of the inventory of some dose-relevant radionuclides, in particular ^{129}I, ^{14}C, ^{36}Cl, ^{135}Cs, has significance in safety assessment of spent fuel disposal because of their long half-lives and potential high mobility in groundwater (Hummel 2017).

b) Fuel matrix dissolution – The largest fraction (> 97%) of the radionuclide inventory (the remaining fission products and activation products as well as the actinides) is released at the same fractional dissolution rate that the fuel matrix dissolves. This process is controlled by the geochemical conditions that exist when the canister is breached as well as the radiation field of the spent fuel.

c) Release of activation products from Zircaloy and other metal parts of the fuel assemblies – This involves rapid release of a fraction of the ^{14}C inventory associated with the Zircaloy oxide film, followed by slow release of activation products as a result of corrosion of the various alloys. The corrosion and radionuclide release model for Zircaloy and other metal parts of the fuel assemblies as derived in other reports is provided in Section 4.7.

The specific radionuclide inventories in the spent fuel matrix, Zircaloy cladding and fuel assembly structural materials are given in MIRAM-RBG Database (Nagra 2023a).

Chapter 2 of the report describes the initial state of the spent fuel at the time of its emplacement in disposal canisters. The various types of fuels are described including information on their composition, burn-up, radiation emissions and structure, as these features influence the release of radionuclides. Detailed information on fission gas release (FGR) for UO_2 and MOX fuels as well as calculated data on FGR and burn-up for Swiss power reactor fuel are also presented. These data are required because FGR is influenced by fuel power history and because radionuclides that are semi-volatile under fuel operating conditions (e.g., ^{129}I and Cs isotopes) exhibit an aqueous release that is proportional to FGR, as discussed in Chapter 4.

Chapter 3 presents information on the composition of the canister and the encapsulated materials (spent fuel, cladding and other structural materials) and their reactivity. This information is specific to the planned Swiss HLW repository and is the basis for the following thermodynamic modelling of the porewater chemistry on both sides of the canister, i.e. bentonite pore water (BPW) and "inside canister water" (ICW) in the context of the reference evolution scenario of the Swiss HLW repository. Predictions of the geochemical conditions are presented, i.e. pH, Eh, as well as concentrations of main solutes, radionuclides and redox-sensitive species (mainly Fe, H_2) that strongly influence the U solubility limit under the strongly reducing conditions expected in the repository. The model calculations are based on the assumption (validated in Chapter 5) that hydrogen evolved by this process is protecting the fuel from radiolytic oxidation at all times after canister failure, which will occur at a time when radiolysis at the spent fuel surface will be weak (10'000 years after waste emplacement or later).

Chapter 4 presents a review of data on short-term aqueous release of various radionuclides. This is followed by a summary of the data that illustrates both the correlation of instant release fraction (IRF) of ^{129}I, ^{36}Cl and Cs isotopes with FGR and the absence of a correlation for some other radionuclides. The term IRF refers to release that is rapid relative to the long timeframe of radiological risk assessment. In practice, this is determined in a duration of a few months under oxic conditions and the IRF contribution is finished when a marked decrease in the cumulative fractional release of nuclides is observed. In recent years there have been many studies published that have provided both a large body of data on the radionuclides that are preferentially released and an understanding of how to estimate the releases from a repository. These data refer to spent fuel having a broad range of burn-up values from light water reactors (LWR), i.e. boiling water reactors (BWR) and pressurized water reactors (PWR). Also discussed are data on rapid release of ^{14}C and ^{36}Cl from fuel as well as the data on rapid release of ^{79}Se, ^{99}Tc and ^{107}Pd. The recommended IRF values for the various fuels are then presented.

Chapter 5 discusses the dissolution of the UO_2 matrix, including a review of studies of spent fuel, alpha-doped UO_2 and relevant aspects of radiation chemistry. Based on this review, the recommended rate of matrix dissolution is derived.

Chapter 6 presents a literature review on geochemical studies of selected analogues of spent UO_2 fuels, namely the Cigar Lake, Oklo and Witwatersrand deposits, focussing on the long-term stability of uraninite and the suppression of radiolytic oxidation by H_2. Data on fission product mobility from the Oklo natural reactor are also briefly discussed. The collected evidence is used complementarily to laboratory data to support the long-term validity of the matrix dissolution rates derived in Chapter 5.

Chapter 7 presents the selected reference values for spent fuel dissolution rates and for the prompt release of nuclides upon first contact with water (Instant Release Fractions, or IRF). These values will be used as input in safety assessment calculations. They are based on currently available experimental and theoretical evidence, thoroughly discussed in Chapter 2 and Chapter 5. A short summary of supporting arguments is also included (Section 7.2).

2 Initial state of the spent fuel in the disposal canisters at the time of emplacement in the repository

2.1 Types of spent fuel requiring disposal

There are four reactors currently (2023) operating in Switzerland in the three nuclear power plants at Beznau (2), Gösgen (1) and Leibstadt (1). The fifth reactor (Mühleberg) ceased operation on Dec. 20th, 2021. Besides the mentioned commercial reactors, a small amount of spent UO_2 fuel arises from the decommissioned Diorit II research reactor, operated between 1972 and 1977 by EIR (now integrated in the Paul Scherrer Institute). Tab. 2-1 presents a summary of the origin, the number of assemblies and burnups of the spent fuel to be disposed of. Further data on the chemical composition of structural materials and fuels, as well as the corresponding radionuclide inventories, can be found in the MIRAM-RBG database Nagra (2023a). The average and maximum burnup values are based on historical data and projections to the end of life of the reactors. Besides enriched UO_2 fuel, which is by far the dominant spent fuel type, a small number of MOX fuel assemblies have been used in the Beznau and Gösgen reactors. In addition, some UO_2 fuel assemblies at Beznau and Leibstadt contain UO_2 pellets doped with a small amount of Cr_2O_3 additive.

The data on fuel type and burnup have been used in conjunction with FGR calculations discussed below to estimate average FGR of the fuel from the various Swiss reactors.

Tab. 2-1: Numbers of fuel assemblies projected to accumulate by the end of life of the Swiss reactors, fuel assembly types (Nagra 2023a), and their average and maximum burnup (BU) values

Reactor (type)*	**Avg/Max BU** [MWd/kg_{iHM}]	**Fuel type**	**Assemblies** [number]
Beznau 1+2 (PWR)	44 / 57	MOX	232
Beznau 1+2 (PWR)	47 / 60	UO_2	1'569
Gösgen (PWR)	44 / 57	MOX	148
Gösgen (PWR)	55 / 74	UO_2	1'612
Leibstadt (BWR)	46 / 63	UO_2	7'710
Mühleberg (BWR)	47 / 62	UO_2	1'177
Diorit II (HWR)	no data	UO_2	349
Totals			12'797

* PWR = Pressurized Water Reactor, BWR = Boiling Water Reactor, HWR = Heavy Water Reactor

2.2 Chemical state and microstructure of spent fuel

2.2.1 Overview of Fuel rod structure and radionuclide distribution

During irradiation, the temperatures in the UO_2 range from 1'000 – 1'500 °C in the pellet centre to about 400 °C at the pellet rim. Fig. 2-1 shows the conceptual distribution of safety-relevant radionuclides in a spent fuel rod after irradiation. During in-reactor irradiation, a fraction of the inventory of some radionuclides produced in the UO_2 fuel matrix is segregated to grain boundaries, to cracks in the fuel and to the gap between the fuel and cladding. Similarly, a fraction of the fission gas produced also segregates. The majority (> 97%) of the radionuclide inventory resides in the UO_2 matrix and in the cladding, in which activation products are formed. The internal side of the cladding has an oxide film that can contain some radionuclides that may have been trapped during the formation of the oxide.

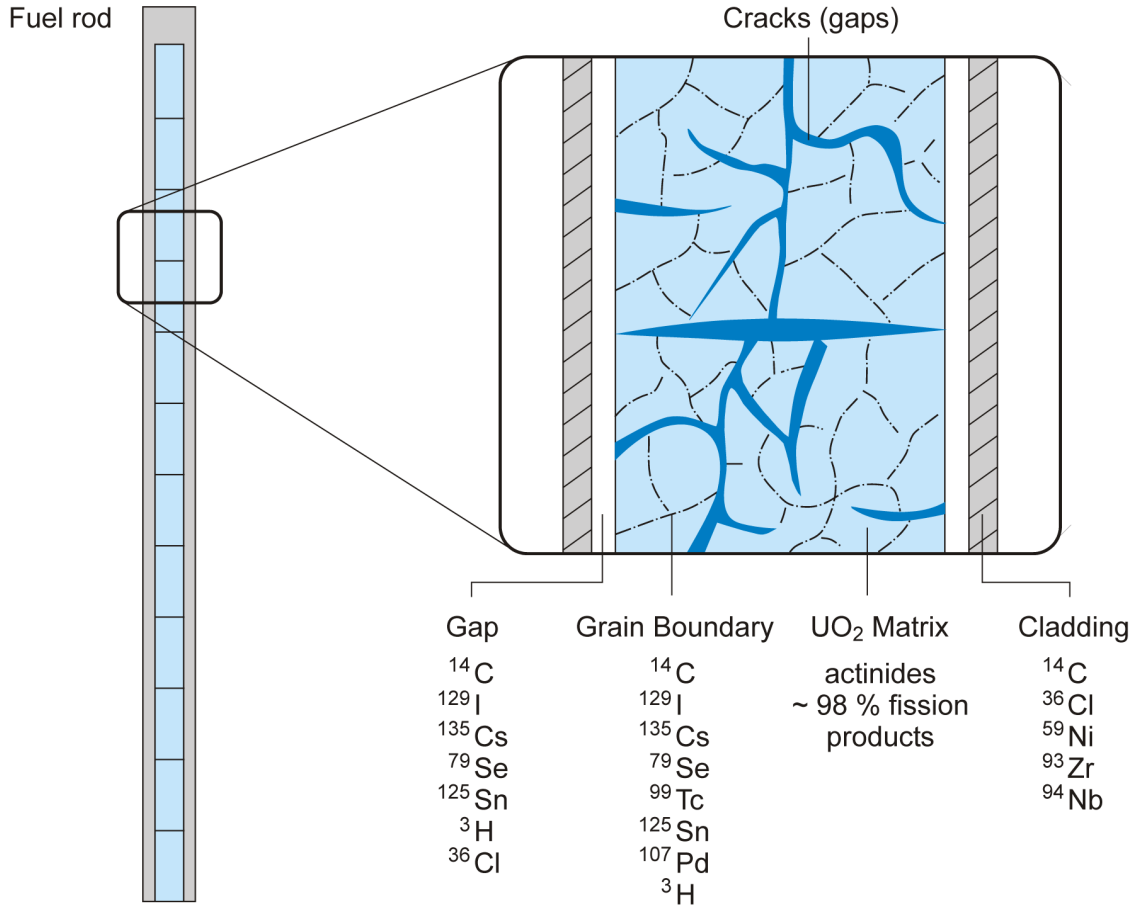

Fig. 2-1: Conceptual distribution of radionuclides in a spent fuel rod

From Johnson (1994) redrawn after Johnson and Tait (1997)

2.2.2 Chemical state of the fuel

2.2.2.1 Definition and significance of oxygen potential

The most important chemical parameter of oxide fuels under "in-pile" conditions, i.e. during operation in a nuclear power reactor, is the partial pressure of oxygen (pO_2 [bar]) and the derived property oxygen potential, which is defined as (Besmann 2012):

$$\Delta\bar{G}_{O_2} \cong R\,T\ln\left(p_{O_2}/p^o\right) \tag{2.1}$$

where R [J mol^{-1}] is the universal gas constant, T [K] is absolute temperature and p^o= 1 bar is the standard state total pressure. The use of pressures instead of fugacities in eq. (2.1) is a common, reasonably good approximation since fugacity coefficients are very close to unity at the comparatively low pressures inside the operating assemblies.

The oxygen potential is a key parameter reflecting the oxidation state of the fuel (Olander 1976). It has an impact on safety-relevant properties during reactor operation such as the rate of cladding oxidation (and thus its service lifetime). Exceedingly high oxygen potentials may lead to fuel hyperstoichiometry, making the fuel matrix more soluble and hence more readily dissolved under disposal conditions, or even lead to oxidation of redox-sensitive fission products / actinides (e.g. to yield Mo^{VII}, $Se^{IV,VI}$, Np^{V}, $Pu^{V,VI}$), increasing their solubility limits.

The oxidation state of (U,Pu)O_2 fuels can be quantified by either the oxygen/metal ratio (O/M) or by the hyperstoichiometry coefficient x in the generalized formula (U, Pu)$O_{2\pm x}$. Both quantities can be related to the oxygen potential, either by directly measuring pO_2 or by calculating it via thermodynamic models.

Experimental measurements of oxygen potentials as a function of (U,Pu)$O_{2\pm x}$ stoichiometry by gravimetric or electrochemical methods (Olander 1976) have been carried out mostly on unirradiated (U,Pu) oxide (e.g. Blackburn 1973, Nakamura & Fujino 1987, Une & Oguma 1983). Data on real spent fuel are unfortunately scarce (Une et al. 1991, Matzke 1995, Walker et al. 2005) due to technical problems related to the high radiological dose rates involved. Therefore, these measurements are complemented by calculations based on advanced thermodynamic models.

To be meaningful, such models must be able to take into account the complex solid solution chemistry of (U,Pu)O_{2+x} and of minor phases, such as noble metal (ε-particles) and oxide inclusions known as "grey phases" (see Section 2.2.2.3). This in turn requires a detailed knowledge of the thermodynamic mixing properties of the ions and elements partitioning into the aforementioned solids (see Section 2.2.2.2). Recently, advanced models have been developed that allow calculating the oxygen potential of irradiated spent fuels (Kaye et al. 2007, Ozrin 2011, Thompson et al. 2012, Curti & Kulik 2020). The model of Curti & Kulik (2020) is presented in Section 2.2.2.3, along with its application to conventional and Cr-doped LWR spent fuel. This is followed by the evaluation of the results in terms of consequences on spent fuel dissolution and radionuclide release.

2.2.2.2 Chemical partitioning and classification of radionuclides in $(U,Pu)O_2$ spent fuel

The large number of radioelements present in spent fuel are categorized in Tab. 2-2, based on their volatility under reactor operating conditions and their solid-state chemistry.

These categories are well established and have a sound theoretical basis (e.g. Kleykamp 1985) as well as confirmatory evidence gained through microanalysis of spent fuel (e.g. Thomas et al. 1992 and Walker et al. 1996). A small group of fission products (Tc, Pd, Rh, Ru, Mo) are in metallic form under fuel operating conditions and congregate by thermal diffusion to form noble alloy particles (ε-particles) in which their relative proportions are similar to their fission yields (Jeffery 1967, Kleycamp 1985, Cui et al. 2010). These particles are resistant to dissolution in water under reducing conditions (Ekeroth et al. 2020).

In the case of CANDU fuel (natural UO_2 fuel), which is irradiated to low burn-up with a higher linear power rating (250–550 W/cm) than LWR fuel, X-ray photoelectron spectroscopy data show that Cs, Rb, Te and Ba are associated with fission gas bubbles in the grain boundaries, often with high surface enrichments (Hocking et al. 1994). In high-FGR LWR fuel (e.g. Gösgen), Cs exists as a vapour in the centre of the fuel and is transported through fission gas micro-tunnels, leading to condensation in gas bubbles in the mid-radial region (Walker et al. 1996). Thomas et al. (1992) found high surface concentrations in grain boundaries of Cs and Te as well as Pd and ε-phases for a high FGR fuel (18%). For a fuel irradiated at lower linear power rating (LPR) with moderate burnup and low fission gas release, an Auger spectroscopy study showed no detectable amounts of Cs, Sr and Tc at grain boundaries, although nm-scale ε-phase particles were observed within the UO_2 grains (Thomas et al. 1992). The latter findings are likely to be more representative of most Swiss power reactor fuel for which FGR is generally low (see Section 2.3.2).

The rare earth fission products and the actinides are known to be quantitatively in solid solution with the UO_2 matrix of the fuel. They are not segregated and consequently not preferentially released in water. Sr and Zr are both in solid solution UO_2 and in the so-called "grey phase" oxides. The release rate of Sr is frequently used as an indicator of the fuel matrix dissolution rate (Johnson and Shoesmith 1988), although it can exhibit limited preferential release (Ekeroth et al. 2020, Roth et al. 2019). Despite this, the Sr release in fuel dissolution experiments appears to be the best indicator of the matrix dissolution rate.

There are two important light long-lived activation products present in spent fuel. These are ^{36}Cl, arising from ^{35}Cl, a trace contaminant in UO_2, and ^{14}C, arising from trace ^{14}N in UO_2. Only ^{36}Cl falls in the semivolatile category along with Cs, Rb and I. In contrast, ^{14}C shows some preferential release as discussed in Section 4.4, but is non-volatile and its release is not correlated with FGR.

Tab. 2-2: Chemical categorisation of radionuclides in spent fuel, with qualitative comments on the IRF

Quantitative estimates of the IRF are discussed in Sections 3.

Category	Radioelements	Comments	IRF
Volatile and semi-volatile	Fission gases (Kr, Xe), I, Cs, Rb, Cl	Fission gases and I in bubbles; Cs and Rb, condensed as soluble salts, but may also exist as oxides	Function of linear power rating and to a lesser degree burn-up
Oxide formers in solid solution at cationic sites in UO_2	Lanthanides, actinides, Sr	Concentrations in solution controlled by low dissolution rate of UO_2 and by the element solubility	None
Metallic	Tc, Rh, Ru, Pd, Mo	Mostly in alloy inclusions (ε-phases) that are resistant to dissolution	Very low
Oxide formers partially segregated	Sr, Ba, Zr	Sr may be present partly in zirconate inclusions	Low
Other	Se	Se is possibly present as selenide substituent for oxygen or at vacancies in UO_2	Low

2.2.2.3 Oxygen potential of conventional and Cr-doped UO_2 fuel as a function of temperature and burnup

In this Section, we present and discuss the results of oxygen potential calculations based on the model of Curti & Kulik (2020) for conventional and Cr_2O_3-doped UO_2 fuel. The model treats the UO_2 phase as a multicomponent solid solution using the sublattice formalism of Berman & Brown (1984). Three distinct sites (cationic, anionic, interstitial) were specified to describe substitutions of U^{4+} by U^{5+}, Pu^{4+}, Pu^{6+}, Am^{3+}, Cm^{3+}, Np^{4+}, Np^{5+}, La^{3+}, Nd^{3+}, Ce^{3+}, Ce^{4+}, Cr^{3+}, or O^{2-} anions by vacancies and of vacant interstitial sites by O^{2-}, respectively. The model also includes a non-ideal noble-metal (ε-particles) solid solution with Mo, Pd, Ru, Rh, Tc end-members, a binary $(Sr,Ba)ZrO_3$ ideal solid solution to represent the "grey phase", stoichiometric solids representing elements in excess or incompatible with the solid solutions (Cr, Cr_2O_3,$CeCrO_3$, $BaMoO_4$, Cs_2MoO_4, RbI, Rb_2O, $RuSe_2$, $RuTe_2$, ZrO_2) and the ideal gas phase. It was implemented into GEM-Selektor package (Kulik et al. 2013) using thermodynamic state-of-the-art data and mixing parameters as derived in Curti & Kulik (2020).

Fig. 2-2 shows the calculated oxygen potentials for conventional and Cr_2O_3-doped UO_2 fuel as a function of temperature for three different burnups (1, 23, 60 MWd/kg_{iHM}). In the initial stages of irradiation they are low and progressively increase with burnup. Except at 1 MWd/kg_{iHM} and T > 1'180 °C, the oxygen potentials of Cr-doped and non-doped fuel are nearly identical at all temperatures and burnups. Thus, Cr-doping appears to have no significant effect on the oxidation state of the fuel. The oxygen potential curves increase systematically up to about 40 MWd/kg_{iHM}

(not shown). No further increase is calculated at higher burnup, i.e. the T-dependent curves coincide at BU > MWd/kg_{iHM} pointing to a buffering mechanism which is readily explained by coexistence at equilibrium of metallic Mo (in the noble metal solid solution) and pure Mo(IV)O_2 phase:

$$\text{Mo(ss)} + O_2\text{(g)} = MoO_2\text{(cr)},\ K = \frac{1}{p_{O_2}\, a_{Mo}^{SS}} = \frac{1}{p_{O_2}\, \gamma_{Mo}^{SS}\, x_{Mo}^{SS}} \qquad (2.2)$$

K is the equilibrium constant, a_{Mo}^{SS} , γ_{Mo}^{SS} , x_{Mo}^{SS} are activity, activity coefficient and mole fraction of metallic Mo in the noble metal solid solution, respectively. The equilibrium relationship (2.2) shows that pO_2 (and therefore the oxygen potential) is a function of Mo concentration in the ε-particles. As the Mo concentration in the ε-particles decreases (dilution), pO_2 must increase. This dilution effect explains the calculated oxygen potential "excess" of 5 – 20 kJ/mol compared to MoO_2(cr) in equilibrium with pure metallic Mo, in which case the activity of Mo is unity. The effect is however too small to oxidize any redox-sensitive radionuclide. Previous calculations carried out for high-burnup conventional UO_2 fuels as a function of pellet radius (Ozrin 2011) yielded slightly lower oxygen potentials assuming ideal solid solution formation in the UO_2 phase.

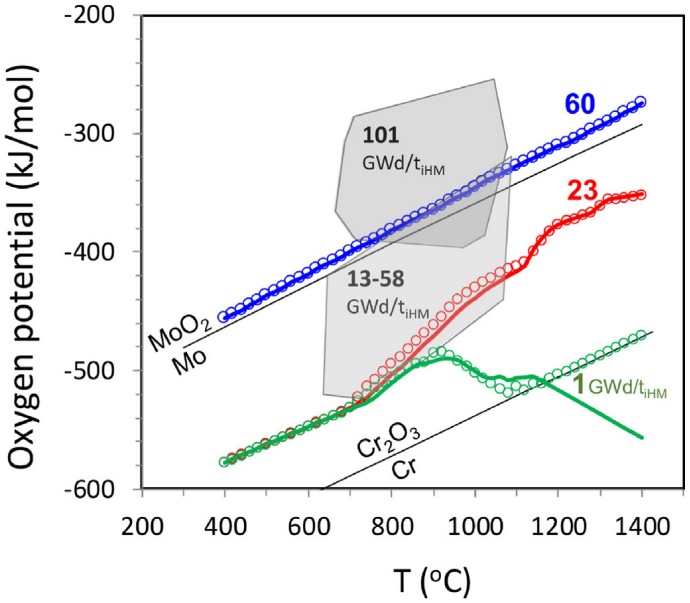

Fig. 2-2: Calculated oxygen potential curves for conventional and Cr-doped UO_2 fuels at three different burnups (1, 23, 60 MW/kg_{iHM})

The grey fields delimit values of published experimental data (Une et al. 1991, Matzke 1995, Walker et al. 2005). Colored lines indicate oxygen potentials of non-doped UO_2 fuel, while circles show corresponding calculations for Cr-doped fuel. The orange squares and bars show the results of published calculations (Ozrin 1995) for high-burnup non-doped UO_2 fuel. The oxygen potentials of Mo-MoO_2 and Cr-Cr_2O_3 pure metal/oxide pairs are shown for comparison. From Curti & Kulik (2020), reprinted with permission from the publisher

Fig. 2-2 also includes $\Delta\bar{G}_{O_2} - T$ regions encompassing experimental oxygen potential measurements on irradiated LWR UO_2 fuels. The comparison of the measurements with the model calculations shows that the computational results for 23 and 60 GWd/t_{iHM} agree well with the measurements of fuels with burnups between 13 and 58 GWd/t_{iHM} (Matzke 1995, Une et al. 1991).

Somewhat surprisingly, it turns out that replacing pure UO_2 with a complex non-ideal UO_2 solid solution has only a minor effect on the calculated oxygen potentials (see curves labeled "ps", and "3 ss", Fig. 2-3). The combined effect of UO_2 and epsilon-particles solid solutions is to increase the oxygen potential by 10-30 kJ/mol. This effect is small compared to the wide range of oxygen potential values determined experimentally on irradiated LWR fuels. It has no consequence on the oxidation state of dose-relevant nuclides.

As already mentioned, the calculations of Curti & Kulik (2020) also indicate that doping with Cr_2O_3 will have practically no impact on the oxygen potential of LWR fuels, except at very low burnup and highest in-pile temperatures, when Cr_2O_3 coexists at equilibrium with metallic Cr (green curves in Fig. 2-2). Then the oxygen potential curve of Cr-doped UO_2 follows the Cr_2O_3/Cr buffer line and largely departs from that of conventional UO_2. At all other temperatures and /or burnups the model predicts that only Cr(III) is stable and that its effect on the oxygen potential is negligible.

In contrast, taking into account the consumption of oxygen by Zircaloy oxidation (curve labeled "3 ss + zox", Fig. 2-3) shows a pronounced beneficial effect, as the calculated (average) oxygen potentials decrease by up to 60 kJ/mol. In a real fuel, the effect is expected to be localized at the pellet periphery.

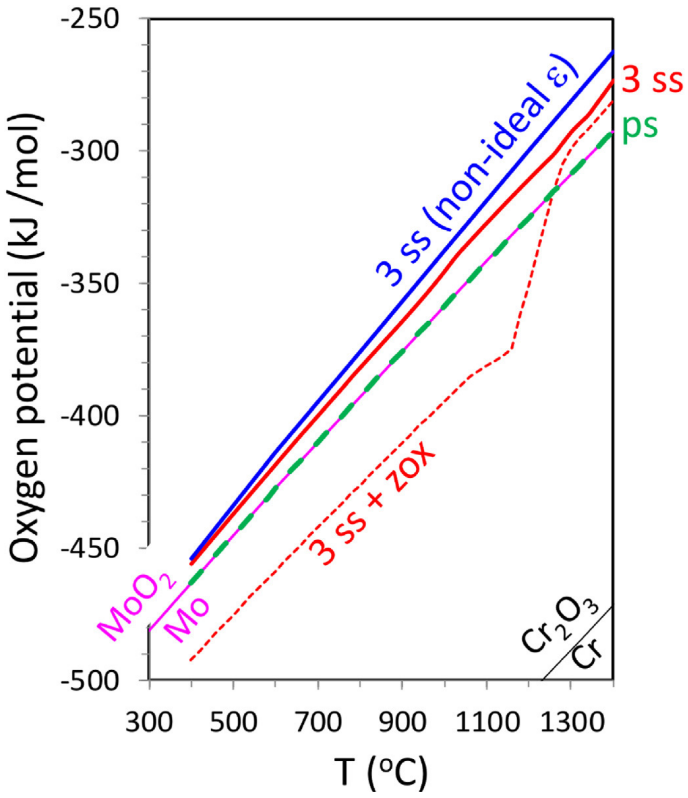

Fig. 2-3: Ellingham diagram showing oxygen potential calculations

ps = only stoichiometric solids (no solid solution); *3 ss* = full solid solution model with ideal mixing in ε-particles; *3 ss (non-ideal ε)* = full solid solution model with non-ideal mixing in ε-particles; *3 ss + zox* = 3 ss calculation including average effect of Zircaloy oxidation; *Mo/MoO₂* = pure metallic Mo/MoO_2 buffer; *Cr/CrO₂* = pure metallic Cr/Cr_2O_3 buffer. From Curti & Kulik (2020), reprinted with permission from the publisher

2.2.3 Fuel Microstructure

The macro- and micro-structure of a spent fuel rod are shown in Figs. 2-4 and 2-5.

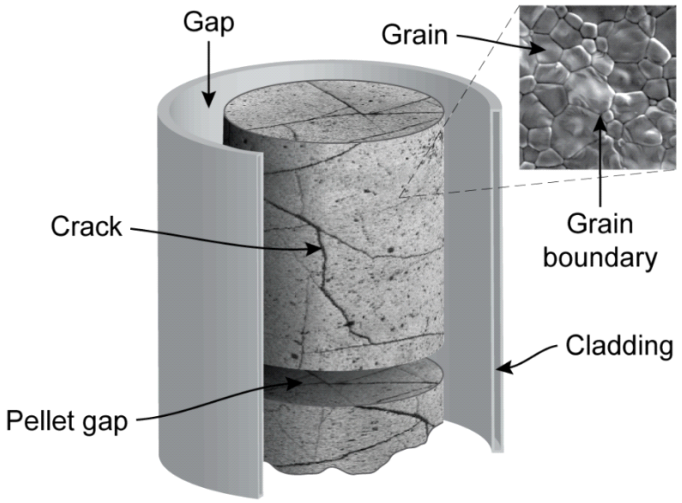

Fig. 2-4: The macro- and microstructure of a fuel pellet after its irradiation

See the cracks and the grain boundaries. The widths of the pellet-cladding and pellet-pellet gaps are purposely exaggerated for the sake of clarity. From Fors (2009), reprinted with the permission from the author

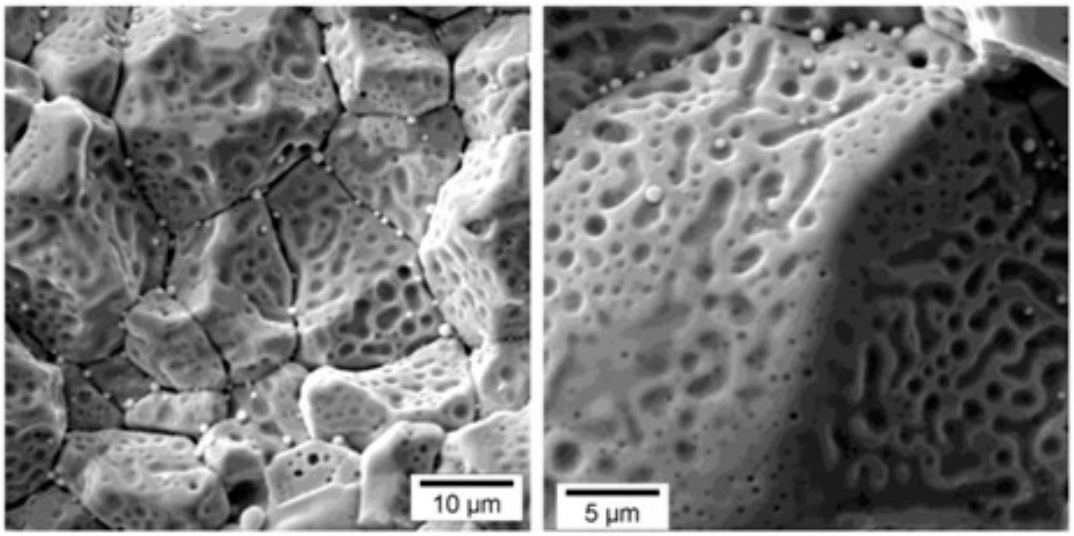

Fig. 2-5: A fracture surface of irradiated UO_2 showing the imprints of grain boundary fission gas bubbles and the beginning of formation of gas tunnels on grain faces, burn-up 38.8 MWd/kg_{iHM}

From Noirot et al. (2009), printed with permission from IAEA

The tiny white spheres are noble metal fission product ε-particles. See Section 2.3.1 for a discussion of FGR.

At elevated burn-up values (above about 45 – 50 MWd/kg_{iHM}), restructuring of grains occurs in the outer region of the fuel pellet (rim) as a result of the higher fission rate, as shown in Figs. 2-6 and 2-7. The restructuring leads to a reduction of grain size to about 0.1 µm and accumulation of fission gas in pores. Microstructural examination of fuel in the high burnup rim shows that, in contrast to fission gas, Cs is completely retained within the grains of the rim (Walker et al. 1996).

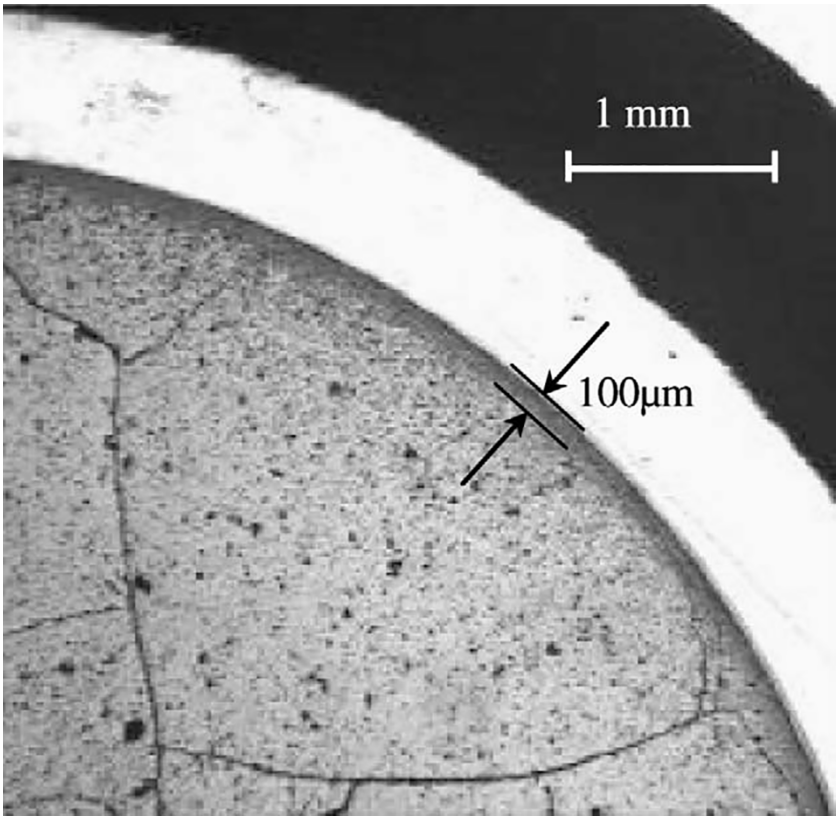

Fig. 2-6: Photograph of spent fuel showing the high burn-up rim region adjacent to the cladding

From Fors et al. (2009), reprinted with permission from the publisher

Accumulation of FG in the rim's pores becomes important above an average rod burnup of about 50 MWd/kg_{iHM} (Johnson et al. 2005) and the trapped FG can represent a significant fraction of the amount released from the matrix. Given the results of Walker et al. (1996) that show complete retention of Cs in the matrix of the rim region, the estimates of large grain boundary inventories in the rim region in Johnson et al. (2005) are clearly not valid for Cs, although the possible release of I into pores has not been studied. The potential for the fission gas and any other fission products associated with the pores to be released rapidly in water is discussed in Section 2.3.

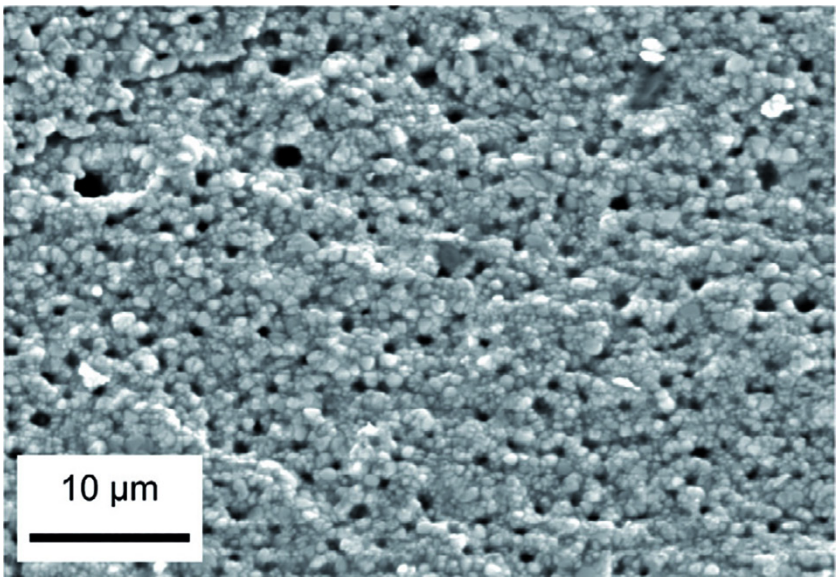

Fig. 2-7: Scanning electron microscopy micrograph of the high burn-up rim region with a local burnup of 75 MWd/kg_{iHM}

From Rondinella & Wiss (2010), reprinted with permission from the publisher

The distribution of fission gas within fuel rods has been determined in studies of the French radioactive waste management program. The results, which are based on a variety of analytical methods including capturing the fission gas released during stepwise air oxidation experiments and leaching studies, are shown in Tab. 2-3 for a fuel irradiated to a burnup of 60 MWd/kg_{iHM} at the typical LPR of French PWRs. It is important to note that these results are representative of fuels irradiated at the relatively low LPR of French PWR fuel. The important role of LPR in FGR and behaviour of other volatile radionuclides and how these data differ in some cases for Swiss reactor fuel are discussed in Section 2.3.

Tab. 2-3: Distribution of the fission gases (Kr, Xe) in a UO_2 fuel rod with a burn-up of 60 MWd/kg_{iHM}

Carbol et al. (2020), adapted from Ferry et al. (2005)

Gas fraction in free volume	0.03
Inter-granular gas fraction	0.019 – 0.042 in central part ($r < 0.5r_0$)
	0.014 – 0.048 intermediate part ($0.05r_0 < r < 0.975r_0$)
	0.045 – 0.062 in the rim pores ($0.975\ r_0 < r$)
Total inter-granular gas fraction	0.08 – 0.15
Fraction in the grains	0.80 – 0.90

2.3 FGR in Swiss power reactor fuel

2.3.1 Overview of FGR

FGR in power reactor fuel is an important parameter in design and performance of nuclear fuel. The central region of the fuel pin reaches temperatures of 1'000 – 1'500 °C under normal reactor operating conditions, causing fission gas to diffuse to grain boundaries where they accumulate in bubbles. Eventually some of these gas bubbles become connected forming tunnels and the gas is released to the interconnected void space (the fuel to sheath gap, fractures in the pellets and the plenum at the end of the fuel pin) (Rest et al. 2019). The operational parameter controlling FGR is the linear power rating (LPR) of the fuel (the power per unit length of the fuel rod), also referred to as the linear heat rating (LHR), which is proportional to fuel temperature. There is a high degree of scatter in the normal operation FGR values, but the evidence for a threshold value of LHR above which FGR increases significantly is clear, as seen in Fig. 2-8.

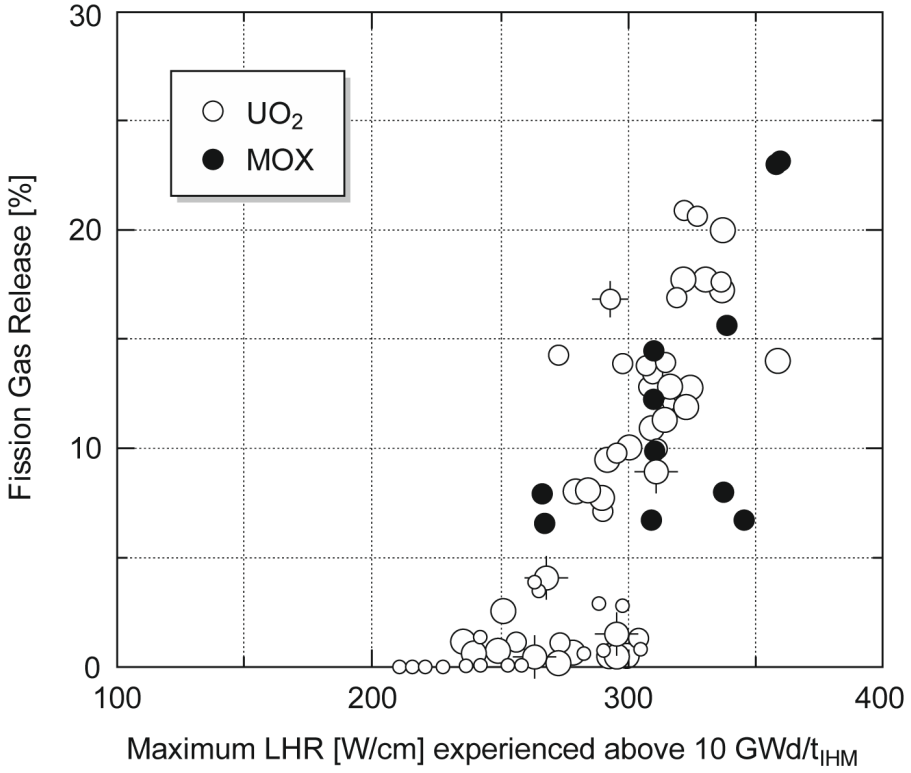

Fig. 2-8: Fission gas release of Boiling Water Reactor MOX and UO_2 fuels as a function of the linear heat rating (in W/cm)

Redrawn after Kamimura (1992), reprinted with permission from IAEA

The LPR of LWR fuel is typically in the range of about 300 W/cm at the beginning of irradiation, declining to around 150 W/cm at the end of irradiation.

FGR is highly relevant to aqueous radionuclide release because it correlates with the segregation of safety-relevant radionuclides ^{129}I, ^{137}Cs and ^{135}Cs and ^{36}Cl, which are volatile under in-reactor irradiation conditions. Therefore, FGR calculations can be used in conjunction with leaching experiments to estimate their release under disposal conditions, as discussed in Section 2.3.2.

2.3.2 Fission gas release calculations for Swiss reactor fuel assemblies

Knowledge of the FGR from spent fuel from the various reactors provides a basis for evaluating the degree of segregation of other elements (Cs isotopes, ^{129}I and ^{36}Cl) that are volatile under reactor operating conditions and thus provides a basis for estimating the IRF.

FGR is frequently measured in post-irradiation fuel characterization studies. Typically, such studies involve puncture of cladding to collect fission gas from selected fuel rods of fuel assemblies that have been chosen because they have operated in the most extreme range of conditions in the reactors, e.g. high burn-up or high LPR (e.g. Ledergerber 2010). It is important to note that results from such studies are consequently not fully representative of the overall spent fuel assembly population. From the perspective of spent fuel disposal, it is more useful to determine the population distribution and average FGR at reactor discharge end-of-life (EOL) and in some cases end-of-cycle (EOC). Such studies have been performed for Beznau (AREVA 2012), Gösgen (AREVA 2010) and Leibstadt (Oldberg 2009) reactors, based on calculations with FGR codes, for all fuel assemblies irradiated in the reactors. The results in these reports are calculated for each individual fuel assembly in the core based on their stepwise power-burnup histories. These reports also contain comparisons between measured and calculated FGR, allowing evaluation of the accuracy of the calculation methods. The FGR codes used have been approved for fuel rod design calculations by SSM and ENSI (Oldberg 2009). The results from these studies are summarized below. Combined with knowledge of the actual burnup of fuel assemblies, this provides a method of estimating the average FGR for fuel assemblies from each reactor.

2.3.3 NPP Beznau

The modelled distribution of FGR for UO_2 fuel assemblies from NPP Beznau is presented in Fig. 2-9. Tab. 2-4 shows that the average FGR is about 1.4 to 1.8% for end of cycles (EOC) 5, 6 and 7 for average burnups ranging from 54 to 62 MWd/kg_{iHM}) indicating that they are relatively constant.

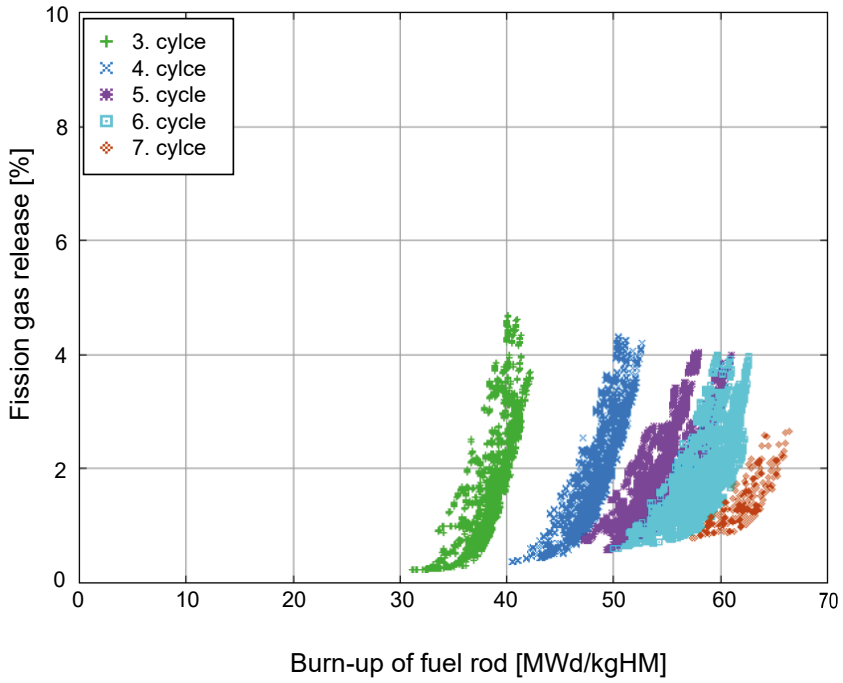

Fig. 2-9: FGR at end of cycle (EOC) for UO_2 fuel assemblies at NNP Beznau

From AREVA (2012)

Tab. 2-4: FGR and burnup of UO_2 fuel assemblies at the end of the respective cycles (NPP Beznau-1/2 6-Region core)

AREVA (2012)

	3rd cycle		4th cycle		5th cycle		6th cycle		7th cycle	
	Burnup [MWd/kg_{iHM}]	**FGR*** [%]	**Burnup** [MWd/kg_{iHM}]	**FGR*** [%]	**Burnup** [MWd/kg_{iHM}]	**FGR*** [%]	**Burnup** [MWd/kg_{iHM}]	**FGR*** [%]	**Burnup** [MWd/kg_{iHM}]	**FGR*** [%]
Avg.	37.7	1.4	47.8	1.7	54.3	1.8	57.6	1.8	62.2	1.5
Max.	42.1	4.7	52.7	4.3	61.0	4.0	62.6	4.0	66.5	2.7

* Average fission gas release

An average FGR of 1.8% is assumed, characteristic of the average burn-up of NPP Beznau UO_2 fuel assemblies of about 50 MWd/kg_{iHM}.

The distribution of modelled FGR for MOX fuel assemblies from NPP Beznau is shown in Fig. 2-10, taken from AREVA (2012). The average FGR is about 3.4% at 49 MWd/kg_{iHM} as shown in Tab. 2-5. However, as shown in Tab. 2-1, the average MOX fuel assembly discharge burn-up is 44 MWd/kg_{iHM} – a lower average value than implied by the curves in Fig 2.9. There is a steep dependence of FGR on burn-up, thus Fig. 2-10 shows that the modelled FGR at the actual average burn-up at Beznau appears to be in the range of 1.5 to 2%. An average value of 2% for MOX fuel assemblies is assumed given the results in Fig. 2-10.

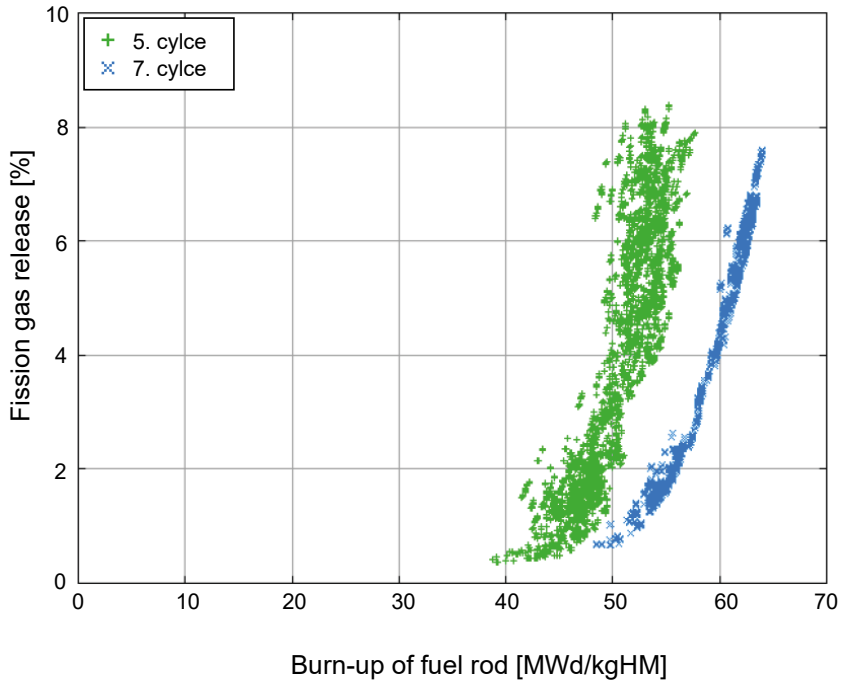

Fig. 2-10: FGR for NPP Beznau MOX fuel assemblies

From AREVA (2012)

Tab. 2-5: FGR and burnup of MOX fuel assemblies at the end of the respective cycles (NPP Beznau-1/2 6-Region core)

AREVA (2012)

	5th cycle		**7th cycle**	
	Burnup [MWd/kg_{iHM}]	**FGR*** [%]	**Burnup** [MWd/kg_{iHM}]	**FGR*** [%]
Avg.	49.4	3.4	57.5	3.4
Max.	57.6	8.4	64.0	7.6

* Average fission gas release

2.3.4 NPP Gösgen

The distribution of FGR for UO_2 fuel assemblies from NPP Gösgen is shown in Fig. 2-11 (AREVA 2010). Average EOC FGR values are relatively constant with burnup. For an average end of life (EOL) burnup of 55 MWd/kg_{iHM}, the average FGR is 13 to 14%, as seen in Tab. 2-6. This is significantly higher than for many other pressurized water reactors (PWRs) and BWRs (Nordström 2009, Johnson et al. 2005). This is caused by higher LPRs (e.g. compare power histories in AREVA 2010 to those in Oldberg 2009). For the purposes of the present report, the average FGR value from the 4th cycle of 14% is adopted for all Gösgen UO_2 fuel assemblies.

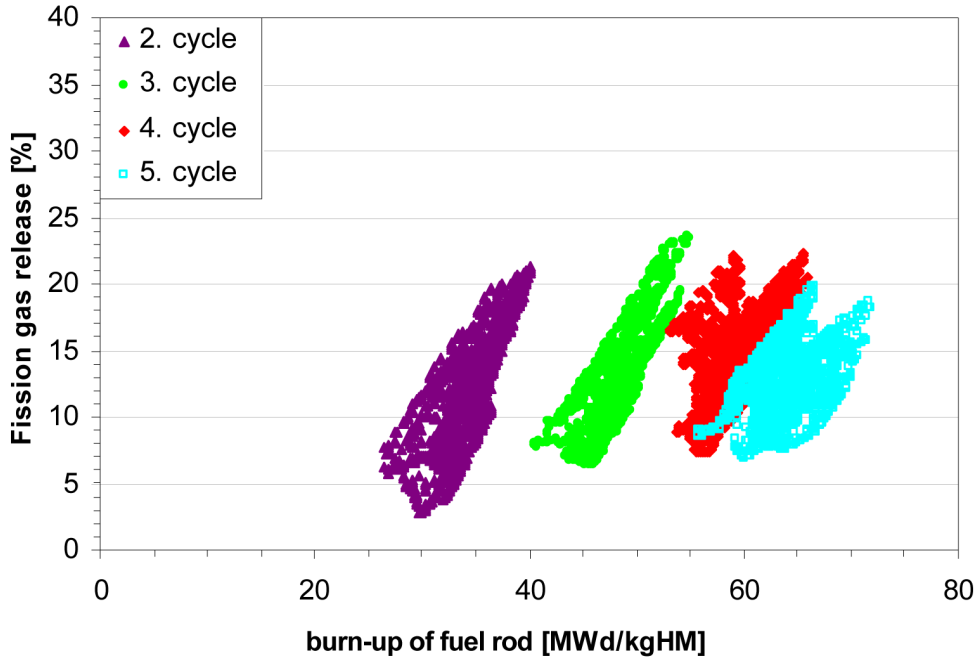

Fig. 2-11: EOC FGR of UO_2 fuel assemblies for NPP Gösgen 5 region core
From AREVA (2010)

Tab. 2-6: Average FGR and burnup at the end of the respective cycles for a NPP Gösgen 5-region-core
AREVA (2010)

	2nd cycle		3rd cycle		4th Cycle		5th cycle	
	Burnup [MWd/kg_{iHM}]	**FGR** [%]	**Burnup** [MWd/kg_{iHM}]	**FGR** [%]	**Burnup** [MWd/kg_{iHM}]	**FGR** [%]	**Burnup** [MWd/kg_{iHM}]	**FGR** [%]
Avg.	34.7	12.3	48.7	13.0	59.4	14.0	63.5	12.8
Max.	40.2	21.2	54.9	23.6	66.0	22.2	71.8	19.9

The distribution of FGR for MOX fuel assemblies from Gösgen is given in AREVA (2010) and the results are shown in Fig. 2-12 and Tab. 2-7. For an average EOL burnup of 55 MWd/kg_{iHM}, the average FGR is about 16%.

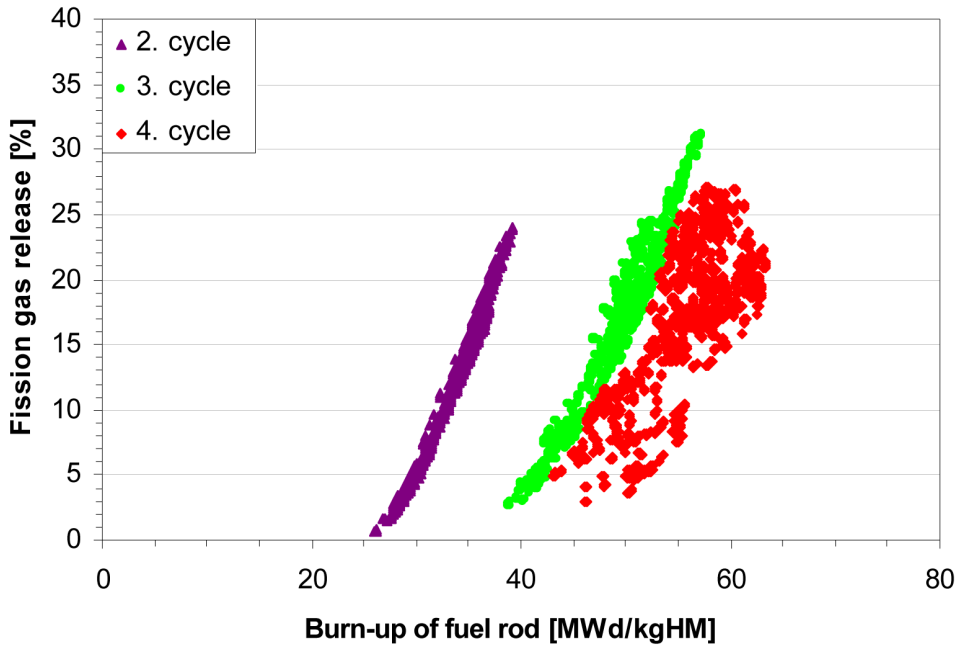

Fig. 2-12: FGR of MOX fuel assemblies for NPP Gösgen Cycle 31 final loading plan

From AREVA (2010)

Tab. 2-7: FGR and burnup of MOX fuel assemblies at the end of the respective cycles for NPP Gösgen Cycle 31 final loading plan

AREVA (2010)

	2nd cycle		3rd cycle		4th Cycle	
	Burnup [MWd/kg$_{iHM}$]	**FGR** [%]	**Burnup** [MWd/kg$_{iHM}$]	**FGR** [%]	**Burnup** [MWd/kg$_{iHM}$]	**FGR** [%]
Avg.	33.6	12.1	48.7	15.6	54.9	15.9
Max.	39.2	24.0	57.3	31.2	63.4	27.1

2.3.5 NPP Leibstadt

The average burn-up of fuel from NPP Leibstadt based on the present inventory in storage and projections is about 46 MWd/kg$_{iHM}$. The modelled distribution of FGR for fuel assemblies from Leibstadt is given in Fig. 2-13 (Oldberg 2009), for which the average FGR is about 4% based on the average FGR at the end of each cycle for NPP Leibstadt given in Tab. 2-8. The previous FGR estimate of 4.5% given in Johnson (2013) assumed a higher average EOL burn-up. That the results in Fig. 2-13 represent bounding values is indicated by the study of Ledergerber et al. (2010) of lead (pilot) assemblies from NPP Leibstadt irradiated to a rod average burn-up of 78 MWd/kg$_{iHM}$, which resulted in all rods having measured FGR below 4.5%. It is thus concluded that an average FGR of 4% represents a best estimate average for Leibstadt fuel assemblies.

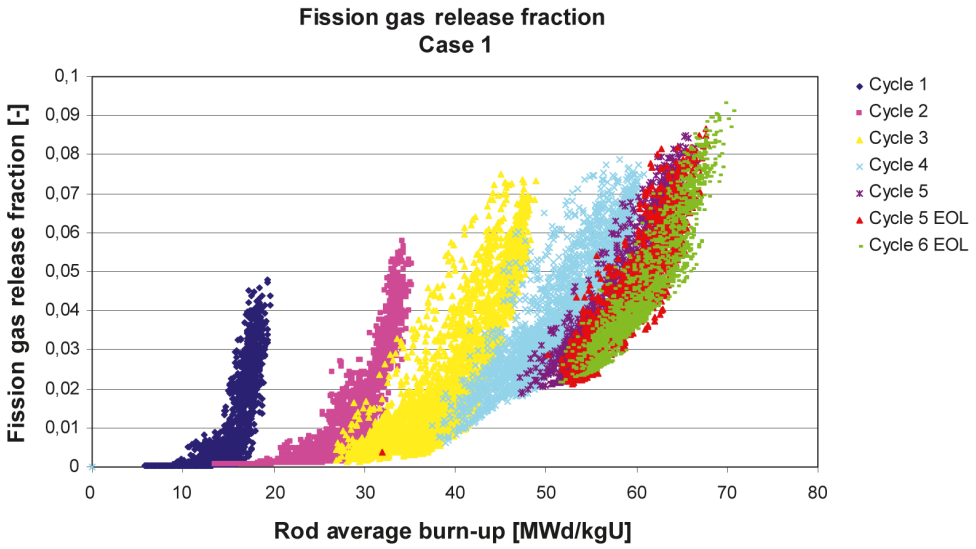

Fig. 2-13: The FGR at EOC and for EOL cycles 5 and 6 for NPP Leibstadt

From Oldberg (2009), courtesy to SKB for permission to reprint figure

Tab. 2-8: Modelled average fission gas release at the end of each cycle for NPP Leibstadt

Adapted from Oldberg (2009)

	Average burnup [MWd/kg_{iHM}]	**Av. FGR%**	**Standard. Dev. FGR in%**
Cycle 1	13.4	0.588	0.986
Cycle 2	26.2	0.945	1.28
Cycle 3	39.0	2.25	1.70
Cycle 4	51.0	3.76	1.50
Cycle 5	58.0	4.33	1.50
Cycle 6	60.6	4.63	1.61
Cycle 5+6 (discharge rods)	59.8	4.53	1.63

2.3.6 NPP Mühleberg

The average burn-up of Mühleberg fuel assemblies is about 47 MWd/kg_{iHM}. The complete distribution of FGR for fuel assemblies from Mühleberg has not been modelled. Compared to the similar Leibstadt fuel assemblies, the Mühleberg fuel assemblies operate at approximately 12% lower average linear power ratings (Appendix A). Given the strong dependence of FGR on LPR, the adoption of the average FGR of Leibstadt fuel of 4% would be expected to be an overestimate for Mühleberg fuel. This can be confirmed by comparing the LPR values of fuel assemblies at Mühleberg to the LPR values for Cases 2 and 4 in Oldberg (2009), which are for fuel assemblies from the Oskarshamn 3 reactor. This comparison, shown in Appendix A, demonstrates that the LPR values for fuel assemblies are the same for Mühleberg and Oskarshamn 2 and 4 cases. From the results it can be concluded that the average FGR of Mühleberg fuel assemblies would be 2.5 to 3.5%: thus a value of 3% is assumed.

2.3.7 Assessment of uncertainties in FGR estimates

It is known that there is frequently a factor of 2 difference between measured and calculated FGR at FGR below 2% but there is typically better agreement at higher FGR. This is illustrated in Fig. 2-14, which shows measured vs. calculated FGR for BWR and PWR UO_2 fuel and PWR MOX fuel (AREVA 2010). The data points are equally distributed on both sides of the 1:1 line. Therefore, it is reasonable to assume that the predictions based on code calculations, which refer to all the rods loaded into the core, are quite accurate.

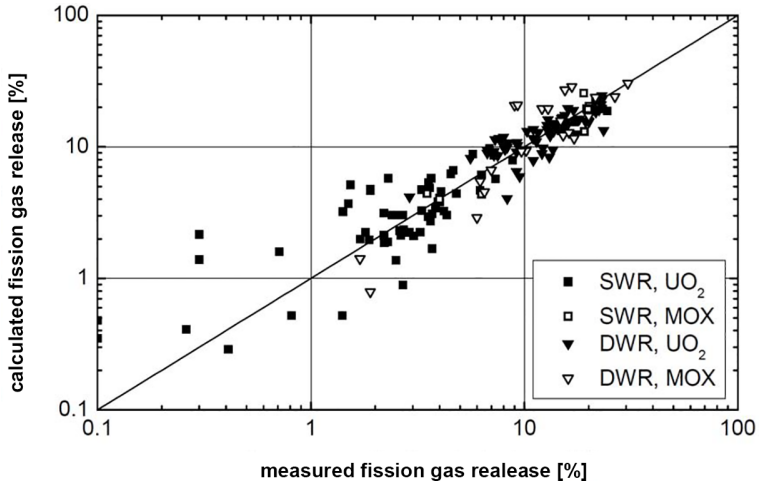

Fig. 2-14: Measured vs. calculated (CARO-E3) FGR for BWR and PWR UO_2 fuel and PWR MOX fuel

From AREVA (2010)

2.4 ^{14}C and ^{36}Cl concentrations in spent fuel

In reactor materials, ^{14}C is an activation product produced largely by the ^{14}N (n,p)^{14}C reaction. Nitrogen is present as an impurity in fuel pellets, arising from adsorption of N_2 onto UO_2 powder prior to compaction into pellets and sometimes as a result of residual N in UO_2 that is produced by reduction of ammonium diuranate. The present ASTM specification for N in UO_2 suggests 75 ppm as a maximum concentration (ASTM 2006). Measurements of N in UO_2 and estimates of ^{14}C production are reported mostly in technical reports that are not published in peer reviewed publications. A review by Bush et al. (1984) refers to seven studies that estimated ^{14}C production in fuel and coolant of reactors. Of these studies, several refer to measurements of N in fuel. A study by Davis (1979) gave results from analysis of fuel from five manufacturers and recommended a value based on these of 25 ppm. Bonka et al. (1974) determined levels in German fuel pellets and found about 5 ppm N with some values higher and assumed a N value of 10 ppm. Other studies are quoted in Bush et al. (1984) but it is not clear how many actual measurements of N in UO_2 were made in the referenced reports (the reports do not give the detailed analytical results or the numbers of samples tested or there is no data reported).

A review by Neeb (1997) stated that N impurity concentrations in BWR and PWR fuels are usually markedly below 10 ppm and are frequently below the analytical detection limit of 4 ppm and that only a few results indicate higher N content in the range of 20 to 30 ppm. A useful result relating to N levels in UO_2 is shown in Fig. 2-15 (Bleier et al. 1987), reported in Neeb (1997).

This shows measured ^{14}C levels in PWR and BWR fuel samples as a function of burn-up, with the shaded areas representing the expected concentration ranges for the fuels based on neutron activation calculations if they had initially contained 5 – 10 ppm N. These ^{14}C levels show that N levels were mostly in the range of 5 – 10 ppm, but that there were a few outliers that would imply levels of perhaps 25 – 30 ppm, especially at higher burn-up.

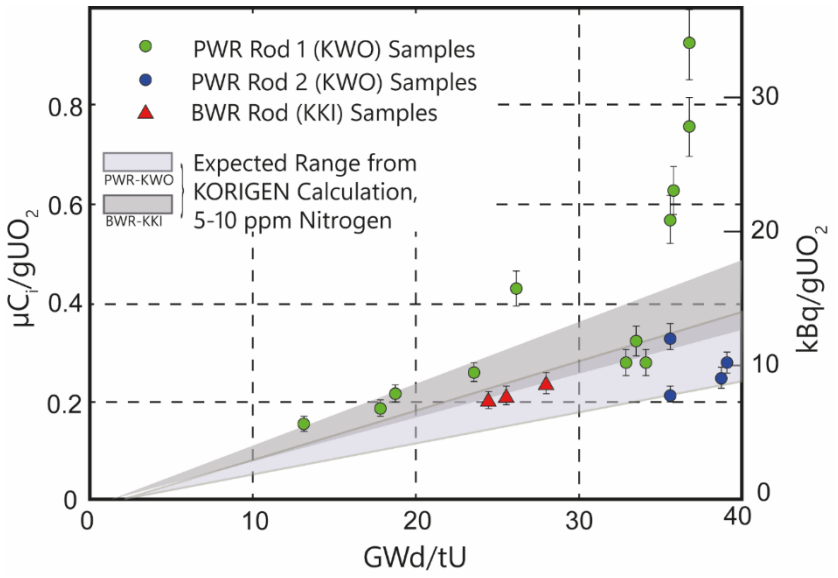

Fig. 2-15: ^{14}C activity in BWR and PWR fuels as a function of burn-up

Redrawn based on Neeb (1997), original figure in Bleier et al. (1987)

Some studies that reported analytical data on N content of fuel pellets are summarized in Tab. 2-9.

Tab. 2-9: N values reported based on analysis of UO_2 fuel pellets

N value	**Comment**	**Reference**
25	Recommended value based on analysis of pellets from several manufacturers	Davis (1979)
10	Based on analysis of German fuel pellets	Bonka et al. (1974)
25	Average value based on analysis of four reference fuels	Guenther (1988a, 1988b, 1991a, 1991b)
~ 10	N value in CANDU UO_2 fuel pellets consistent with measured ^{14}C values in spent fuels	Stroes-Gascoyne et al. (1994)
5 to 10	N values in BWR and PWR fuel pellets consistent with measured ^{14}C levels in spent fuels	Bleier et al. (1987)

The 14 ppm value assumed in SKB SR-Site (SKB 2010a) refers to an EPRI (1995) report that may have taken the value from Bonka et al. (1974).

More recent information, presented by Capouet et al. (2017) within the context of the EU CAST Project, indicates that N levels in UO_2 are in the range of about 35 ppm, but clearly below the 75 ppm ASTM specification (see Fig. 2-16). The data used to prepare the figure come from 10 studies that are listed in Appendix 2 of Capouet (2017) (results from some of these studies are quoted in Tab. 2-9). The reported database covers data obtained over several decades.

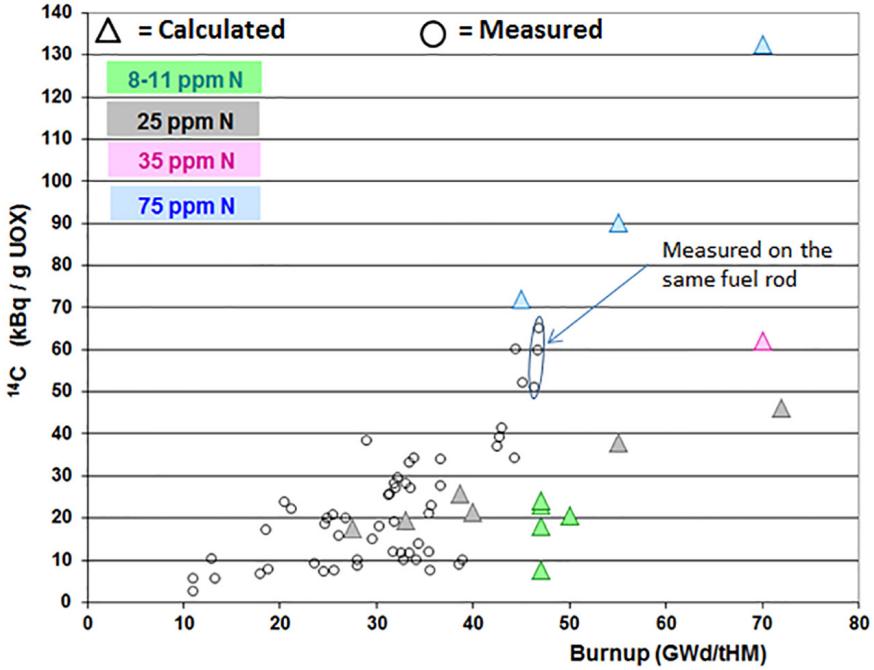

Fig. 2-16: Dependency of ^{14}C level inUO_2 fuel on initial N content

From Capouet et al. (2017)

Overall, the results in Fig. 2-16 correlate with N levels in UO_2 pellets which range from 10 to 50 ppm. It seems reasonable that a mean N value for safety assessment could be set at well below the ASTM specification level of 75 ppm, perhaps in the range 25 – 35 ppm, in the absence of any specific data from suppliers of Swiss power reactor fuel.

Discussion with spent fuel experts suggests that carbon compounds (CO_2, CO and CH_4) are either not detected during rod puncture tests for fission gas or are at very low levels, although a study performed within the FIRST-Nuclides project (Kienzler et al. 2017, Gonzales-Robles et al. 2016) discusses fission gas sampling that detected a very small amount of CO_2 in a rod puncture test. The result is surprising from a thermodynamic point of view, as the oxygen potential in an irradiated sealed fuel rod should be low enough that CO_2 should not form. Radiochemical analysis of fuels shows that by far the majority of ^{14}C is retained within the matrix of the fuel (Neeb 1997). An interesting point worth noting in this report is that the N content of the fuel studied by Kienzler et al. (2017) was given as 11 ppm. Limited new work on release of ^{14}C was performed during the FIRST-Nuclides Project and, of the few measurements performed, none were reported in refereed journals. Reference values of N used by Nagra for stage 3 of the sectoral plan are 25 ppm as a reference value and 75 ppm as an upper bound.

Chlorine is present in UO_2 at trace levels and ^{35}Cl has a large neutron capture cross-section: thus ^{36}Cl is produced during fuel irradiation by neutron capture. The ASTM specification for Cl in UO_2 pellets suggests 25 ppm as maximum concentration (ASTM International C-776-06 (2006): Standard specification for sintered uranium dioxide pellets, September 2006). This is likely much higher than the real concentrations, which have been reported to be 5 – 10 ppm (Guenther et al. 1991a). It is unclear what method was used for analysis of Cl in UO_2 pellets by Guenther et al. (1991a), as this information is not in the referenced report. Nonetheless, the detection limit for Cl in UO_2 is certainly lower than 10 ppm. Tait et al. (1997) used pyrohydrolytic extraction and collection of evolved gases followed by ion chromatography to determine Cl in unirradiated CANDU fuel (natural UO_2 pellets). They reported Cl levels of 2.3 ± 1.1 ppm. Results for enriched UO_2 pellets may differ, but the low levels for CANDU fuel are probably indicative. Prior Nagra safety assessments have adopted a Cl impurity value of 5 ppm. Reference values for Cl used by Nagra for stage 3 of the sectoral plan are 5 ppm as a reference value and 25 ppm as an upper bound.

2.5 Radiation emissions from spent fuel

Spent fuel emits alpha, beta, gamma and neutron radiation. Alpha radiation is the dominant contributor to radiolysis during spent fuel dissolution in the repository (Fig. 2-17), as the fluxes of beta radiation decreases rapidly and becomes low after a few hundred years. Gamma radiation (not shown) follows a similar curve to beta radiation and becomes negligible after a few hundred years. Neutron emissions are insignificant with respect to radiolysis. The influence of radiation on spent fuel dissolution is discussed in Chapter 5.

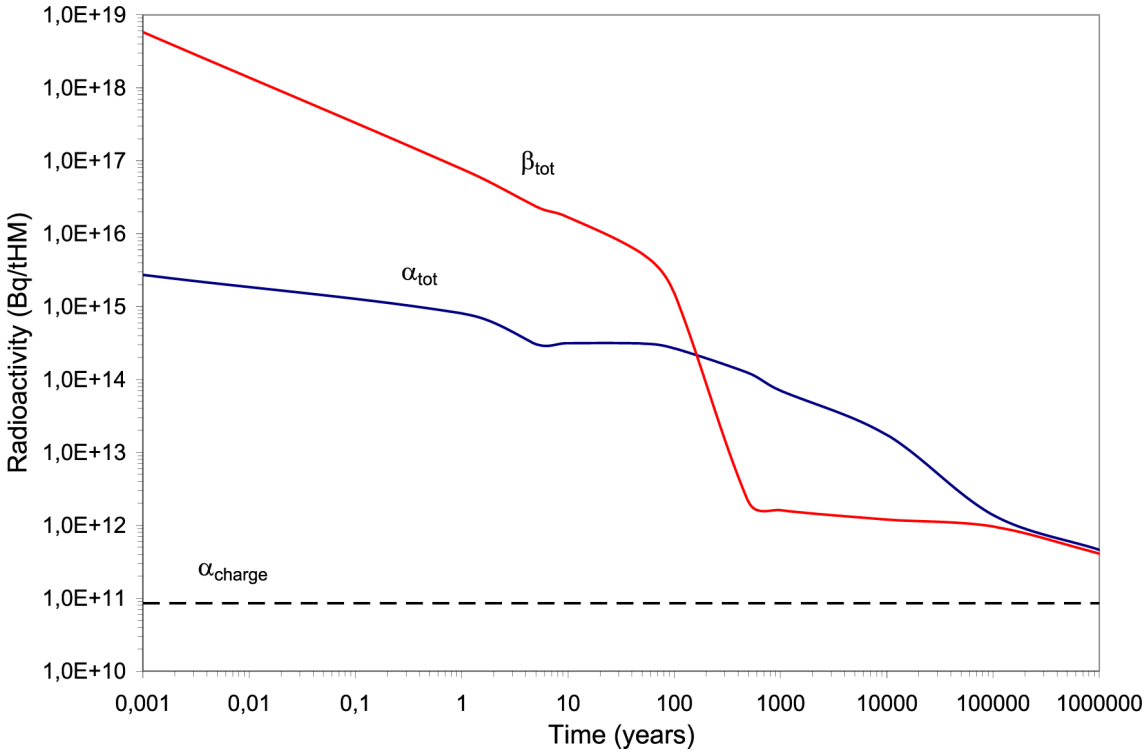

Fig. 2-17: Total number of β and α emissions per t_{iHM} for UO_2 fuel with a BU of 40 GWd/t_{iHM}

The dashed line indicates the α activity of the fuel prior to in-reactor irradiation. From Carbol et al. (2020), reprinted with permission from the publisher

3 Chemical inventories and aqueous chemistry at the inner and outer canister sides

3.1 Composition of waste package materials

3.1.1 Introductory remark

The purpose of this Section is to define the chemical inventories of engineered barrier materials (canister, Zircaloy and other structural materials) in their initial states, i.e., prior to any interaction with aqueous solutions, based on current Nagra specifications. These data, together with the bentonite porewater compositions discussed in Section 3.2, will serve as input for the calculation of bulk chemical conditions inside the canister, presented in Section 3.6.

3.1.2 Composition of Zircaloy and other structural materials

The MIRAM-RBG database (Nagra 2023a) is the basis for the reference radiological and chemical inventories of all waste sorts to be disposed of in Switzerland. For the six different spent fuel waste types from commercial reactors described in Section 2.1, two distinct types of canisters with different internal arrangements have been defined: one hosting BWR SF, the other hosting PWR SF (Nagra 2024). Due to the different reactor types and fuels used in Swiss NPPs, assembly geometries and their chemical compositions are not uniform. This results in some chemical heterogeneity, arising from the different types of Zircaloy cladding and other structural materials used.

Tab. 3-1 shows the overview of the structural material types and their masses for the six spent fuel sorts from commercial reactors (the spent fuel itself is excluded). Besides Zircaloy, several types of corrosion-resistant Ni-Cr-(Mn) steel and smaller amounts of Ni-Cr alloys (Inconel) are used. From the amounts specified in Tab. 3-1 and standardized compositions of the aforementioned materials (not shown), it was possible to build complete chemical inventories of the structural materials for each type of assembly. These are shown in Tab. 3-2, with major elements highlighted in bold. It turns out that the chemistry of *all* structural materials is dominated by Zr, Sn (Zircaloy) and Fe, Cr, Ni (steel and metal alloys) with smaller, significant amounts of Si and Mn. Overall, the differences in chemical composition of the six types of structural materials are small. This justifies selecting a single representative composition (BE-L-UO_2-U-HAA) for the calculations discussed in Section 3.6.

Tab. 3-1: Inventories of Zircaloy and other structural materials (in kg per assembly)

After Nagra 2014, Beilage 1 (Abfallsortenreport)

The selected composition for model presented in Section 3.6 is highlighted in bold.

Spent fuel	Inconel	Inconel	Inconel	Steel	Steel	Steel	Steel	Zircaloy	Zircaloy
Waste sort	718	750	600	US 304	1.4541	1.4571	12.03	2	4
BE-B-MOX-U-HAA	0.736	0	0	0	12.2	1.97	0	0	103
BE-B-UO2-U-HAA	0.736	0	0	0	12.2	1.97	0	0	103
BE-G-MOX-U-HAA	1.97	2.96	0	0	23.0	2.24	0	0	144
BE-G-UO2-U-HAA	1.97	2.96	0	0	22.9	2.26	0	0	144
BE-L-UO2-U-HAA	**0**	**0**	**0.923**	**9.48**	**0**	**0**	**0**	**72.8**	**0.246**
BE-M-UO2-U-HAA	0	0	0.903	0	0	0	10.0	63.9	0

Tab. 3-2: Representative elemental composition (in moles) of structural materials for SF assemblies from Swiss NPPs, calculated from the data in Tab. 3-1 and from the chemical composition of the materials

Major elements are shown in bold.

Waste sort => Element	**BE-B-MOX-U-HAA**	**BE-B-UO2-U-HAA**	**BE-G-MOX-U-HAA**	**BE-G-UO2-U-HAA**	**BE-L-UO2-U-HAA**	**BE-M-UO2-U-HAA**
Al	0.14	0.14	1.13	1.13	0	0
C	0.55	0.55	1.07	1.07	0.37	0.47
Co	0.06	0.06	0.42	0.42	0	0
Cu	0	0	0	0	0.04	0.04
Cr	**56.4**	**56.4**	**109.2**	**108.9**	**38.8**	**3.9**
Mn	2.58	2.58	4.86	4.85	1.81	0.67
Mo	0.23	0.23	0.63	0.63	0	0
N	0	0	0	0	0.33	0.03
Nb	0.41	0.41	1.39	1.39	0	0
Ni	**35.4**	**35.4**	**102**	**102**	**26.9**	**11.7**
P	0.23	0.23	0.33	0.33	0.07	0.06
S	0.04	0.04	0.06	0.06	0.05	0.06
Si	2.44	2.44	4.39	4.38	1.35	0.08
Sn	**12.6**	**12.6**	**17.6**	**17.6**	**8.9**	**7.8**
Ti	1.3	1.3	4.1	4.1	0	0
Zr	**1'109.9**	**1'109.9**	**1'551.6**	**1'551.6**	**786.8**	**688.3**
Fe	**175.6**	**175.6**	**322.6**	**321.6**	**122.9**	**181.7**

3.1.3 Reference canister composition

The reference canister material is a low carbon steel, which consists of almost pure metallic Fe with restricted concentrations of specific minor elements, routinely used in metallurgy to optimize the desired mechanical and corrosion properties. The current reference composition is shown in Tab. 3-3.

Tab. 3-3: Compositional limits (in weight%) for the carbon steel reference material to be used for the fabrication of SF/HLW waste canisters

Modified from Nagra (2024)

Element	**C**	**Si**	**Mn**	**P**	**S**	**Cr**	**Ni**	**Cu**	**Fe**
Weight-%	0.12 max.	0.3 max.	0.8 max.	0.015 max.	0.01 max.	0.2 max.	0.2 max.	0.02 max.	≥ 98.3 (balance)

3.2 Bentonite pore water (BPW)

3.2.1 Initial state of bentonite

Composition and characteristics of bentonite pore waters will depend on the initial state of the compacted bentonite. This includes exchanged cation populations, the protonation state of edge sites in montmorillonite and the content of reactive minor minerals. A precise knowledge of minor minerals inventories is important, since at the high solid/water ratio typical of compacted clays, aqueous and exchanged cation concentrations will react sensitively to their dissolution or precipitation.

Currently, MX-80 Wyoming bentonite is the reference buffer material for backfilling the repository drifts, with the mineral contents, cation exchange capacity (CEC) and exchanged cation populations defined in Tab. 3-3. These data originate from earlier characterization studies on a few selected samples (Müller-Vonmoos & Kahr 1983, Bradbury & Baeyens 2002). Further data on the composition of other bentonites is presented in Jenni et al. (2019) and references therein.

Tab. 3-4: Initial state of MX-80 bentonite used as reactant material in the calculation of BPW compositions

Species/mineral	**Amount** [mol/kg]	**Equivalent fraction**	**Mole fraction**
Exchanged cations			
NaZ	0.668	0.843	0.907
KZ	0.013	0.016	0.018
MgZ_2	0.020	0.051	0.027
CaZ_2	0.033	0.083	0.045
Z_{tot} = CEC	0.787	1	1
Minor minerals			
Gypsum	0.0235		
Quartz	1.66		
Kaolinite	0.039		
Calcite	0.3		
Siderite	0.086		
Magnetite	0.43		

3.2.2 Bentonite pore water model

In saturated bentonite most of the water resides in the interlayer of montmorillonite. The remaining water (inter-particle or external water) consists of an uncharged fraction (the free water, residing in the so-called "anion accessible" porosity, see Van Loon et al. 2007) and of an electrically charged, a few nm-thick fraction in the diffuse double layer (DDL) adjacent to the clay surface. At the pH-range of interest (pH 6 – 8), the surface at frayed edges of clay particles is negatively charged due to an excess of deprotonated ($=XO^-$) sites. This negative, pH-dependent charge leads to anion exclusion and consequently to an excess of charge-compensating cations in the DDL.

At high degrees of compaction, the proportion of DDL water within the external water may become significant, thus complicating the modelling of clay pore water speciation. As a default, geochemical codes can only deal with a single water phase and do not allow the dynamic modelling of the DDL. For the prediction of bentonite pore water compositions in compacted bentonite a specific model (ClaySor model) was developed and implemented in the GEM-Selektor code that allows taking into account surface and DDL charge. Details of the model and its application to derive the bentonite pore waters described in Section 3.2.3 can be found in Kulik et al. (2018) and Curti (2022).

The model assumes that all reactions involving water except cation exchange (ion pair formation, exchange with gas and precipitation/dissolution reactions) take place within the "anion accessible" porosity volume. The pH-dependent clay surface charge is modelled by protonation/deprotonation equilibria following the model of Bradbury & Baeyens (1997). The positive charge excess in the DDL arising from the negative clay surface charge is treated by distributing uniformly an excess of Na^+ ions in the equilibrated external water. A consequence of this approach is that the resulting water has a net charge. Although the interlayer water is formally

not involved in the mentioned equilibria, cation exchange between the hydrated interlayer and the "anion porosity" water is quantified via exchange constants that take into account the specific clay:water ratio corresponding to the desired dry bulk density of the compacted bentonite.

3.2.3 Bentonite pore water compositions

BPW compositions were modelled at standard state conditions (T = 25 °C, p = 1 bar) using the GEM-Selektor code (Kulik et al. 2013) and the recently updated PSI thermodynamic database TDB2020 (Hummel & Thoenen 2022). In the simulations, Opalinus Clay porewater (OPAw) filling the "anion accessible" porosity reacts with minor minerals in MX-80 bentonite (carbonates, gypsum, carbonates, kaolinite, pyrite) and with a predefined population of exchangeable cations in montmorillonite. The bentonite is treated as inert cation exchanger pre-compacted to a dry density of 1'450 kg m^{-3}.

OPAw compositions were defined based on analyses of water extracts from the recent Nagra borehole campaign in the "Nördlich Lägern" (NL) and "Zürich Nordost" (ZNO) region. This water has salinities intermediate between those of waters sampled in the "Jura Ost" (JO) region and from the Bülach borehole. Three BPWs were defined, corresponding to three different imposed carbon dioxide partial pressures (Tab. 3-5) reflecting the expected range in the Opalinus Clay formation (Mäder & Wersin 2022).

Three additional BPWs were calculated to cover the regional differences observed during the borehole campaign (Tab. 3-6). "Bülach water" was modelled starting from extracts sampled from the homonymous borehole in the NL region. This water is of particular interest because it has the highest salinity among all waters extracted during the deep drilling campaign. The other two BPWs listed in Tab. 3-6 ("low salinity water" and "high salinity water") were defined by

subtracting/ adding appropriate NaCl amounts to the E3-OPW-Ref water and then recalculating the BPW enforcing the required saturation equilibria and a pCO_2 of $10^{-2.2}$ bar. They represent bounding values for the salinities of Opalinus Clay pore water (i.e. ionic strengths of 0.15 M and 1.0 M, respectively) as observed also outside the SGT-E3 borehole campaign region (e.g. Mt. Russelin water in the Mt. Terri region, see Mazurek & de Haller 2017).

In spite of the wide regional and salinity ranges, the six BPW compositions are fairly similar and fall within narrow ranges of pH (6.9 to 7.5) and redox potential (Eh (-159 to -189 mV). The similarities are a consequence of chemical buffering mechanisms provided by the minor minerals (particularly gypsum and carbonates) in combination with the fixed pCO_2 ranges and exchange/sorption equilibria in the clay. The Eh is regulated by equilibria among minor iron minerals present in the bentonite (siderite, pyrite) and magnetite (representing Fe corrosion products). For systems at thermodynamic equilibrium with fixed pCO_2 and constant *T, p*, it can be demonstrated that the pH is only a function of the sulphate ion activity, *as long as calcite and gypsum are present*. This constraint can be derived from equilibrium relations for the reaction

$$CaCO_3(s) + 2\ H^+ + SO_4^{2-} + H_2O <=> CaSO_4{*}2H_2O(s) + CO_2(g) \qquad \log K^0_r = 14.26$$

which leads to following equation:

$$pH = \frac{\log K_r^0 - \log p_{CO_2} + \log a_{SO_4^{2-}}}{2}$$

For all BPWs listed in Tab. 3-5 and Tab. 3-6 with sulphate concentrations varying moderately (45 – 102 mM) the full GEM-Selektor calculations obey the above relation, explaining the narrow, near-neutral pH-range.

The formation of strong U(VI)-carbonate complexes may increase the solubility of uranium in water. Our BPW calculations predict total carbonate concentrations in the 1 – 5 mM range. For the reference bentonite pore water E3-BPW-Ref with 3 mM carbonate, a total U solubility limit of about 3×10^{-8} M and a reducing Eh (-173 mV) were calculated. This solubility, although quite low, is about ten times higher than usually predicted under reducing conditions at equilibrium with amorphous UO_2. The inspection of the results (Tab. 3-7) reveals that even at these comparatively low carbonate levels, carbonate complexes contribute 99.9% of the total dissolved uranium. The dominant species are the two ternary $Ca\text{-}U^{VI}\text{-}CO_3$ complexes, which sum to more than 90% of the dissolved uranium. It can be anticipated, however, that in a more reducing environment such as expected inside the corroding canister, all U(VI)-carbonate complexes will be destabilized, yielding, as expected, a UO_2 solubility in the range of 10^{-9} M or less (see Section 3.7).

Tab. 3-5: pCO_2, pH, Eh, ionic strength and total element concentrations of bentonite pore waters computed for the NL-ZNO region compared to the reacting Opalinus Clay Waters (in grey)

Description	**low pCO_2**		**reference BPW**		**high pCO_2**	
Calc. ID	**E3-OPW_lowpCO2**	**E3-BPW_lowpCO2**	**E3-OPW-Ref**	**E3-BPW-Ref**	**E3-OPW_highpCO2**	**E3-BPW_highpCO2**
log p(CO_2)/bar	-2.79	-2.80	**-2.20**	**-2.20**	-1.80	-1.80
pH	7.40	7.51	**7.10**	**7.24**	6.90	7.05
Eh	-0.190	-0.194	**-0.167**	**-0.173**	-0.152	-0.159
IS /m	0.317	0.452	**0.319**	**0.452**	0.321	0.453
***Aqueous concentrations** [mol/kgw]*						
Al	2.13E-08	2.45E-08	**2.09E-08**	**2.08E-08**	2.86E-08	2.39E-08
Ba	1.56E-07	7.84E-08	**1.57E-07**	**7.19E-08**	1.58E-07	6.85E-08
C(IV)	1.07E-03	1.37E-03	**2.21E-03**	**2.94E-03**	3.68E-03	4.99E-03
Ca	2.01E-02	1.92E-02	**2.03E-02**	**1.77E-02**	2.05E-02	1.69E-02
Cl	0.239	0.238	**0.240**	**0.239**	0.241	0.240
F	1.74E-04	1.74E-04	**1.74E-04**	**1.74E-04**	1.74E-04	1.74E-04
Fe	7.14E-06	6.42E-06	**2.56E-05**	**2.09E-05**	5.95E-05	4.65E-05
K	2.13E-03	1.92E-03	**2.13E-03**	**1.83E-03**	2.14E-03	1.79E-03
Mg	1.43E-02	1.12E-02	**1.45E-02**	**1.02E-02**	1.46E-02	9.77E-03
Mn	8.16E-05	1.82E-05	**8.24E-05**	**1.84E-05**	8.33E-05	1.86E-05
Na	0.215	0.391	**0.215**	**0.375**	0.216	0.366
S(VI)	2.29E-02	7.16E-02	**2.29E-02**	**7.86E-02**	2.29E-02	8.29E-02
Si	1.73E-04	1.70E-04	**1.72E-04**	**1.70E-04**	1.72E-04	1.70E-04
Sr	3.67E-04	1.87E-04	**3.70E-04**	**1.72E-04**	3.73E-04	1.64E-04

Tab. 3-6: pCO_2, pH, Eh, ionic strength and total element concentrations of bentonite pore waters for the Bülach site and for the reference case assuming bounding salinity values, compared to the reacting Opalinus Clay Water (in grey)

Description	**Bülach water**		**Low salinity water**		**High salinity water**	
Calc. ID	**E3-OPW_sal**	**E3-BPW_sal**	**E3-OPW-Ref-ls**	**E3-BPW-Ref-ls**	**E3-OPW-Ref-hs**	**E3-BPW-Ref-hs**
log p(CO_2)/bar	-2.81	-2.80	-2.11	-2.20	-2.35	-2.21
pH	7.37	7.42	7.04	7.33	7.20	6.97
Eh	-0.187	-0.189	-0.161	-0.179	-0.177	-0.157
IS /m	0.509	0.592	0.151	0.353	1.007	1.084
***Aqueous concentrations** [mol/kgw]*						
Al	2.05E-08	2.21E-08	2.10E-08	2.07E-08	2.14E-08	1.90E-08
Ba	1.81E-07	1.13E-07	9.90E-08	5.12E-08	3.97E-07	2.38E-07
C(IV)	1.02E-03	1.19E-03	2.15E-03	3.48E-03	2.29E-03	2.00E-03
Ca	2.90E-02	2.71E-02	2.02E-02	1.29E-02	2.03E-02	5.40E-02
Cl	0.407	0.405	0.078	0.078	0.924	0.922
F	1.71E-04	1.70E-04	1.55E-04	1.54E-04	2.12E-04	1.65E-04
Fe	9.08E-06	8.49E-06	3.07E-05	1.64E-05	1.99E-05	5.35E-05
K	2.74E-03	2.41E-03	2.13E-03	1.44E-03	2.13E-03	3.89E-03
Mg	1.89E-02	1.56E-02	1.45E-02	7.45E-03	1.45E-02	2.98E-02
Mn	1.07E-04	1.83E-05	8.46E-05	1.82E-05	6.61E-05	1.90E-05
Na	0.368	0.496	0.054	0.289	0.900	0.845
S(VI)	2.98E-02	5.91E-02	2.28E-02	1.02E-01	2.34E-02	4.54E-02
Si	1.68E-04	1.66E-04	1.77E-04	1.74E-04	1.53E-04	1.53E-04
Sr	4.19E-04	1.87E-04	2.39E-04	1.25E-04	3.73E-04	1.64E-04

Tab. 3-7: Calculated speciation at the U solubility limit in the reference bentonite pore water (E3-BPW-Ref)

Species	**Molality**	**%**
$Ca_2U^{VI}O_2(CO_3)_3(aq)$	2.16E-08	70.13
$CaU^{VI}O_2(CO_3)_3^{2-}$	6.54E-09	21.20
$Mg_2U^{VI}O_2(CO_3)_3(aq)$	1.63E-12	0.01
$MgU^{VI}O_2(CO_3)_3^{2-}$	6.37E-10	2.06
$U^{VI}O_2CO_3F^-$	2.15E-12	0.01
$U^{VI}O_2(CO_3)_3^{4-}$	1.73E-09	5.60
$U^{IV}CO_3(OH)_3^-$	1.99E-10	0.65
$U^{VI}O_2(VI)(CO_3)_2^{2-}$	7.83E-11	0.25
$U^{VI}O_2\,CO_3(aq)$	2.14E-12	0.01

Tab. 3-7: Cont.

Species	Molality	%
U-carbonate complexes	3.08E-08	99.92
$U^{V}O_2^+$	7.95E-12	0.03
$U^{IV}(OH)_4(aq)$	1.70E-11	0.05
Other U complexes	2.49E-11	0.08
U(total)	**3.09E-08**	**100**

3.3 Corrosion of iron

Carbon steel canisters are designed to isolate the spent fuel assemblies during at least 10'000 years after waste emplacement. At that time , temperatures will have reached equilibrium with the host-rock (~ 40 – 50 °C).

For the vast majority of the lifetime of the canister steel corrosion will proceed exclusively anaerobically:

$$3\ Fe(s) + 4\ H_2O \rightarrow Fe_3O_4(s) + 4\ H_2(g) \quad (3.1)$$

Molecular hydrogen (H_2) is the major gas component produced (Diomidis et al. 2016). Compared with other gases, it has a very low solubility in water (0.78 mmol/kgw at 25 °C, see Miron (in prep), which may lead to pressure build-up (see Sections 3.7.3 and 5.3) and water displacement in the confined repository environment.

Canister corrosion will also produce mobile ferrous ions (Hofstetter et al. 2014). According to the calculations in Section 3.6, Fe(II) concentrations inside the corroding canisters will rise to about 70 µM, while lower Fe(II) concentrations are predicted for OPAw and BPW (6 – 54 µM).

3.4 Buffer saturation times and gas pressure buildup

Senger et al. (2014) developed a 3-D thermo-hydraulic model to predict the initial evolution of the repository near field after waste emplacement and closure. When applied to a mixed MOX/SF canister, corresponding to the highest heat output evolution among the different types of SF waste, the model predicts buffer resaturation within about 100 years, as indicated by relative humidity approaching 100%. Prior to this time, temperatures in bentonite exceed 100 °C, with a peak at 135 °C about 5 years after waste emplacement (see Curti et al. 2023). During this period, partially saturated conditions prevail, particularly in the internal section of the bentonite buffer, where even dry conditions are reached temporarily. As soon as the bentonite is resaturated, steel corrosion leads to a steep increase in gas pressure. Thereafter, gas pressure decreases to about 50 – 60 bars at the expected canister failure times ($\geq 10^4$ a). By that time, temperatures will have reached equilibrium with the host-rock (~ 40 – 50 °C).

A key result of Senger et al. (2014) is that conditions in the bentonite should remain fully saturated between 100 and 60'000 years, i.e. unsaturated conditions are unlikely at canister failure time.

3.5 Canister breaching and ingress of water

The carbon steel canisters are fabricated to isolate the waste for a period of at least 10'000 years. After this time or later, canister breaching will occur by a combination of environmental degradation and mechanical stress.

Once cracks intersecting the full thickness of the canister are formed, water from the saturated bentonite will infiltrate into the cavities inside the canister. Corrosion of the waste package and the so-far intact internal surfaces of the canister will then start, so that anaerobic iron corrosion and gas production will presumably intensify soon after failure. It is estimated that carbon steel corrosion will cease after about 40'000 years, assuming a canister wall thickness of 14 cm and a corrosion rate of 0.002 mm/a. The water will come into contact with Zircaloy cladding, other structural materials (mainly Ni-Cr alloys) and the SF pellets. (No credit is given to the integrity of the thin and brittle Zircaloy cladding). This will start corrosion reactions for the metallic materials as well as radionuclide release.

3.6 Chemical reactivity of H_2 and kinetic constraints on redox reactions

Hydrogen is a reductant which is usually kinetically hindered at repository temperature, but catalysts such as microbes or bacteria could make its reaction with oxidants possible. If the hydrogen produced via canister corrosion were reactive, it may be consumed by various redox reactions. Repository materials and pore water contain different amounts of redox-sensitive species in their oxidized forms (mainly carbonate, Fe(III) and sulphate) which could potentially react with the generated hydrogen, leading to the formation of reduced species and solids (e.g., methane, siderite, pyrite/pyrrhotite). Normally, however, molecular hydrogen is chemically inert at temperatures below 150 °C and in the absence of microbial mediation (McCollom & Seewald 2001, Thom & Anderson 2008, Truche et al. 2009).

Microbial life is however highly restricted in compacted MX-80 bentonite at dry densities $\geq$ 1'450 kg m^{-3} and water activities < 0.96 (see Jenni et al. 2019).

There are cases, however, where hydrogen is chemically activated without microbial mediation. One such mechanism that is relevant for the repository system is the surface mediated activation of hydrogen at the spent fuel surface (see also Chapter 5). Activation of dissolved H_2 has been demonstrated to occur both on the UO_2 surface (in the presence of radiation) and (catalytically) on exposed surfaces of noble metal inclusions in spent fuel via decomposition of adsorbed molecular hydrogen to $H^{\cdot}$ radicals (see explanations and Fig. 61 in Badley & Shoesmith 2022). Both pathways prevent U(IV) oxidation and thus protect the fuel from radiolytic oxidation. These processes, being limited by the adsorption of H_2 on the fuel surface should remain localized and capable of activating only a small fraction of the large amounts of H_2 produced by canister corrosion. While the rate of H_2 activation on the UO_2 surface under irradiation cannot exceed the rate of radiolytic oxidant production and will thus continuously decrease with time no such limitation applies to the catalytic pathway mediated by noble metal inclusions. This mechanism will therefore continue to protect the fuel from oxidation at all times.

3.7 Chemical evolution inside the failed canister

3.7.1 Model outline

The simulation of the chemical processes within the failed canister presented here assumes fully saturated conditions within the canister because it currently cannot be reliably implemented for coupled chemical processes under unsaturated conditions. This corresponds to the simulations of the dose calculations, which are also conservatively limited to fully saturated conditions, which are performed with the STMAN code (Nagra 2002, Robinson 2022).

To this aim, the batch reaction model described in Curti (2021) is applied with updated pore water composition and chemical inventories. The model assumes abrupt canister failure via formation of a fissure in the canister. Bentonite pore water (E3-BPW-Ref-un[1]) then intrudes and fills all empty cavities inside the spent fuel canister. According to the current design the empty space in the intact loaded canister is 2 m^3 for PWR fuel (4 assemblies/canister) and 1.7 m^3 for BWR fuel (12 assemblies/canister). No reduction of the void volume via formation of Fe-corrosion products[2] inside the canister is considered. Furthermore, it is assumed that at failure time the steel canister will have been partially altered to magnetite, so that saturation equilibrium with this mineral is always maintained. The amounts of solids allowed to react with the water inside the canister are defined through a scaling procedure which takes into account the different corrosion rates of the materials involved (spent fuel, steel, Zircaloy and structural materials) as well as the diffusive water flux from bentonite. This procedure is briefly described in Section 3.7.2 and in more detail in Curti (2021).

3.7.2 Chemical inventories, model parameters and boundary conditions

A major aim was to carry out simulations reflecting both chemical complexity and corrosion kinetics of the materials involved. Therefore, updated values of corrosion rates and the detailed chemical data for the spent fuel waste type BE-L-UO2-U-HAA (Leibstadt UO_2 spent fuel, including compositions of Zircaloy and other structural materials) were used.

The elemental inventories are first normalised to 1 L of aqueous solution inside the canister (i.e. divided by 1'700 L). These are listed in the first column of Tab. 3-8. The second column ("scaled inventory") takes into account that spent fuel, Zircaloy and structural materials corrode at much slower rates than the canister. Accordingly, these inventories are reduced by a factor equal to the ratio of the corrosion rate of the mentioned materials to the carbon steel corrosion rate of 2 μm a^{-1} from Diomidis et al. (2016, p. 18), corresponding to a surface normalised rate of 8.9×10^{-9} mol m^{-2} s^{-1} for a steel density of 7'860 kg m^{-3}. Zircaloy corrodes very slowly due to surface passivation following the formation of a protective ZrO_2 film. A linear corrosion rate of 10^{-8} m/a was conservatively selected, which corresponds to a surface normalized corrosion rate of 2.24×10^{-11} mol m^{-2} s^{-1}. For simplicity, the Zircaloy corrosion rate was assumed also for other structural materials (e.g. end pieces and springs in the fuel assemblies).

---

[1] This is a charge-balanced version of the reference bentonite porewater E3-BPW-Ref discussed in Curti (2022) obtained by removing the excess positive charge ascribed to the diffuse double layer via subtraction of NaCl. This step is necessary to avoid an electrically charged system inside the canister.

[2] Corrosion products such as magnetite and other secondary solids have a much higher molar volume than carbon steel.

The spent fuel dissolution rate was determined following the procedure described in Appendix 1 of Curti (2021). This involved first determining an average corrosion rate (6.5×10^{-13} mol m^{-2} s^{-1}) from the range ($0.3 – 1.0 \times 10^{-12}$ mol m^{-2} s^{-1}) reported in Section 6.4 of Nagra (2005), then multiplying this value by a factor of ten to account for the increase in surface area due to water accessible cracks in the spent fuel pellets. This resulted in a final selected spent fuel corrosion rate of 6.5×10^{-12} mol m^{-2} s^{-1}.

The third column in Tab. 3-8 ("reactive inventory") specifies the amount of "scaled inventory" effectively allowed to react with 1 L of bentonite pore water. It implies a further normalization step, which takes into account the estimated *diffusive water flux* from bentonite into the cavities inside the canister. The model is consistent with the conservative repository evolution scenario followed in the safety assessment model (Grindrod et al. 1991, Nagra 2002), which assumes fully saturated conditions and instantaneous filling of the void spaces between waste package and canister[3]. A more realistic, however, less conservative and hardly quantifiable scenario, is described in Sections 3.4 and 3.5.

In order to simulate the diffusive exchange of water and solutes between bentonite and the water-filled volume inside the canister without resorting to reactive transport simulations, we proceeded as follows. Using a mean water self-diffusion coefficient of 5.97×10^{-11} m^2 s^{-1} from experimental data on the diffusion of tritiated water in bentonite (Bestel et al. 2018) a steady state diffusive flux of 1.1×10^{-4} mol s^{-1} across the bentonite/waste package interface was determined. At this flux, the initial water and solutes filling the void volume inside the canister (1.7 m^3) will be exchanged (without any advection) within 28.2 years under the hypothetical assumption of a steady state flux. This time and the geometric surfaces were then multiplied with the surface normalised corrosion rates to scale the amounts of reacting solids to the diffusive flux of water and solutes in the simulation. At a corrosion rate of 2 μm/a and a constant water flux, the fraction of steel canister material corroded during this time is calculated to be 4.03×10^{-4}, which leads (in combination with the scaling factors for lower corrosion rates of the other materials) to the "reactive inventories" listed in Tab. 3-8. The technical details of these calculations can be found in Appendix 1 and 2 of Curti (2021).

In the simulations, the "reactive inventories" are equilibrated with 1 L of BPW, assuming either unconstrained or externally fixed pCO_2. The calculations were carried out, as for the reference BPW calculations, using version 3.9.0 of the GEM-Selektor code (Kulik et al. 2013). Contrary to the calculations in Curti (2021), only stoichiometric solids included in the recently updated PSI-Nagra database TDB 2020 (Hummel & Thoenen 2022) were considered. Other potentially forming secondary solids (ankerite) and solid solutions such as ternary (Ca, Mg, Fe)CO_3 were excluded due to the limited reliability of the thermodynamic data and/or mixing parameters. Moreover, based on the experimental evidence that sulphate reduction and methanogenesis are likely to be kinetically inhibited inside the failed canister (see Section 3.6), reduction of carbonate and sulphate species were intentionally suppressed in the calculations. Moreover, it seems unlikely that H_2 activation mechanisms analogous to those described in Section 3.6 could operate on other metallic or non-metallic surfaces present in the environment of interest (e.g. steel, Zircaloy, Cr-Ni alloys, Fe corrosion products). Radiolytic decomposition of adsorbed H_2 cannot take place away of the fuel surface and the catalytic properties of such materials can hardly be superior to those of noble metals. Finally, in the absence of experimental data there is no reason to assume H_2 activation on the surface of materials other than spent fuel.

[3] In a previous safety case calculations, the water-filled void volume is represented as "reservoir thickness" of a continuous annular volume separating waste from the bentonite, see Grindrod et al. (1991) and Table A3.3-1, parameter 15 in Nagra (2002).

Tab. 3-8: Chemical inventories of solid materials inside the canister

Elements not included in the calculation because they are not part of the TDB2020 thermodynamic database (Cr, Cu) are greyed out.

Material	**Element**	**Normalized inventory**[1] [mol/L]	**Scaled inventory**[2] [mol/L]	**Reactive inventory**[3] [mol/L]
Steel canister	C	1.34	1.34	5.40E-04
	Mn	1.95	1.95	7.87E-04
	P	6.50E-02	6.50E-02	2.62E-05
	S	4.18E-02	4.18E-02	1.69E-05
	Si	1.43	1.43	5.77E-04
	Cr	5.16E-01	5.16E-01	2.08E-04
	Ni	0.457	0.457	1.84E-04
	Cu	4.22E-02	4.22E-02	1.70E-05
	Fe	236.2	236.2	9.52E-02
Zircaloy	Zr	5.55	1.39E-02	5.62E-06
	Sn	6.30E-02	1.58E-04	6.37E-08
Structural materials	Cr	0.274	6.87E-04	2.77E-07
	Mn	1.28E-02	3.21E-05	1.29E-08
	Si	9.52E-03	2.39E-05	9.62E-09
	Fe	0.868	2.18E-03	8.77E-07
	Ni	0.19	4.77E-04	1.92E-07
Spent fuel	U	5.28	3.85E-03	1.55E-06
	Pu	4.62E-02	3.36E-05	1.35E-08
Oxygen (by balance)[4]		311.32	300.67	0.121

[1] The inventories were normalized to 1 L of solution in the cavities inside the canister.
[2] The inventory of each material is reduced proportionally to the ratio of material: canister corrosion rate.
[3] Effective amounts of element equilibrated assuming a FCR (Fraction of Canister Reacted) of 4.03×10^{-4}.
[4] Assumes contributions of half Fe in the canister as magnetite, in addition to UO_2 and PuO_2.

3.7.3 Results of calculations

Two calculations were carried out, differing in the treatment of the gas phase (Tab. 3-9). In the calculation denoted INCAN 2a_3, thermodynamic equilibrium was calculated without external constraints on pCO_2, implying that no exchange of dissolved carbon dioxide between bentonite and the canister interior was allowed (closed system conditions). This calculation yields a mildly alkaline, strongly reduced solution (pH 8.4, Eh -495 mV) in equilibrium with a H_2-rich gas phase and a pCO_2 ($10^{-4.5}$ bar) more than two orders of magnitude lower than in the bentonite and host-rock ($10^{-2.2}$ bar). This result implies a concentration gradient such that carbonic acid dissolved in the bentonite pore water would diffuse towards the canister if equilibration were allowed.

Calculation INCAN 2a_2 is identical to the former, except that the pCO_2 was fixed to $10^{-2.2}$ bar as for the reference bentonite pore water. This implies that in-diffusion of dissolved carbon dioxide from bentonite into the canister cavity is now allowed until the equilibrium pCO_2 inside the canister equals that in the bentonite. The result is a slightly less alkaline and less reducing solution (pH 7.24, Eh -222 mV) similar to the pristine bentonite pore water, in equilibrium with a gas phase now containing only traces of hydrogen. This calculation represents long-term equilibrium when iron corrosion is complete and the generated hydrogen has escaped (> 100'000 years after waste emplacement), while calculation INCAN 2a_3 simulates conditions shortly after canister failure (assumed in the reference evolution scenario to occur after ≥ 10'000 years after waste emplacement). The two calculations thus represent two limiting cases of the expected chemical evolution inside the canister. As long as steel corrosion is active, hydrogen partial pressures will be substantial and surely above the critical thresholds in the $10^{-5} – 10^{-4}$ bar range necessary to ensure protection from oxidative fuel dissolution (see Section 5.6). Note also that the calculations were carried out at a total pressure of 1 bar, far below the hydrostatic pressures expected in the repository environment. Taking into account realistic pressures would increase the availability of hydrogen. It has been demonstrated that even very small amounts of hydrogen are sufficient to prevent fast oxidative dissolution of the fuel (Pastina and Laverne 2021) via surface mediated mechanisms. According to Trummer and Jonsson (2010) the critical H_2 concentration, below which such protective effect vanishes, is 5.4×10^{-9} M, corresponding to hydrogen partial pressures of 3.8×10^{-5} bar, at the earliest possible canister failure time. These mechanisms will be further discussed in Section 5.6.

Tab. 3-9 also reports the calculated solubility limiting solids for each listed element. Soluble elements (Na, K, Cl) are undersaturated with all potentially precipitating solids included in the database. Aluminium, somewhat surprisingly, also does not reach saturation with respect to any solid, due to the fact that the intruding BPW has already a very low aluminium concentration (limited by kaolinite) and no other significant Al source is present in the reacting chemical inventory inside the canister. For all other elements, the final equilibrium concentration is limited by precipitation of sparingly soluble solids mostly corresponding to expectations, with few notable exceptions.

For instance, phosphorous is limited by precipitation of small amounts of F-apatite, $Ca_5(PO_4)_3F$(cr), in spite of the very low content in carbon steel (0.015 wt.%), which translates into a reactive inventory of only 26.2 µmol/L (Tab. 3-9). This amount is nevertheless sufficient, in combination with relatively high Ca and F concentrations (16 – 17 mmol/L and 0.17 mmol/L, respectively), to generate an ion activity product reaching the solubility product of F-apatite. Phosphate is also found to limit the concentration of Pu in the case of unconstrained pCO_2 (INCAN 2a_3), a result in-line with that reported in analogous calculations by Bradbury et al. (2014), which had cast some doubts due to the incompleteness of thermodynamic data at that time. The present results are more robust due to large improvements in the thermodynamic database for phosphorous (Hummel & Thoenen 2022).

Finally, coffinite ($USiO_4$), rather than amorphous UO_2, is determined to be the solubility-limiting phase for uranium. This fixes the aqueous U concentrations to very low values in the two reported calculations (0.03 – 0.9 nmol/L). This result is also an effect of changes in the thermodynamic database, which are discussed later in Section 6.3.

Tab. 3-9: Results of speciation calculations to determine aqueous, gas and solid equilibria in the water permeating the open space inside a failed canister loaded with BWR UO_2 fuel, compared with the initial composition of the reacting bentonite pore water

	E3-BPW-Ref-un Reacting bentonite pore water	**INCAN 2a_2** Constrained pCO_2	**INCAN 2a_3** Unconstrained pCO_2	**Limiting solids** (INCAN 2a_2/3)
IS(m)	0.434	0.434	0.432	
pH	7.25	7.24	8.40	
Eh(V)	-0.175	-0.222	-0.495	
log $p(CO_2)$	-2.22	-2.20	-4.51	
log $p(H_2)$	-8.58	-6.95	**-0.03**	
log $p(N_2)$	-0.008	-0.007	**-1.162**	
log $p(O_2)$	-65.9	-69.2	-83.0	
Main elements	*mol/kgw*	*mol/kgw*	*mol/kgw*	
Al	2.08E-08	2.08E-08	2.08E-08	-
Ba	6.94E-08	7.00E-08	8.34E-08	$BaSO_4$(cr)
C(in)	2.94E-03	2.94E-03	2.20E-04	$CaMg(CO_3)_2$(cr), $CaCO_3$(calcite)
Ca	1.71E-02	1.69E-02	1.64E-02	$CaCO_3$(calcite)
Cl	0.239	0.239	0.239	-
F	1.74E-04	1.65E-04	1.65E-04	$Ca_5(PO_4)_3F$(cr)
Fe	2.05E-05	**7.22E-05**	**7.08E-05**	$FeCO_3$(cr) + Fe_3O_4
K	1.83E-03	1.83E-03	1.83E-03	-
Mg	1.02E-02	1.01E-02	9.58E-03	$CaMg(CO_3)_2$
Mn	1.84E-05	**6.21E-05**	**5.94E-05**	$MnCO_3$(cr)
Na	0.341	0.341	0.341	-
Ni	-	1.85E-04	3.70E-05	$Ni(OH)_2$(cr)
P	-	9.59E-09	6.59E-10	$Ca_5(PO_4)_3F$(cr)
Pu	-	3.61E-08	6.32E-08	$Pu(OH)_3$(am) / $PuPO_4$(am_hyd)
S	7.80E-02	7.70E-02	7.78E-02	$SrSO_4$(cr)
Si	1.70E-04	1.95E-04	2.06E-04	SiO_2(cr)
Sn	-	8.96E-09	1.71E-08	SnO_2(cr)
Sr	1.66E-04	1.67E-04	1.64E-04	$SrSO_4$(cr)
U	-	8.86E-10	3.14E-11	$USiO_4$(cr)
Zr	-	6.23E-10	6.23E-10	ZrO_2(cr)

Although coffinite is the solubility-limiting solid in both INCAN 2a_2 and INCAN 2a_3 calculations, the calculated equilibrium uranium concentrations differ by more than an order of magnitude. This is due (as anticipated in Section 3.2.3) to the redox-dependent stability of uranyl carbonate complexes. In the former equilibrium (with pCO_2 fixed at $10^{-2.2}$ bar) the calculated Eh (-222 mV) is only 50 mV lower than in the bentonite pore water E3-BPW-Ref (also with pCO_2 fixed at $10^{-2.2}$ bar), implying that the ternary Ca-U^{VI}-CO_3 complexes are still fairly stable (Tab. 3-10). In contrast, the calculation INCAN 2a_3 with unconstrained pCO_2 reaches equilibrium at significantly higher pH and lower Eh, leading to full destabilization of the aforementioned complexes and thus to a much lower final U concentration. This result is important, as it implies that the UO_2 solubility is a function of the assumption made on pCO_2 equilibration. Diffusion of dissolved carbon dioxide from an external reservoir will eventually favour higher U concentrations, compared to a system inside the canister that remains more or less closed to CO_2 exchange.

Tab. 3-10: Calculated U speciation in pore waters inside the failed canister

Species	**INCAN 2a_2**		**INCAN 2a_3**	
	Molality	**%**	**Molality**	**%**
$Ca_2U^{VI}O_2(CO_3)_3(aq)$	4.69E-10	52.9	< 1E-13	0.0
$CaU^{VI}O_2(CO_3)_3^{2-}$	1.44E-10	16.3	< 1E-13	0.0
$Mg_2U^{VI}O_2(CO_3)_3(aq)$	< 1E-13	0.0	< 1E-13	0.0
$MgU^{VI}O_2(CO_3)_3^{2-}$	1.45E-11	1.6	< 1E-13	0.0
$U^{VI}O_2CO_3F^-$	< 1E-13	0.0	< 1E-13	0.0
$U^{VI}O_2(CO_3)_3^{4-}$	3.80E-11	4.3	< 1E-13	0.0
$U^{IV}CO_3(OH)_3^-$	2.00E-10	22.6	1.44E-11	45.8
$U^{VI}O_2(VI)(CO_3)_2^{2-}$	1.74E-12	0.2	< 1E-13	0.0
$U^{VI}O_2\,CO_3(aq)$	< 1E-13	0.01	< 1E-13	0.00
U-carbonate complexes	8.67E-10	97.9	1.44E-11	45.8
$U^{V}O_2^+$	1.17E-12	0.1	< 1E-13	0.0
$U^{IV}(OH)_4(aq)$	1.70E-11	1.9	1.70E-11	54.2
Other U complexes	1.82E-11	2.1	1.70E-11	54.2
U(total)	8.85E-10	100.0	3.14E-11	100.0

3.8 Implications of chemical conditions for spent fuel dissolution

The objective of the two calculations presented in Section 3.7 was to identify major parameters controlling the *bulk chemical conditions* inside the failed canister and to provide corresponding ranges of composition, pH and redox conditions. For this purpose, two bounding calculations were carried out reflecting limiting conditions for the exchange of CO_2 between water inside the canister and the bentonite buffer (INCAN 2a_2 and INCAN 2a_3, see Tab. 3-9), under the assumptions that sulphate/carbonate are not reducible and that H_2 is chemically inert. The results define relatively narrow windows of pH (7.2 to 8.4), Eh (-222 to -495 mV) and total carbonate concentrations (2.9 to 0.2 mmol/kgw).

An interesting result is that equilibrium U concentrations (and thus the spent fuel non-oxidative dissolution rates) depend on the pCO_2 conditions established inside the canister. In the calculation representing conditions shortly after failure (INCAN_2a_3), the reaction between bentonite pore water and the solid materials (mainly the canister) first reduces the local pCO_2, establishing an inward diffusion gradient of CO_2(aq). With time, in-diffusion of CO_2(aq) reduces the pH and increases the Eh of the water inside the canister. Through the pH reduction the Ca concentration increases via calcite equilibrium, which in turn stabilizes ternary Ca-uranyl-carbonate complexes. This leads to a somewhat higher U concentration in the limiting case of the long-term evolution, when the CO_2(aq) gradient no longer exists (INCAN_2a_2). The predicted increase in U concentration is however not a point of concern since it is negligible (from 0.03 to 0.9 nM) compared to the potential effect of radiolytic oxidation, therefore, it will not have an impact on the dissolution of the spent fuel matrix.

A further notable result is that the U(IV) silicate coffinite is predicted to limit uranium solubility instead of amorphous U(IV) oxide. This result is a direct consequence of the new data selected for this compound in the TDB2020 thermodynamic database. Considering the still large remaining uncertainties in thermodynamic data, the question whether coffinite or amorphous UO_2 will be the most stable U(IV) phase in the system of interest cannot be resolved conclusively. This issue is not purely academic, considering the potential consequences of coffinitization on spent fuel dissolution kinetics and radionuclide release.

If sufficient dissolved silica were available, it is conceivable that extensive transformation of UO_2 to coffinite would occur. Nevertheless, from the results of the speciation calculation it can be argued that the availability of silica will be limited. Indeed, the comparison of bentonite pore water (Tab. 3-5 and Tab. 3-6) and "inside canister" water compositions (Tab. 3-9) indicate similar silica concentrations in both compartments, implying negligible fluxes of Si from bentonite towards the fuel (if any). Under such circumstances, the silica will remains stored as SiO_2 and coffinitization would be minor. The almost equal silica concentrations inside the canister and in bentonite simply result from equilibrium with the same SiO_2 phase (quartz) in the two compartments and the fact that this equilibrium (contrary to calcite equilibrium) does not depend on pCO_2 or pH within the ranges of interest. Data from natural analogues (Wang & Xu 1999, Evins & Jensen 2012) confirm that coffinitization of uraninite is usually minor and favoured in silica-rich environments ([Si] $\geq 10^{-3}$ M). Further evidence and a discussion on the thermodynamics of coffinitization is provided in Chapter 6.

4 Instant release fractions of radionuclides

4.1 Correlations of the IRF of Cs and I with FGR

The group of volatile or semi-volatile elements (Xe, Kr, Cs and I) has been widely studied in fuel engineering, reactor safety and waste management studies and there is a large body of data on their behaviour as a function of linear power rating and burn-up.

It has been shown that the IRF of ^{137}Cs and ^{129}I in short-term leaching experiments correlates well with the FGR of the fuel. A typical example is shown in Fig. 4-1, which shows that the cumulative release fraction of ^{129}I asymptotically approaches the measured FGR, whereas the ^{137}Cs is substantially smaller.

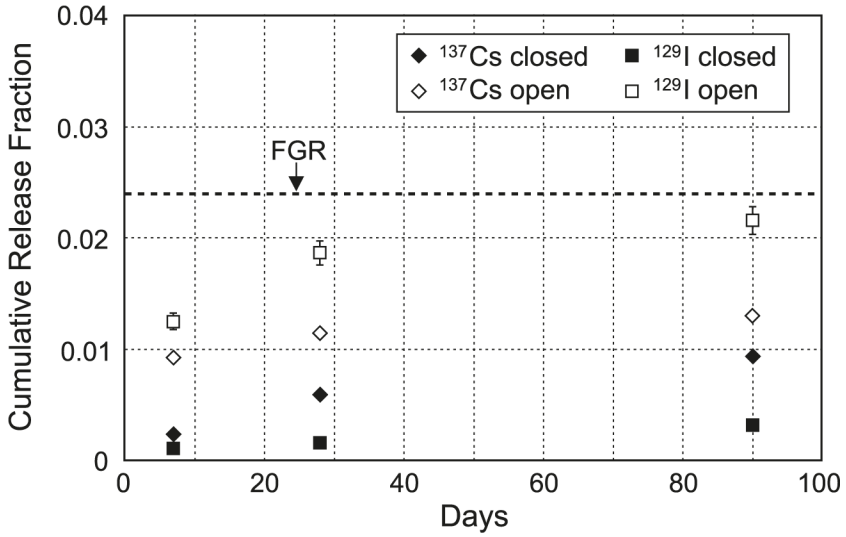

Fig. 4-1: Cumulative fractional release of ^{137}Cs and ^{129}I from Ringhals PWR fuel samples with a burn-up of 61.4 MWd/kg$_{iHM}$

The terms closed and open refer to clad samples and samples with the cladding pried open to release the fragments, respectively. From Johnson et al. (2012) reprinted with permission from the publisher

This correlation has a good mechanistic basis, as the diffusion coefficients of Xe and I in UO_2 in reactor are approximately the same (Lewis et al. 1990). Walker et al. (1996) report that Cs and Xe diffusion coefficients are the same, whereas Lassman et al. (2002) based on a more detailed analysis, report a diffusion coefficient for Cs that is 1/3 the value for Xe. Some differences in volatility exist, however, as Cs is volatile at the high temperatures of the fuel rod centre but condenses below about 1'200 °C at the high internal pressure of a fuel rod (Walker et al. 1996), whereas both Xe and I are gases under such conditions. How these differences in volatility might affect leaching behaviour is not understood.

There now exists significant data on the short-term release of radionuclides from moderate and high burn-up BWR and PWR fuel. The EU First-Nuclides project (Lemmens et al. 2017) has resulted in new data becoming available on the IRF of ^{129}I and ^{137}Cs. Much of this new data comes from experiments performed on high burn-up fuel and almost all the data discussed below comes from fuel with burn-up values from 50 – 65 GWd/t$_{iHM}$, which encompasses the typical burn-up values of Swiss power reactor fuel. Earlier studies of the IRF of low to moderate burn-up fuels

were summarized in Johnson & McGinnes (2002). It is further noted that almost all the experimental data obtained below as well as the data discussed in Johnson & McGinnes were obtained by leaching fuel samples in water under oxidizing conditions. Such experiments are performed over a period of weeks to months, which is too short a period for estimating IRF values for long-term safety assessment. Grain-boundary release could continue on the time scale of many years: thus experiments may not succeed in determining the end of prompt release contributions.

A radionuclide release model for safety assessment using IRF values and corrosion-based release (or matrix dissolution) rates includes the implicit assumption that the latter mechanism involves congruency of release, i.e., after the short-term release, the remaining radionuclide inventory is released at the same fractional rate as the uranium oxide matrix dissolves. The evidence for congruency of release comes from a number of experiments performed under strongly reducing conditions simulating geological disposal, where matrix dissolution becomes extremely slow. These experiments show that release of the radionuclides with a low IRF (i.e. FGR < 5%) appears to cease after a short period of time (see e.g. Spahiu et al. 2000, 2004 and Puranen et al. 2018, 2020 and 2022). This is illustrated in Fig. 4-2, taken from Puranen et al. (2018). The amounts released are reported as FIAP (Fraction of the Inventory in the Aqueous Phase), which for highly soluble radionuclides has the same meaning as cumulative fractional release.

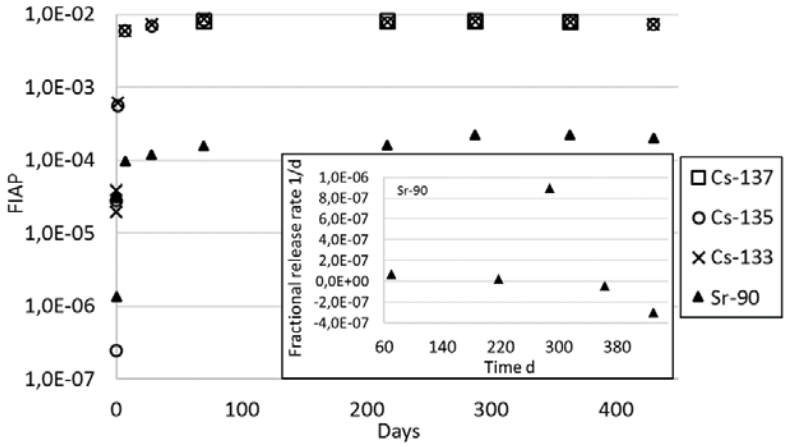

Fig. 4-2: FIAP (Fraction of the Inventory in the Aqueous Phase) values for Cs isotopes and Sr-90 under 5 MPa H_2 pressure in 10 mM NaCl and 2 mM $NaHCO_3$ solution

The fuel sample had a burn-up of 65 GWd/t_{iHM} and a FGR of 2.45%. From Puranen et al. (2018), reprinted with permission from the publisher

Results for the IRF of ^{129}I for high burn-up BWR and PWR fuels studied in the FIRST-Nuclides project (Lemmens et al. 2017) are shown in Fig. 4-3 and Fig. 4-4. The diffusion coefficients of Xe and I in UO_2 are approximately the same (Lewis et al.1990), thus a 1:1 relationship is expected. The data show that the IRF is approximately the same as the FGR, although there is significant scatter around the 1:1 line. The degree of scatter is similar to that shown in Fig. 2-13 for calculated vs. measured FGR.

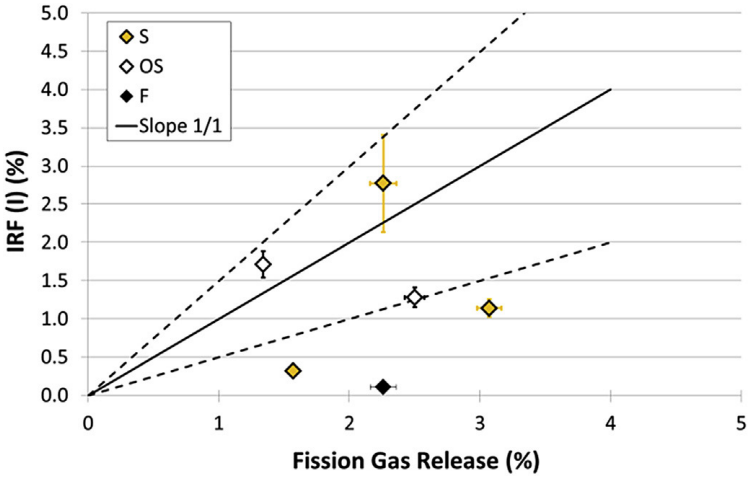

Fig. 4-3: Maximum cumulative IRF of iodine (%) as a function of Fission Gas Release (%) for BWR fuel samples, with 95% confidence intervals

When not visible, the error bars are hidden by the symbols; the dotted lines indicate IRF deviations of ± 50% from the ideal slope 1/1, shown as a solid line; Legend: S = clad fuel Segment, OS = Open Segment, F = Fragment (Lemmens et al. 2017). The terms closed and open refer to clad samples and samples with the cladding pried open to release the fragments.

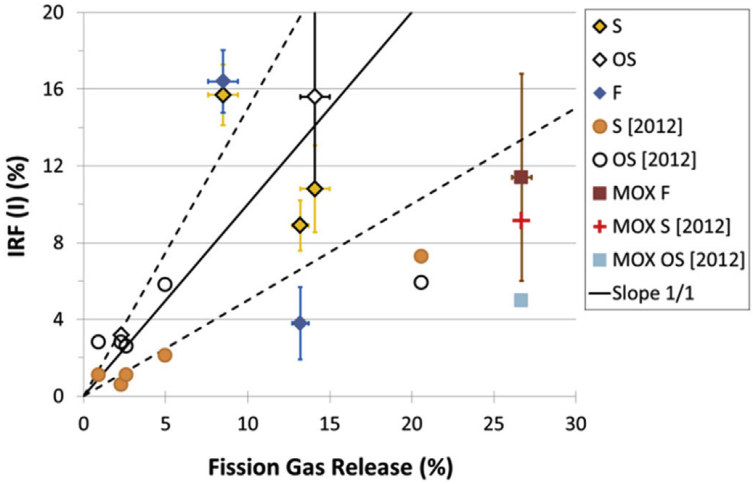

Fig. 4-4: Maximum cumulative IRF of iodine (%) as a function of Fission Gas Release (%) for PWR samples, with 95% confidence intervals

The dotted lines indicate IRF deviations of ± 50% from the ideal slope 1/1, shown as a solid line; the data indicated as [2012] were taken from Johnson et al. (2012) and Ekeroth (2012); the 95% confidence intervals are shown only for the data from FIRST-Nuclides; Legend: S = clad fuel Segment, OS = Open Segment, F = Fragment. (Lemmens et al. 2017). The terms closed and open refer to clad samples and samples with the cladding pried open to release the fragments.

Results for ^{137}Cs are shown in Fig. 4-5 and Fig. 4-6. Based on the diffusion coefficients in UO_2, a $\sqrt{(1/3)} \approx 0.6$ relationship between FGR and Cs IRF is expected (Lassman et al. 2002, Johnson et al. 2012). Most of the data in Fig. 4-5 follow the expected behaviour within the confidence intervals. For the data below the correlation, the fission gas release overpredicts the IRF for Cs and is therefore conservative for safety assessment calculations.

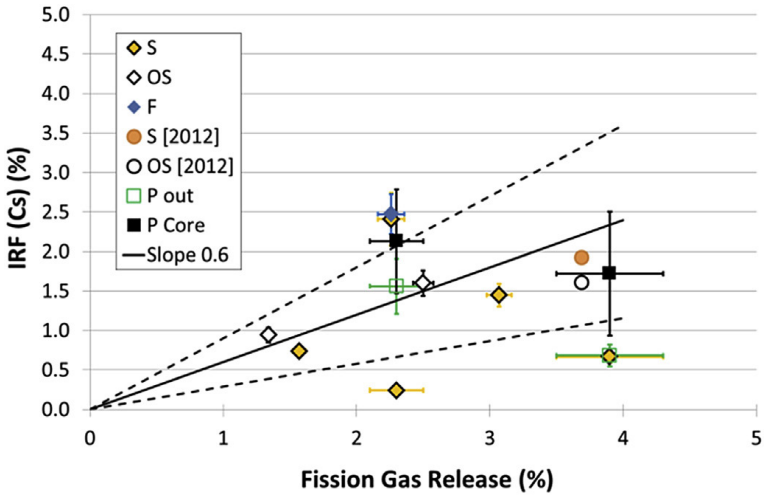

Fig. 4-5: Maximum cumulative IRF of cesium (%) as a function of Fission Gas Release (%) for BWR fuel samples, with 95% confidence intervals

When not visible, the error bars are hidden by the symbols; the dotted lines indicate IRF deviations of ± 50% from the ideal slope 0.6, shown as a solid line; the data indicated as [2012] were taken from Johnson et al. (2012) and Ekeroth et al. (2012); Legend: S = clad fuel Segment, OS = Open Segment, F = Fragment, P = Powder from the core or outer zone of the pellets. Lemmens et al. (2017). The terms closed and open refer to clad samples and samples with the cladding pried open to release the fragments.

As seen in Fig. 2-8, the principal driver of FGR is fuel temperature, which is reflected in the LHR of the fuel. A similar correlation also applies to the measured release fractions for ^{129}I and ^{137}Cs, as seen in Fig. 4-7 and Fig. 4-8, which plot the data in Figs. 4-2 to 4-6 against the LHR at roughly 50% of the EOL burn-up. As for FGR (Fig. 2-8), a threshold LHR of about 200 – 250 W/cm is necessary to generate high IRFs for iodine and cesium.

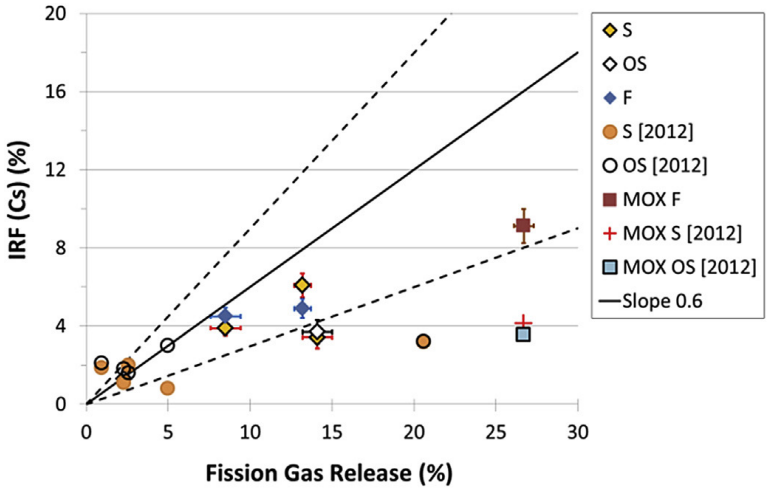

Fig. 4-6: Maximum cumulative IRF of cesium (%) as a function of Fission Gas Release for PWR samples, with 95% confidence intervals

The dotted lines indicate IRF deviations of ± 50% from the ideal slope 0.6, shown as a solid line; the data indicated as [2012] were taken from Johnson et al. (2012) and Ekeroth et al. (2012); the 95% confidence intervals are shown only for the data from FIRST-Nuclides; Legend: S = clad fuel segment, OS = Open Segment, F = Fragment. (Lemmens et al (2017). The terms closed and open refer to clad samples and samples with the cladding pried open to release the fragments.

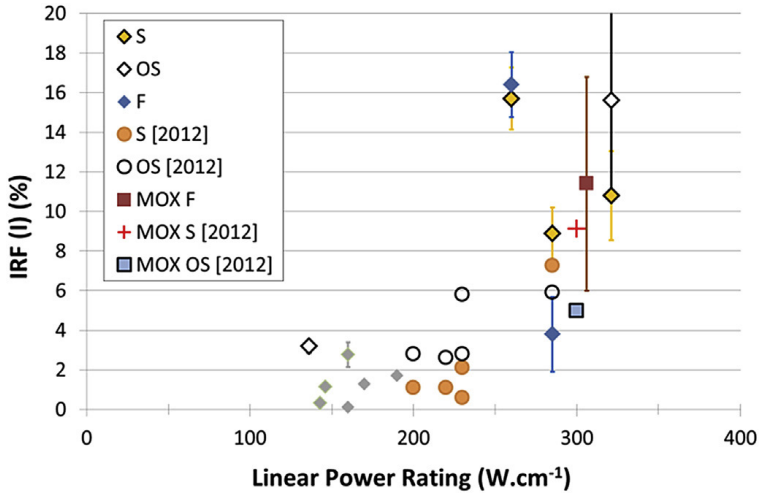

Fig. 4-7: IRF values of ^{129}I for BWR and PWR UO_2 fuel and MOX power reactor fuel

Taken from Fig. 32 of Lemmens et al. (2017); for details on sample identification and comments on LPR see Lemmens et al. (2017).

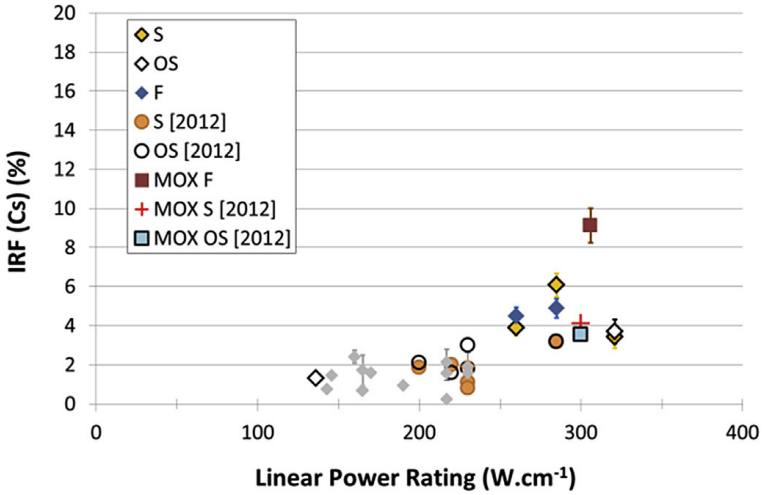

Fig. 4-8: IRF values of Cs for BWR and PWR UO_2 fuel and MOX power reactor fuel

Taken from Fig. 33 of Lemmens et al. (2017); for details on sample identification and comments on LPR see Lemmens et al. (2017).

Recently, so called doped UO_2 fuels, doped with minor amounts of Cr_2O_3, Al_2O_3 or other oxides, are being used in LWRs. The main effect of the dopants is to increase density and grain size (up to about 60 µm) during the sintering process (Arborelius et al. 2006). At normal reactor operation temperatures, this reduces diffusion of fission gas and the segregation of volatile/semivolatile nuclides out of the grains, minimizing the risk of cladding failures through stress corrosion cracking (Piro et al. 2017). As a collateral result, the coarsening and densification allow doped fuels to be operated at higher power, increasing energy harvesting efficiency.

In spite of the small concentrations involved, the addition of Cr and Al oxides modifies the initial chemistry and grain structure of the fuel. It is therefore not clear a priori what the net effect of doping will be on IRF and fuel dissolution rates under repository conditions. Only comparative experiments with doped and non-doped spent fuel having similar in-pile histories and carried out under the same repository-relevant laboratory conditions can provide a reliable answer. This topic is quite recent and object of ongoing research.

In a series of spent fuel leaching studies under oxidizing conditions (Roth et al. 2013, Roth et al. 2014, Nilsson et al. 2017) the leaching behaviour of ADOPT fuel was compared to standard UO_2 fuel. The doped fuel was produced by Westinghouse using the so-called "ADOPT[4]" technology (Arborelius et al. 2006). These studies showed that the Cr-doping had little to no effect on fuel dissolution behaviour. Nevertheless, a lower release of Cs and I was observed for the doped samples, while the releases of Mo and Tc were relatively higher. The slightly higher releases from a Cr-doped PWR fuel (not ADOPT) as compared to standard UO_2 and ADOPT fuel were due to the smaller grain size of the leached sample (Barreiro-Fidalgo et al. 2021).

In the context of the recently finalized DisCo project, comparative dissolution studies were carried out. Radionuclide release data were obtained under identical conditions for conventional UO_2 fuel and a Cr, Al-doped UO_2 fuel (Fidalgo et al. 2020, Metz 2021, Evins et al. 2021) irradiated in a BWR reactor. The objective of the study was to test whether the radionuclide release and dissolution behavior of the two types of fuels would differ significantly under anoxic repository conditions, i.e. if introducing the dopants would lead to different IRF and matrix dissolution rates. To this end, fragments of both types of spent fuel, both irradiated in BWR reactor to similar local

[4] ADOPT = Advanced Doped Pellet Technology

burn-ups (BU = 63 and 66 MWd/t_{iHM}, FGR = 2.5 and 1.4%, for the standard and doped fuel, respectively) were leached in NaCl-$NaHCO_3$ solution in H_2 atmosphere for 1'001 days. The solution used represents a simplified repository pore water of near-neutral pH.

A number of radionuclides were monitored (^{238}U, ^{239}Pu, ^{237}Np, ^{135}Cs, ^{100}Mo, ^{90}Sr, ^{99}Tc, ^{129}I). Fig. 4-9 shows selected results, revealing very similar release patterns for ^{238}U, ^{90}Sr, ^{135}Cs and ^{129}I for the two fuels. The evolution curves of all four isotopes are almost identical and it can thus be concluded that the dissolution behaviour of the two fuels is practically identical under the selected experimental conditions. The ^{238}U concentration stabilized at values of $2 – 5 \times 10^{-8}$ mol/L, which is about one order of magnitude higher than expected at equilibrium with UO_2(am) under strictly anoxic conditions. This is due to the fact that the fuel samples used in these tests had been leached for several years under oxidizing conditions and were extensively pre-oxidized, resulting in precipitation of UO_2(s) in bulk solution under H_2 leaching. The concentrations of the highly soluble IRF nuclides ^{135}Cs and ^{129}I stabilized after about 200 days, while the ^{90}Sr concentration continued to increase slightly up to at least 700 days, which is taken as indication of matrix dissolution. The earlier stabilization of ^{135}Cs and ^{129}I indicates that the release of these nuclides is related to prompt dissolution from the readily accessible gap region or open fractures, not to matrix dissolution. Note that a comparison of radionuclide releases based on aqueous concentrations rather than on inventory normalized releases (FIAP) is allowed in this case because of the similar nature of the samples (fragments with presumably similar total exposed surface area), irradiation history (similar local burnups) and identical experimental conditions.

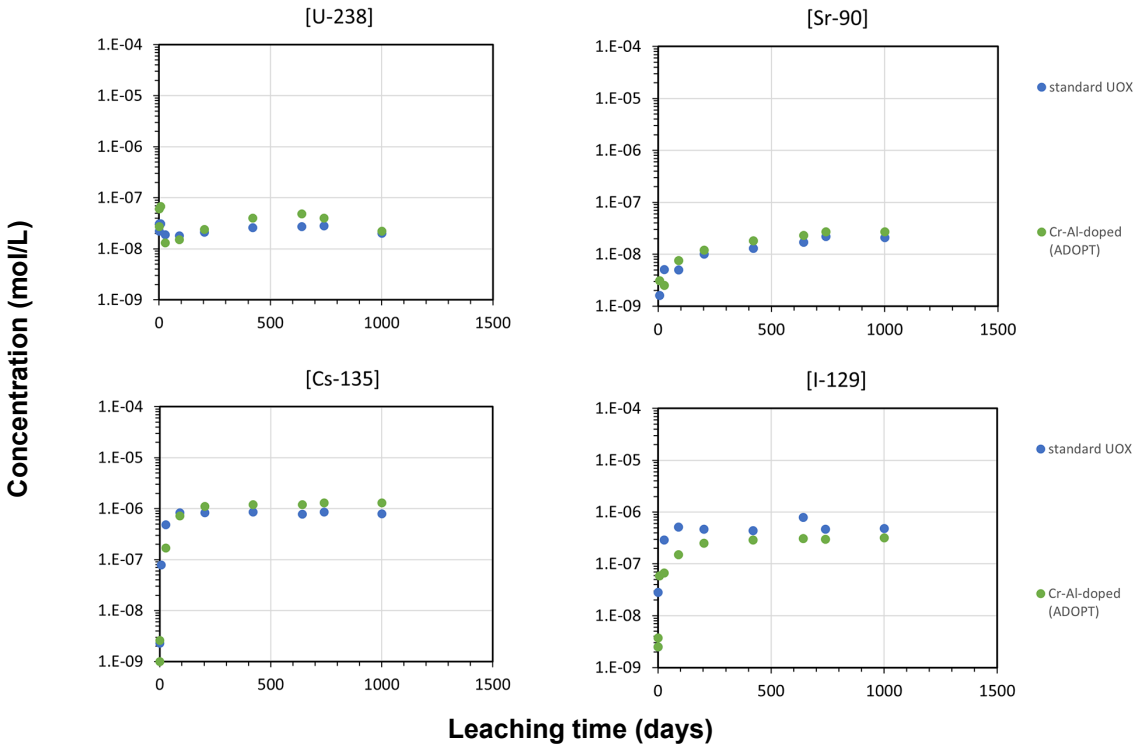

Fig. 4-9: Selected results from leach experiments with standard and Cr,Al-doped fuel, carried out under H_2 atmosphere

Data retrieved from Appendix in Metz (2021).

4.2 Potential release of the inventory at grain boundaries

As noted in Chapter 2, the IRF is defined as

$$IRF = IRF_G + IRF_{GB}$$

where IRF_G represents the fraction of the total radionuclide inventory in the fuel that is released from the gap (the interconnected void space in the fuel rod) and IRF_{GB} is the fraction of the total radionuclide inventory in the fuel released from grain boundaries. As discussed in Section 2.2.3, significant accumulations of FG and potentially other volatile radionuclides can occur at grain boundaries in spent fuel. In performance assessment calculations in Nagra (2002), the quantities of fission products that have accumulated in closed pores at grain boundaries have been pessimistically considered to be included in the IRF (Johnson & McGinnes 2002).

For the rim region, in which there is significant FG trapped in pores, there appears to be no enhanced release of ^{137}Cs (Fors et al. 2009, Johnson et al. 2012, Roudil et al. 2007). This is consistent with the EPMA measurements of Walker et al. (1996), who found no evidence for Cs associated with FG bubbles in the rim. This indicates that the approach of considering the rim region as part of the IRF, as suggested by Johnson et al. (2005) and Johnson (2014) is overly pessimistic. This conservatism is not included in the spent fuel dissolution model for SR-Site (SKB 2010a, b), in which only the gap inventory was considered in estimating the IRF for the various reactors. The discussion in Section 3.27 of SKB (2010b) stated that, while there is some conceptual uncertainty in deriving the IRF, there is a reasonable basis for arguing that the grain boundary inventories do not contribute to the IRF at burnups < 45 MWd/kg_{iHM} , at least for low to moderate FGR fuels. Conceptually, the argument made is that, while there are certainly FG bubbles present at grain boundaries throughout the fuel (see Tab. 2-3) they represent closed pores. Therefore, such FG with the associated ^{135}Cs and ^{129}I will be released at the same rate as matrix dissolution and consequently the IRF_{GB} term is considered to be negligible. If this assumption is incorrect, i.e. if Cs and I continue to be released from grain boundaries even though the matrix dissolution rate has become negligible because of reducing conditions, the grain boundary inventory in Tab. 2-3 should be included in the IRF.

Several studies that have a bearing on this issue are discussed below and the key results are summarized in Tab. 4-1. The studies considered have all been performed under reducing conditions using pressure vessels that permit measurement (in some cases) of the fission gas released during dissolution of the fuel. This contrasts with the data from the First-Nuclides Project (Fig. 4.1 and Figs. 4-3 to 4-8), which were obtained in experiments to determine the IRF under oxidizing conditions where matrix dissolution is far more rapid. Experiments performed in pressure vessels under reducing conditions are of particular interest, given the paucity of measurements of ^{129}I release, as studies have shown that ^{129}I and Xe have approximately the same in-reactor diffusion coefficient in UO_2. As a result, Xe releases under reducing conditions may allow an upper bound to be placed on ^{129}I releases from grain boundaries.

Fors et al. (2009) performed experiments under reducing conditions on a fuel rod section with a burnup of 59 MWd/kg_{iHM} containing a large part of the rim material. The fuel would be expected to have had a significant GB inventory in the rim pores according to Tab. 2-3. Despite this, the data suggest essentially negligible Cs release after the first 7 days of the 502-day experiment, which offers evidence that grain boundaries in the rim do not contribute to release under reducing conditions. A study by Ekeroth et al. (2020) showed constant ^{137}Cs concentrations after about 200 days and no indication of further release for up to 700 days for a fuel sample with a burnup of 43 MWd/kg_{iHM}. Xenon and ^{129}I release were not measured. Röllin et al. (2001) studied Cs and U release in flow-through dissolution experiments and observed the same fractional release rates, confirming no preferential release from grain boundaries. Again, ^{129}I release was not measured.

The evidence that there is negligible Cs release from grain boundaries under reducing conditions is good for moderate burnup, low FGR fuel and for the high burnup structure of the rim, but there is no data available for ^{129}I or Xe release. The situation for high burnup and high FGR UO_2 fuel and for MOX fuel is discussed below.

Puranen et al. (2018) observed accumulation of 1 to 1.5% of the Xe inventory in the gas phase of their pressure vessel over 420 days for a fuel sample from a rod that had a puncture test FGR of 2.45% and a burn-up of 65 MWd/kg_{iHM} (see Fig. 4-2), suggesting some opening of fission gas bubbles during the experiment. Despite this, they observed no further increase in Cs concentration after 70 days. No measurements of ^{129}I were performed in the experiment. In a recent study by Puranen et al. (2022) a fission gas release of 28% was measured as well as an ^{129}I release of 8.95% on a fuel sample with a puncture test FGR of 5% and a burn-up of 75 MWd/kg_{iHM}. The trend towards high release of Xe from grain boundaries as burnup increases is expected, as grain boundaries become more and more densely populated with gas bubbles and their interlinkage increases (Rest et al. 2019). It is noted that both the fuels studied by Puranen et al. (2018, 2022) had burnup values exceeding those found in the Swiss inventory of fuels for disposal.

Tab. 4-1: Evidence related to the degree of preferential leaching of Xe, ^{129}I and Cs from spent fuel samples under reducing conditions

Fuel data	**Leaching conditions**	**Release into solution**	**Comments regarding release from GB**	**Reference**
BU – 59.1 MWd/kg_{iHM} High BU rim sample FGR – not reported	H_2 Pressure – 4.1 MPa T – 20 °C Duration – 502 days	^{137}Cs – 3.5% released; 97% of this release occurred in the first 7 days	Negligible Cs release from GB. Very small amount of FG detected	Fors et al. (2009)
BU – 43 MWd/kg_{iHM} FGR (puncture) - 0.3%	H_2 Pressure – 0.5 MPa T – 20 °C Duration – 760 days	^{137}Cs – 0.7% - constant after 100 days	No evidence of Cs release after 100 days	Ekeroth et al. (2020)
BU – 43 MWd/kg_{iHM} FGR (puncture) - 0.3%	H_2 Pressure – 0.01 MPa T – 20 °C Flow-through experiment	Approx. same FRR of U and ^{137}Cs	No evidence of preferential release of FPs under reducing conditions	Röllin et al. (2001)
BU – 65 MWd/kg_{iHM} LPR – typical FGR (puncture) 2.7% Cs pre-leach 1.3%%	H_2 Pressure – 5 MPa T – 20 °C Duration – 440 days	FG – 1 to 1.5% (end of test) ^{135}Cs – 0.9% (stable conc. after 300 days)	Evidence of slight FG release despite little matrix dissolution	Puranen et al. (2018)
BU – 75 MWd/kg_{iHM} LPR - typical FGR (puncture) – 5% Cs pre-leach 0.96%	H_2 Pressure - 2.5 to 4 MPa T – 20 °C Duration – 459 days	FG – 28% (still slightly increasing) ^{129}I – 8.95% ^{135}Cs – 1.94% (stable conc. after 300 days)	Evidence of significant FG and ^{129}I release from FG bubbles despite little matrix dissolution	Puranen et al. (2022)
BU – 50 MWd/kg_{iHM} Gösgen High LPR NIKUSI fuel* FGR (puncture) – 8.3%	H_2 Pressure – 0.32 MPa T – 20 °C Duration – 450 days	FG – 15% (clad segment) to 23% (fragments). Release from fragments reached steady state of 23% after 4 months.	Evidence of major FG release	Gonzalez-Robles et al. (2016)
BU – 50 MWd/kg_{iHM} Gösgen High LPR NIKUSI fuel* FGR (puncture) – 8.3%	H_2 Pressure – 0.3 MPa T – 20 °C Duration – 333 days	FG – 16% ^{129}I – 16% ^{137}Cs – 3.9%	Evidence of major FG and ^{129}I release	Gonzalez-Robles et al. (2015)

Tab. 4-1: Cont.

Fuel data	Leaching conditions	Release into solution	Comments regarding release from GB	Reference
BU – 43 MWd/kg_{iHM} FGR (puncture) - 0.3%	H_2 Pressure – 0.5 MPa T – 20 °C Duration – 500 days	^{129}I – 25%[5] ^{137}Cs – 0.2%	Release of Cs stopped after intial release. See footnote below regarding unreliability of the ^{129}I analysis.	Spahiu et al. 2004
MOX fuel BU - 47 MWd/kg_{iHM} FGR – not reported	H_2 Pressure – 5.3 MPa T – 23 °C Duration – 2078 days	^{137}Cs concentrations release increased slowly; no further release after 800 days	Cs released from grain boundaries, but the release stopped.	Carbol et al. 2009 JNM

* NIKUSI – Niedrigtemperatur-Kurzzeit-Sintern (low-temperature short-time sintering) – experimental fuel rods irradiated at Gösgen. These are not standard production fuel rods.

In low FGR fuel (below several%) the fission gas bubbles accumulated at grain boundaries are poorly connected to one another, thus on exposure to water leaching of Cs and I from these closed bubbles would not occur if matrix dissolution were suppressed by reducing conditions. Once a much more interconnected network develops along grain boundaries, as with high FGR fuel, water can percolate more effectively throughout the fuel reaching fission gas bubbles that are also likely to be associated with Cs and ^{129}I. Gonzalez-Robles et al. (2015, 2016) studied a high FGR (8.3%) Gösgen fuel with a burn-up of 50 GWd/tU. Gösgen fuel assemblies have high puncture test FGR compared to other LWR fuel assemblies (see Fig. 2-11). They observed significant continuing Xe and ^{129}I release in a sealed vessel with a H_2 overpressure. The cumulative release of Xe and ^{129}I in the experiment plateaued at about 16% of the inventory in the fuel after about 300 days of leaching. The experimental conditions would be expected to suppress matrix dissolution, thus causing a rapid levelling off of ^{129}I concentration and very little accumulation of Xe in the gas phase of the sealed autoclave. It is possible that this finding is related to the observations of Walker et al. (1996), which include a sample of Gösgen fuel, where it was suggested that Cs from the centre of the fuel condensed within FG bubbles in the cooler mid-radial region. However, the fuel rod studied by Gonzalez-Robles et al. (2015, 2016) was fabricated using low temperature sintering, a process unlike that used in normal UO_2 pellet fabrication, which may have contributed to its unusual dissolution behaviour. Moreover, it was a test rod that has not been used commercially in Gösgen (as confirmed to Nagra by Gösgen by written communication (internal document)). The significance of these findings is thus so far not clear.

The Spahiu et al. (2004) study of a low FGR fuel observed no continuing Cs release over 500 days after the initial release of 0.2% that occurred in the first few days.

Comparable data for MOX fuel is scarce. Carbol et al. (2009a) studied the dissolution of a MOX fuel sample with a burnup of 47 MWdkg_{iHM} over a period of 2078 days and observed no Cs release after 800 days. Again, ^{129}I and Xe release were not measured.

The data discussed above suggest that there is little preferential (grain boundary) release of Cs isotopes under reducing conditions for a burnup of about 45 MWd/kg_{iHM}. For the case of 65 MWd/kg_{iHM}, both the Cs release and the Xe release during leaching were less than the puncture test FGR. The database for estimating the contribution under reducing conditions of preferential

[5] According to K. Spahiu, the ICP-MS data used to calculate iodine concentrations in this work were obtained using the acidified solution sample in which all isotopes are analysed and are thus highly unreliable.

^{129}I leaching to the IRF is clearly poor, particularly in the case of ^{129}I. The results observed by Gonzales-Robles et al. (2015, 2016) for Gösgen experimental fuel assemblies having high FGR are suggestive that high LPR fuel as that from Gösgen may have a tendency to progressive leaching, but it is not clear whether the data are representative and could be used quantitatively because the fuel was produced by a non-standard method. Nonetheless, they were irradiated at the typical high LPR of Gösgen reactor fuel, so they are at least indicative.

It can be concluded, based on the discussion above, that there is likely to be no continuing preferential leaching of Cs for the typical burnup values of fuels from Beznau (avg. 44 – 47 MWd/kg$_{iHM}$), Mühleberg (avg. 47 MWd/kg$_{iHM}$) and Leibstadt (avg. 46 MWd/kg$_{iHM}$) fuels. However significant preferential leaching from Gösgen fuel (avg. 55 MWd/kg$_{iHM}$) cannot be ruled out and should be considered. Based on these observations, the FGR calculations in Section 2.3 and the FGR-IRF correlations in Section 4.1, the following section presents aggregated IRF estimates.

4.3 Overall assessment of uncertainties of IRF estimates for Cs and I

The largest uncertainty in IRF estimates of Cs and I may be the degree to which Cs and I leaching continues to occur despite the very low matrix dissolution rate under reducing conditions. Experimental results with spent fuel such as shown in Fig. 4-2 and in other studies discussed in Section 5 are performed for hundreds of days. On this time frame release rates of Cs and I become exceptionally low. It is not certain however, that preferential release stops altogether, and that release occurs only as a result of matrix dissolution. Because of this uncertainty, both average and upper bound IRF values exceeding the modelled FGR values are proposed.

4.4 IRF of ^{36}Cl and ^{14}C

Measurements of the release of ^{36}Cl from spent fuel have been reported by Tait et al. (1997) for CANDU fuel and this is the only available data. The analysis method used was accelerator mass spectrometry, which is demanding and costly. This study reported that, for high linear power rating fuel, the releases considerably exceeded FGR. Because the power ratings of CANDU fuel far exceed those in LWR fuel (see Section 2.2.2), the observed high fractional releases may not apply to LWR fuel. Nonetheless, the absence of any data on ^{36}Cl release from PWR fuel suggests it is prudent to assume ^{36}Cl releases are 2 to 3 times that of FGR (see SKB 2010b).

The largest number of measurements of ^{14}C release come from the study of CANDU fuel samples by Stroes-Gascoyne et al. (1994). They reported a mean release of (2.7%) for a large number of fuel samples. There are a few measurements of ^{14}C release for LWR fuel that are in the range of about 1 – 3.5%. The results on CANDU fuel have shown that ^{14}C release is independent of linear power rating, thus the CANDU fuel data are directly relevant. Reports by Wilson and Shaw (1987) and Wilson (1990a, 1990b) refer to rapid releases of 0.05 to 3.5% of the ^{14}C inventory in their LWR fuel leaching tests. Mennecart et al. (2014) observed releases of ^{14}C of 1.5% from high burn-up LWR fuel after 357 days.

Given the scarcity of data on ^{14}C release from LWR fuel, it seems appropriate to give greatest weight to the data set of Stroes-Gascoyne et al. (1994). As a result, an average IRF of 3% is assumed for ^{14}C, with an upper bound of 5%.

4.5 IRF of ^{79}Se

The possibility of a large IRF of ^{79}Se was postulated in some previous studies (e.g. Johnson & McGinnes 2002 and Johnson et al. 2005), because little was known about its behaviour in fuel rods and there was a need to ensure that the release fraction in safety assessments was not underestimated. Curti et al. (2014) showed using spectroscopic techniques that selenium appears to be present in spent fuel as Se^{-2} and is substituted for oxygen in the UO_2 lattice, from which it might be inferred that there would be a negligible IRF.

Attempts have been made to measure the aqueous release of ^{79}Se from LWR fuel under oxidizing conditions. Wilson (1987) was not successful in detecting Se in leaching and from his "less than" values a maximum release of < 0.025% can be derived. Johnson et al. (2012) also attempted to measure ^{79}Se release but were not successful, reporting a "less than" value of 0.22% derived from the detection limit in the experiments. Puranen et al (2014) measured an IRF for ^{79}Se under reducing conditions of 0.29% using a ICP-MS technique with improved detection limit but suggested that Se is heterogeneously distributed in the fuel because its release rate is intermediate between that of Cs and U. Kienzler et al. (2017) reported an IRF for ^{79}Se of 0.5 and 0.7% under oxidizing conditions after 178 days.

From these data, it is possible to conclude that the IRF of ^{79}Se is about 0.5%, with an upper bound of 1%.

4.6 IRF values of other long-lived fission products

As noted in Tab. 2-2, the fission products ^{99}Tc, ^{107}Pd and ^{93}Mo are present largely in noble alloy ε-particles, which are easily visible in micrographs of spent fuel (Fig. 2-5). The degree of segregation from the UO_2 grains may be significant, but the alloy particles are resistant to chemical dissolution. Indeed, low IRF values for ^{99}Tc have been reported by Cui et al. (2011) (0.03%), (Spahiu 2004) (0.01%) and Kienzler (2017) (0.001%).

Prior estimates of large IRF values for Tc and Pd in Johnson & McGinnes (2002) were principally based on the very pessimistic assumptions that the fraction of these fission products in the rim region was up to 16%, without consideration for their potential dissolution. These inclusions are essentially noble metal alloys, thus little if any dissolution is expected to occur (Cui et al. 2001). In the SR-Site safety assessment SKB (2010b) assumed that the maximum IRF for ^{99}Tc and ^{107}Pd is 1%, which is quite conservative given the values for ^{99}Tc noted above. A more realistic estimate would be 0.01%, with an upper bound of 0.1%.

As discussed in SKB (2010), tin is expected to be metallic in fuel (Kleykamp 1985) and non-volatile under fuel in-reactor conditions. The IRF values for Sn-125 proposed by Johnson & McGinnes (2002) are therefore excessively pessimistic and the IRF value of 0.1% is adopted, as proposed in SKB (2010b).

Very limited preferential release of Sr-90 is seen in leaching experiments. Johnson and Tait (1997) concluded that the best estimate IRF for Sr would be 0.25%, with 1% as a pessimistic estimate. At that time, all data available were from experiments performed under oxidizing conditions. As shown in Fig. 4-2 (Puranen et al. 2018), the IRF of Sr-90 is about 0.02% under reducing conditions. Ekeroth et al. (2020) reported an IRF of 0.05% under reducing conditions. A more recent study by Puranen et al. (2022) reported an IRF of 0.05%. As greater weight should be given to the results measured under reducing conditions, an average IRF of 0.05% is assumed, with an upper bound of 0.25%.

4.7 IRF of C-14 from Zircaloy

A dedicated report related to ^{14}C has been authored by Nagra (2023b). Instant release fraction (IRF) for ^{14}C from Zircaloy defined in there are 0.01% (reference), 0.1% (upper bound) and 0.001% (lower bound). Activities of the inventory are part of the MIRAM-RBG Database (Nagra 2023a)

The content of Cl in Zirconium alloys is expected to be very low. For example, Aitchson & Davies (1993) measured Cl impurity levels of 1 to 5 ppm in Zr/2.5Nb pressure tubes. Zwicky (2008) documented maximum allowed Cl concentrations for Zircaloy-2 of 20 ppm for a rod irradiated in Forsmark 3. No measurements have been reported of ^{36}Cl release from Zircaloy.

4.8 Summary of recommended IRF values for radionuclides for fuel from Swiss power reactors

The proposed IRF values of radionuclides for the Swiss reactors are summarised in Tab. 4-2, based on the data presented earlier. As discussed in Sections 4.1, a $\sqrt{(1/3)}$ relationship between FGR and the IRF of Cs (135 and 137) is adopted, whereas ^{129}I IRF values are assumed to be the same as FGR. For ^{36}Cl, an IRF value three times that of FGR is assumed. All other IRF values are not correlated with FGR.

Upper bound values are also presented. Based on the discussion in Section 4.1, the upper bound IRF values for both Cs isotopes and ^{129}I are assumed to be twice the reference Cs IRF value.

There are some significant changes in Tab. 4-2 compared to the analogous Tab. 5 in Johnson (2014). The following changes are noted:

1. Tab. 4-2 gives lower MOX FGR values for Beznau (2%) than the previously estimated 4%, based on the lower average burnup of MOX fuel adopted in the present study. The average MOX FGR for Gösgen has been increased to 16%.
2. Upper bound IRF values are given in Tab. 4-2 rather than distinguishing between gap and grain boundary inventories as was done in the previous study. This acknowledges the difficulty of quantitatively estimating grain boundary inventories and the need to consider the, at present, contradictory evidence for continuing preferential release of fission gas (and by inference I and perhaps Cs) under reducing conditions. Given the uncertainties, it is considered more transparent to simply define pessimistic upper bound IRF values.
3. The IRF values for noble metal fission products are greatly reduced in Tab. 4-2 because of new data from experiments performed under reducing conditions.

Tab. 4-2: Average FGR and reference and upper bound IRF (aqueous release) values (%) of radionuclides for spent fuel from the Swiss reactors

Red shading represents IRF values that are correlated with FGR (see Section 4). Blue shading indicates IRF values not correlated with FGR.

	Beznau		**Gösgen**		**Leibstadt**	**Mühleberg**
	UO_2	**MOX**	**UO_2**	**MOX**	**UO_2**	**UO_2**
FGR (avg.)	1.8	2	14	16	4	3
Cs IRF (ref.)	1.1	1.2	8	9	2.3	1.7
Cs IRF (upper bound)	2.2	2.4	16	18	4.6	3.4
^{129}I (ref.)	1.8	2	14	16	4	3
^{129}I (upper bound)	3.6	4	28	32	8	6
^{36}Cl	5.4	6	42	48	12	9
^{79}Se (ref.)	0.5	0.5	0.5	0.5	0.5	0.5
^{79}Se (upper bound)	1	1	1	1	1	1
^{14}C (ref.)	3	3	3	3	3	3
^{14}C (upper bound)	5	5	5	5	5	5
^{126}Sn	0.1	0.1	0.1	0.1	0.1	0.1
^{90}Sr (ref.)	0.05	0.05	0.05	0.05	0.05	0.05
^{90}Sr (upper bound)	0.25	0.25	0.25	0.25	0.25	0.25
^{107}Pd (ref.)	0.01	0.01	0.01	0.01	0.01	0.01
^{107}Pd (upper bound)	0.1	0.1	0.1	0.1	0.1	0.1
^{99}Tc (ref.)	0.01	0.01	0.01	0.01	0.01	0.01
^{99}Tc upper bound)	0.1	0.1	0.1	0.1	0.1	0.1

5 Fuel matrix dissolution

5.1 Chemistry of UO_2 dissolution

Spent fuel is largely UO_2(s), with only a small fraction of other actinides and fission products. The majority of these radionuclides are present as interstitials or in solid solution in the UO_2(s) matrix (Kleykamp 1985). The release of the IRF radionuclide fraction was described in the previous sections: here the dissolution rate of the fuel matrix itself is discussed. The rate of spent fuel dissolution depends on a variety of factors such as the composition of the spent fuel itself and of the groundwater, as well as the redox conditions under which the dissolution takes place.

The main component of the fuel matrix, uranium dioxide UO_2(s), dissolves in water by releasing U(IV) species in solution. This process occurs with a certain rate, referred to as the rate of *non-oxidative dissolution*. There is also an *oxidative dissolution (corrosion)* of UO_2(s), during which various oxidants present in solution cause the oxidation of U(IV) atoms on the surface, followed by their release in solution as U(VI) or uranyl (UO_2^{2+}) species (see next section). The non-oxidative dissolution thus occurs only in the complete absence of oxidants with the dissolution rate higher when far from saturation but approaching zero when the concentration of U(IV) in solution approaches the solubility limit of UO_2(s) under the given conditions. In the pH range expected in a deep repository, UO_2(s) is sparingly soluble and U(IV) solutions in equilibrium with UO_2(s) have a concentration of ~ 3 10^{-9} M (Guillamont et al. 2003, Grenthe et al. 2020). This low solubility of UO_2(s) under repository conditions, together with the absence of advective fluxes expected in the repository near field, make the non-oxidative dissolution unimportant for the releases from the canister. This is because in the absence of oxidants, the solution inside the canister quickly becomes saturated and the non-oxidative dissolution rate approaches zero.

Within a few weeks to months after canister emplacement and backfilling, as observed in the FE (Full-scale Emplacement) experiment at Mont Terri, all oxygen present in the bentonite nearfield will be consumed (Giroud et al. 2018, Puigdomenech et al. 2002, Kolar & King et al. 1996) as summarised in Curti et al. (2023), resulting in an oxygen free and reducing environment. Under these conditions UO_2(s) would be stable and the release of actinides and the majority of fission products would be controlled by its low solubility.

5.2 Radiation chemistry and spent fuel dissolution

The reducing conditions in the failed canister can change as a result of water radiolysis, caused by the radioactivity of the spent nuclear fuel itself. Spent fuel emits alpha, beta, gamma and neutron radiation. Alpha radiation is the dominant contributor to radiolysis during spent fuel dissolution in the repository, as the fluxes of beta, gamma and neutron radiation decrease rapidly and become low after a few hundred years (see Fig. 3-2). The mechanisms and impact of water radiolysis on spent fuel dissolution have been investigated for decades (e.g., Shoesmith 2013 and references therein). In addition, significant strides have been made in improving the aqueous thermodynamic data for U, other actinides and important fission products (Grenthe et al. 2020, Olin et al. 2005, Rand et al. 2009). These studies have greatly aided in the interpretation of results from spent fuel dissolution studies.

The oxidants produced by radiolysis ($OH^{\cdot}$, $OOH^{\cdot}$, H_2O_2, O_2) oxidize U(IV) atoms in the fuel matrix surface to U(VI), which are then released in solution, especially if carbonate is present, due to the formation of strong U(VI)-carbonate complexes. The rate of this oxidative dissolution is much higher than that of non-oxidative dissolution (Röllin et al. 2001) discussed in Section 5.1. In addition, U(VI) hydrated oxides (e.g., schoepite) are several orders of magnitude more soluble than UO_2(s). The influence of various oxidants has been investigated in several studies and it was established quite early, based on electrochemical measurements, that H_2O_2 was ~ 200 times faster

than O_2 in oxidizing the UO_2 surface (Shoesmith et al. 1985, Shoesmith 2000). It was also established (Shoesmith 2000) that oxidation is the rate determining step, while the dissolution step, especially in the presence of carbonate, is relatively fast.

Fractional release rates (i.e., the fraction of the initial inventory released per year by congruent dissolution of all nuclides residing in the fuel matrix, units a^{-1}) for fission products such as Sr were used to estimate the fuel matrix dissolution rate. This is because U(VI) usually precipitated in a variety of U(VI) solid phases, depending on the solution composition after a few months leaching, and could not be used to estimate the rate of matrix dissolution. Other solids, such as calcite, could precipitate if synthetic groundwaters were used for leaching, blocking the surface from oxidative dissolution (Werme and Spahiu 1998). Based on the results of several studies in a variety of groundwaters typical for different repository concepts, including salt brines, the long-term Sr release rates were ~ $3.7\ 10^{-5}\ a^{-1}$ under oxidizing conditions, i.e., in presence of air (Loida et al. 2012).

In this section the influence of two intrinsic fuel parameters on the oxidative fuel dissolution rate is discussed, namely the surface area and the fuel burnup.

The microstructure of LWR spent fuel is complex with grain boundary surfaces typically exhibiting fission gas bubbles as well as ε-particles, particularly in the mid-radius to central region of the pellet where temperatures were highest (see Fig. 3-2). In addition, some fission gas tunnels exist in the central region of the fuel (Fig. 2-5) which will have permitted some of the fission gases (Xe, Kr) and other volatile fission products (e.g., Cs, I) to escape to fractures and thus to the outer regions of the fuel rod and the plenum. Spent fuel pellets are significantly fragmented due to thermally induced fracturing caused by the steep thermal gradient and the low tensile strength of the ceramic fuel material. This process is common to all fuel rods (Johnson and Shoesmith 1988). Similar fragment sizes and geometrical surface area were estimated for LWR and CANDU fuel rods based on particle size measurements (Johnson 1982) and fracture distributions measured in fuel pellet cross sections (Barner 1985 and Gray 1992). Nonetheless, these results do not provide a direct indication of the reactive surface area, which is expected to be significantly larger. This so-called specific surface area has typically been determined with BET measurements (Brunauer et al. 1938) which are widely used in mineral dissolution studies, partly because they permit a straightforward surface area normalization of dissolution rates measured in different studies. However, assessing the spent fuel area by BET is usually not successful for active fuel (Spahiu, 2021, Chapter 11). An extensive discussion of this issue and the estimated spent fuel surface area are given in Grambow et al. (2010). Moreover, under oxidizing conditions, although both BET and geometric surface areas were found to increase as dissolution proceeds, bulk release rates were found to decrease (Hanson and Stout 2004). Such contradictory results have eventually led to avoidance of using surface area as a means to normalize spent fuel dissolution rates. The current widespread practice is to report fractional dissolution rates of spent fuel fragments (Spahiu 2021, Section 11).

The outer part or the rim of the fuel pellet has higher actinide and fission product concentrations than the inside of the pellet, as well as smaller grains due to the *high burnup structure,* Fig. 2-7 (Rondinella & Wiss 2010). This means that the production of α, β, γ radiolytic products will be higher as compared to a grain on the inside of the pellet. Three systematic leaching studies of fuels with variable burnup (Ekeroth et al. 2009 and references therein, Jegou et al. 2004, Hanson 2008) have shown that the higher doping level at the pellet rim both with actinides (such as Pu) and fission products makes the fuel matrix less prone to oxidation and counteracts successfully both the higher surface area and the higher radiation field. The content of 2+, 3+ and 4+ non-uranium cations in spent fuel increases with burnup, leading to a decrease in dissolution rate by both a surface area effect (if the dopant is less soluble or dissolves more slowly than UO_2) and by a semi-conductor effect, which alters the ability for electron transfer, i.e., by limiting the stability of U in the +5 or +6 state. Oxygen potential calculations for Pu doped UO_2 (Catlow 1977,

Harding & Pandey 1984) showed that the lattice was stabilised by the formation of dopant-oxygen vacancies. For Gd and Eu doped UO_2 (Park and Olander 1992) and for Nd doped UO_2 (Park 1994), the oxygen potential data could be fitted by using a model in which Ln(III)-oxygen vacancy clusters led to the stabilisation of the UO_2 lattice by decreasing the availability of oxygen vacancy sites (required to incorporate oxygen when oxidation occurs). This means that fuel dissolution rates determined with average burnup fuel are valid also for high burnup fuel.

Similar increased stability towards oxidative dissolution is observed for the Pu-aggregates in spent or fresh MOX fuel (Carbol et al. 2009a, Jegou et al. 2010, Odorowski et al. 2016).

5.3 Spent fuel dissolution under deep repository conditions

When spent fuel comes into contact with bentonite porewater in a failed canister, after a short IRF pulse, the net release of actinides and of most fission products will depend on the UO_2(s) matrix dissolution rate, since the great majority of radionuclides (> 95%) are preserved there (Ferry et al. 2005). As discussed in the two previous sections, only the oxidative dissolution rate (release of U(VI)) could lead to high radionuclide releases from the canister. The rate depends on many parameters, both intrinsic (fuel burnup, surface area etc.) and environmental (temperature, pH, bentonite porewater composition, etc.). However, the most important ones are the redox conditions on the fuel surface.

As already mentioned in Section 5.1, a few months after repository closure, all the post-closure oxygen will be consumed by reducing minerals, bacteria or the canister, resulting in an oxygen free and reducing environment, as summarised in Curti et al. (2023). Such conditions are very difficult to realize in a laboratory; even the redox conditions in an Ar-flushed glove box with 1 or 0.01 ppm O_2 are very oxidizing compared to those expected in the repository. This is why such studies are difficult; even traces of O_2 would oxidize U(IV) to U(VI) or Pu (IV) to Pu(V). As it will be shown in the next section, both dissolved H_2 and Fe (II) can create such conditions at the fuel surface in a failed canister in the repository.

In the Swiss deep repository concept, relatively large amounts of dissolved hydrogen will be present during long time periods (Diomidis et al. 2016, Johnson et al. 2005, Bonin et al. 2000). A major hydrogen source is the anoxic corrosion of the massive carbon steel canisters (see eq. 3-1).

Another hydrogen source is the α-, β- and γ-radiolysis of water by the radiation of spent fuel. In the case of a canister defect and bentonite porewater intrusion, the anoxic corrosion of carbon steel gives rise to the production of hydrogen at a higher rate than its diffusive mass transport away from the canister. The concentration of dissolved H_2 in the solution inside the canister is expected to quickly exceed its solubility in aqueous media (see Section 3.7). Gas phase formation occurs when the sum of partial pressures of gas components (i.e., hydrogen and vapor) exceeds the aqueous phase pressuree a. For this reason, several studies of spent fuel leaching in the presence of hydrogen at pressures up to 5 MPa ($[H_2]_{diss}$ ~ 40 mM) or in the presence of metallic iron have been carried out.

The results of several published studies during the last two decades show a large impact of the presence of dissolved hydrogen (added or produced in situ by anoxic corrosion of Fe) in suppressing effectively the radiolytic fuel oxidation/dissolution process. For this reason, these tests are referred to as tests carried out under “reducing conditions”. As will be discussed below, the reducing conditions do not refer to the redox potential of the bulk solution, rather to complex interfacial phenomena occurring at the very surface of the spent fuel or α-emitting actinide oxide surfaces (see also Section 5.6).

5.4 Dissolution rates of spent UO_2 and MOX fuel under reducing conditions

To provide spent fuel dissolution rates for repository safety assessments, it is necessary first to examine results from various types of dissolution experiments, including radiolysis studies. In the summary presented below and in the accompanying figures, the results of selected critical studies are shown. They include only measurements that were performed under reducing conditions directly relevant to a repository in Opalinus Clay. This means that the large number of studies performed under anoxic (oxygen-free, but with no reducing agent present) or in the air atmosphere of a hot cell discussed shortly in Section 5.3 are purposely not included in the discussion or derivation of the dissolution rate for safety assessment, as they were carried out under conditions not reflecting the repository environment of interest. Finally, data from studies that involve measuring the dissolution rate in H_2 dominated solutions under flow conditions (e.g., Röllin 2001) are also excluded from the present compilation of representative dissolution rates. While such studies provide much insight, in particular illustrating that the dissolution rate is decreased significantly in H_2-saturated solutions relative to oxygenated solutions, the flow rates used are high enough that U(IV) remains undersaturated in solution at the fuel surface, maintaining a high non-oxidative dissolution rate (i.e. release of U(IV)) not representative of the conditions in the Swiss SF/HLW repository. In a repository in which diffusion controls mass transfer in solution, U(IV) concentrations will reach the saturation value soon after exposure of the fuel to porewater. As a result, the non-oxidative rate of SF dissolution will remain negligible under reducing conditions, see also Section 5.1.

Rates derived from UO_2 and MOX fuel leaching under reducing conditions. A large number of studies of fuel dissolution under reducing conditions have been carried out in the last two decades and the results will be discussed here. The first tests of fuel leaching in the presence of hydrogen indicated an unusual behaviour of the dissolved uranium and other redox sensitive nuclides during the initial leaching period (Fig. 5-1): their concentrations decreased instead of increasing, as they usually do during fuel leaching in the absence of hydrogen, due to the radiolytic oxidation of the fuel and the release of U(VI) and other oxidized nuclides. As discussed in Ekeroth et al. (2020) this decrease is due to the reduction of radionuclides originating from a pre-oxidized fuel layer and cannot be due e.g., to the precipitation of any U(VI) phase. A thin pre-oxidized layer always exists in fuel rods cut open usually several years before the leaching tests, due to the high sensitivity of U(IV) to oxidants. It is clearly seen in X-ray Photoelectron Spectroscopic analysis (XPS) of the fuel particle before leaching (Fig. 7 in Ekeroth et al. 2020). Further, this reduction occurs at the surface of the fuel itself (Albinson et al. 2003, Ollila et al. 2003, Cui et al 2008, Spahiu 2021). This means that the presence of dissolved hydrogen not only neutralizes completely radiolytic oxidants (Ekeroth et al. 2020, Spahiu et al. 2004, Carbol et al. 2005) but also causes reduction of pre-oxidized radionuclides. A closer look at the releases of non-redox sensitive fission products such as Cs, Sr and Mo during the first 2-3 samplings indicates clearly that their releases initially increase as a few pre-oxidized fuel layers dissolve during the first days, with releases ceasing once these layers had been removed (see Fig. 5-2).

The concentrations of uranium, the major component of the fuel matrix, decrease from 3×10^{-7} M at the start to 5×10^{-9} M after about 100 days and then remain constant at $2 – 3\ 10^{-9}$ M for more than 2 years (see Fig. 5-1). These concentrations are in excellent agreement with the solubility of UO_2(am) (Grenthe et al. 2020), which also means that there is only U(IV) in solution, because any U(VI) in solution would result in a concentration increase. U concentrations cannot be used to derive spent fuel dissolution rates, because no increase is noted, but they can be used to set an upper limit to the oxidative dissolution rate. This is because the disappearance from solution of the oxidative dissolution indicator (U(VI)) in the form of U(VI) solids, which occurred under oxidizing conditions, can be ruled out based on arguments presented in Ekeroth et al. (2020). The freshly precipitated UO_2(am) at the start of the test does not protect the fuel surface from oxidative

dissolution; on the contrary, it is the first to be oxidized and released in solution when accidental air intrusion occurs. This is revealed by U concentrations increasing to the same level as those at the start of the test, whereas other nuclides do not (Carbol et al. 2005, Spahiu et al. 2004). Less than 1% of the precipitated U was found in acid stripping of the autoclave (Albinsson et al. 2003) and more than 99% of the U was deposited on the fuel surface itself (Ollilla et al. 2003). Tests where special care was taken to avoid solution contact with metallic parts of the autoclave, including condensed water, were carried out (Spahiu et al. 2004) to dismiss any U reduction-precipitation elsewhere in the autoclave.

If U(VI) is reduced by the system spent fuel + dissolved hydrogen, it is difficult to imagine that the same system releases oxidized U(VI), but this can be assumed to illustrate a point about fuel dissolution rates. Thus, if the oxidative fuel dissolution would occur with a fractional rate of 10^{-6} a^{-1} in the tests described in Ekeroth et al. (2020), a gradual increase of the U concentration due to the produced U(VI) would occur, reaching 1.23 10^{-8} M after one year. No such increase is observed in this or any of the other reported fuel leaching studies under hydrogen (Spahiu et al. 2000, 2002, 2004, Carbol et al. 2005, Carbol et al. 2009a, Fors et al. 2009, Puranen et al. 2020, Puranen et al. 2022). This concentration increase would of course be greater in studies with a whole fuel pellet (~ 9 g), given the larger amount of U dissolved (Carbol et al. 2005, Loida et al. 2001, Loida et al. 2005). This means that oxidative fuel dissolution is either absent or occurs with a rate which is lower than 10^{-6} a^{-1}. As discussed in Spahiu (2021), it is very difficult to measure dissolution rates of the order of 10^{-8} a^{-1}, because the expected concentration increase, even for the most abundant nuclide in fuel (U), would be quite near the detection limit and the analytical errors in the sub-ppb concentrations (< 10^{-9} M) make the detection of such low rates difficult.

Similar conclusions are reached by an analysis of the concentrations of Np and Pu in the studies by Ekeroth et al. (2020) (Fig. 5-1) or Fors et al. (2009). The values measured are much lower than those corresponding to equilibrium with their corresponding reduced oxides, which rules out any presence of these elements in their oxidized states in the solutions. The observed concentrations below the solubility of the pure oxides are explained by the authors as due to the potential formation of an ideal solid solution during the initial reduction of the pre-oxidized nuclides. This solid solution would contain the actinide oxides of U, Pu, Np in the same proportions as they are in the fuel inventory. Given that Pu and Np are “diluted” ~ 100 to ~ 1'000 times respectively in the mixed solid as compared to U, the same holds for their concentrations in solution. Any trace of Np(V) or Pu(V) in the autoclave solution would result in orders of magnitude higher concentrations.

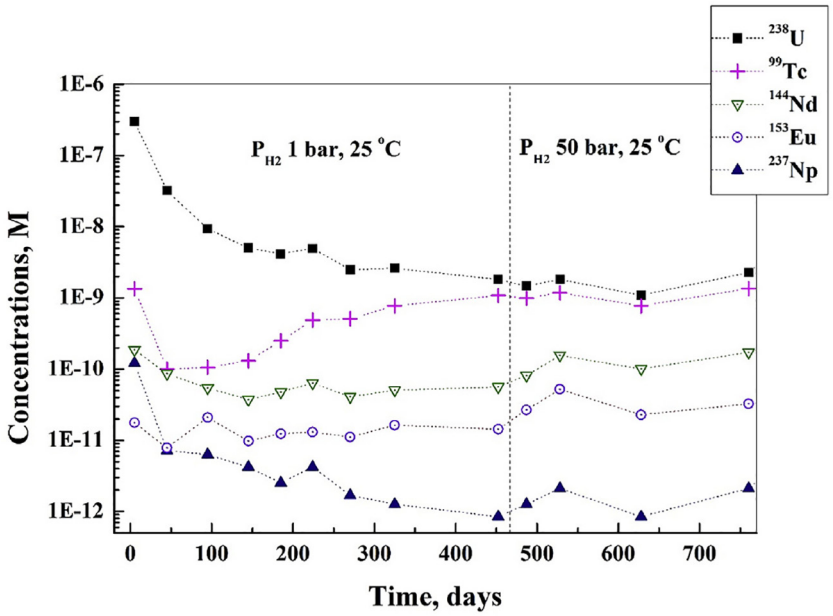

Fig. 5-1: Concentrations of ^{238}U, ^{99}Tc, ^{144}Nd, ^{153}Eu and ^{237}Np in solution at two different H_2 overpressures

Ekeroth et al. (2020)

It should be kept in mind that it is quite difficult to avoid U(IV) oxidation at near neutral pH as U(IV) is stable in solution only for extremely low oxygen fugacities ($P_{O2} < 10^{-65}$ atm, Rai et al. 1990). The air intrusion measured during the autoclave test of Ekeroth et al. (2020) (revealed by nitrogen levels reaching 1500 ppm) would cause an increase of the U concentrations much higher than 10^{-8} M. The absence of an increase of U levels means that the same system that causes the reduction of pre-oxidized nuclides (fuel surface + dissolved H_2) also neutralises any influence of intrusive oxygen. The strong reducing capacity of this system is noticed especially in some experiments carried out with the addition of 0.1 mM or 1 mM bromide in the 5 M NaCl (Loida et al. 2007) or 6 *m* NaCl (Metz et al. 2007) leaching solution. Bromide is a known OH-radical scavenger, since it reacts with the OH-radical about 250 times faster than molecular hydrogen (Zehavi and Rabani 1972) and thus cancels any beneficial effect of molecular hydrogen under radical rich β, γ-radiations. Separate tests in 5 M NaCl solutions with added bromide in the presence of H_2 showed extensive production of molecular radiolytic oxidants under external γ-radiation and oxidation of an added unirradiated UO_2 pellet (Metz et al. 2007). However, in tests with spent fuel in Br-containing solutions, where the intrinsic γ-radiation of the fuel has apparently created the same conditions in the bulk solution, the measurements show an absence of molecular oxidants in the autoclave, as well as low and decreasing concentrations of U or Pu (Loida et al. 2007). In this case, since no beneficial effect of H_2 is expected in the case of homogeneous α-radiolysis (Bauhn et al. 2017, see also Section 5.9), it follows that only surface mediated processes can be responsible for the consumption of the molecular oxidants produced near the fuel surface by α-radiation and especially in the bulk solution by the intrinsic γ- or β-radiation of the spent fuel.

The redox conditions in the autoclave during the two-year leaching test of Ekeroth et al. (2020) are quite similar to those during the first days when a reduction of pre-oxidized nuclides occurred. It is very difficult to imagine e.g., that some parts of the fuel release U(VI), which is later reduced in some other parts of the fuel. This is ruled out by corrosion potential measurements of

Broczkowski et al. (2005, 2010), which confirm that the whole fuel surface reaches very negative potentials. This demonstrates that the epsilon particles are galvanically coupled to the UO_2 matrix, hence the whole surface behaves uniformly.

The results of the leaching of MOX fuel under a H_2 atmosphere (Carbol et al. 2009a) exhibit similarities to experiments conducted with UO_2 fuel, i.e., a decrease of all redox sensitive radionuclide concentrations to values corresponding to equilibrium with their reduced oxides, constant long-term levels of ^{137}Cs, as well as lower releases from fuel regions containing Pu-agglomerates.

Support for below detection limit releases of U(VI) from fuel under reducing conditions comes also from a few studies carried out with spent fuel (Grambow et al. 1996a, Carbol 2005, Puranen et al. 2017, Puranen et al. 2020) or Pu doped UO_2 (fresh MIMAS MOX fuel, Odorowski 2015) in the presence of *metallic iron* and under an initially Ar atmosphere. It is well known (Farrell et al. 1999, Fiedor et al, 1998, Gu et al. 1998, Morrison et al. 2001, Grambow 1996b, Cui 2002) that iron reduces U(VI) from solution and precipitates it as UO_2(s). Under oxygen-free conditions, magnetite reduces U(VI) to U(IV) and precipitates UO_2(s) (Pan et al. 2020, Latta et al. 2014, Scott et al. 2005), while green rust on iron surfaces precipitates UO_2(s) (Cui and Spahiu 2002, O`Loughlin et al. 2003). In the above studies, the presence of iron in the same vessel means that a few cm from the fuel surface there exists a U(VI) detector, because U(VI) released by oxidative dissolution of the fuel surface would be reduced and collected on the iron surface. The analysis of iron surfaces in the above studies showed U levels indicating only U(IV) sorption on the corresponding surfaces. No accumulation of uranium as UO_2 on iron was observed. This also supports the argument that the rate of oxidative dissolution is below the detection limit under reducing conditions. However, based only on the experimental data, it is very difficult to determine fractional dissolution rates of the order of 10^{-8} a^{-1}. On the other hand, as will be shown below, there is plenty of evidence that fractional dissolution rates higher than 10^{-6} a^{-1} can be ruled out.

As stated in Section 5.2 fractional fuel dissolution rates of the order of ~ 3.7 10^{-5} a^{-1} were determined based on Sr-releases for oxidative fuel dissolution. The tests were done in a hot cell atmosphere (very few with Ar flushing) and usually two pellets (~ 18 g fuel) together with cladding were leached in 200 ml of solution. This means that after one year ~ 0.67 mg of fuel was dissolved, corresponding to an amount of ^{90}Sr in fuel with the same inventory as the one used in (Ekeroth et al. 2020) of 2.98 10^{-7} g or 3.3 10^{-9} moles. This corresponds to a 1.5 ppb ^{90}Sr increase over one year, a concentration increase that can be easily detected with ICP-MS or radiochemical analysis. Much higher Sr releases during one year (from a few ppb at short times to more than 40 ppb after 376 days) are reported for tests with two fuel pellets carried out under Ar by Spahiu et al. (2004).

In the case of dissolution of 2 g fuel under reducing conditions in 800 ml solution (Ekeroth et al. 2020), in order to detect dissolution rates lower than 10^{-6} a^{-1}, one would have to detect Sr-90 releases of 8.94 10^{-10} g or 9.94 10^{-12} moles over one year. This means that over one year the Sr-90 concentrations would increase by only 0.0012 ppb. Concentration increases of 1.2 ppt are hardly measurable with any of the existing analytical methods and it is questionable whether such low concentrations can be measured using clean room techniques. Furthermore, it is difficult to detect such low changes given the background of ^{90}Sr (e.g., 0.15 – 0.24 ppb in the test reported in Spahiu et al. 2004) released as an instant release fraction and by the dissolution of the pre-oxidized layers. This effect causes the oscillations observed around zero behaviour of calculated FRR[6] (see Fig. 5-3). In any case, the fractional release rates of Cs, Sr and Mo measured in most leaching tests clearly show a decrease following the dissolution of pre-oxidized fuel layers, eventually

[6] There is no measurable Sr released between two intervals, an overestimation in the previous point causes negative values in the next point.

oscillating around zero. There are also a few long-term tests where no more releases are detected after a certain point in time (termination of Cs releases in Spahiu et al. (2004) tests, illustrated in Fig. 2 of Cui et al. (2008), Sr release termination in Spahiu et al. (2002) tests, illustrated in Tab. 3-8 of Carbol et al. (2005), Puranen et al. (2020), Puranen et al. 2022), see Tab. 5-1 for more details.

Finally, tests carried out with sealed glass ampules containing 1 g fuel in 30 ml of carbonate solution under initially pure Ar atmosphere showed constant levels of radiolytic O_2 and H_2 in the gas phase and for practically all radionuclides in solution for ampules analysed after 1, 2 and 3 years (Cera et al. 2006, Eriksen et al. 2008). This demonstrates that radiolytically produced hydrogen accumulated after ~ 1 year was sufficient to completely stop further dissolution of the fuel. If H_2 and O_2 are continuously produced by radiolysis during the entire duration of the experiment, there seems to be no other possible explanation for the constant H_2 and O_2 levels measured in the ampoule after the first year, other than their catalytic recombination to water.

Pastina and LaVerne (2021) have compiled a list of studies of dissolution of spent fuel and alpha doped UO_2 illustrating that dissolution rates of spent fuel are very low and are clearly less than 10^{-6} per year under truly reducing conditions. Much of the information in their table does not provide direct measurements of the fractional dissolution rate of spent fuel. The reason for this is illustrated in Fig. 5-3 and the discussion of fractional release rates for ^{90}Sr in the previous pages. A subset of the data provided in Table 1 from Pastina and LaVerne (2021) is given in Tab. 5-1, along with more information. The first column provides identification of the fuel type studied, with the reducing agent present (H_2 or metallic Fe). The second column gives the alpha activity of the sample. The third column provides comments on the estimated dissolution rate given by the primary authors, whose references are given in the fourth column. In many of these studies, no dissolution rate was reported by the authors, as the rate declined to values indistinguishable from zero within the analytical uncertainties and thus, ultimately, was not measurable.

Measured dissolution rates from experiments performed with alpha-doped UO_2 (see Section 5.5) are also included in Tab. 5-1, along with some rate values taken from studies involving radiolytic model calculations, see Section 5.6.

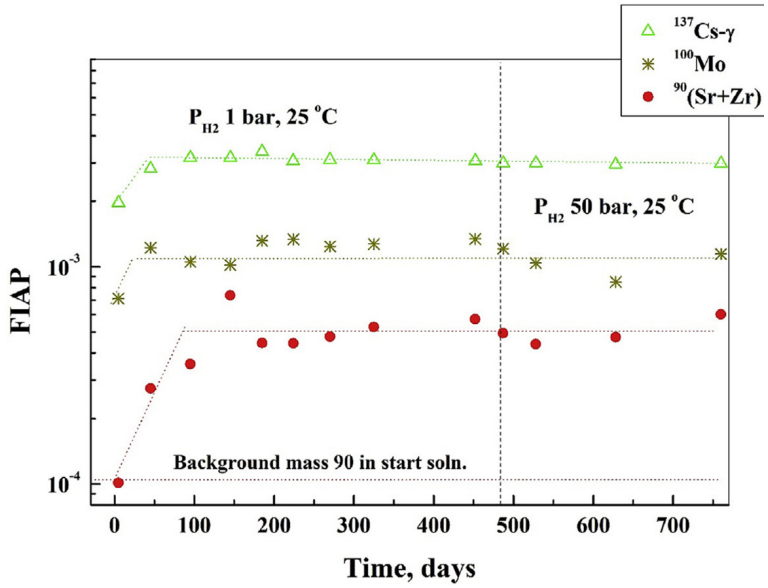

Fig. 5-2: FIAP (Fraction of Inventory in Aqueous Phase) of Cs, Mo and 90(Sr+Zr) in solution at two different H_2 overpressures

Ekeroth et al. (2020)

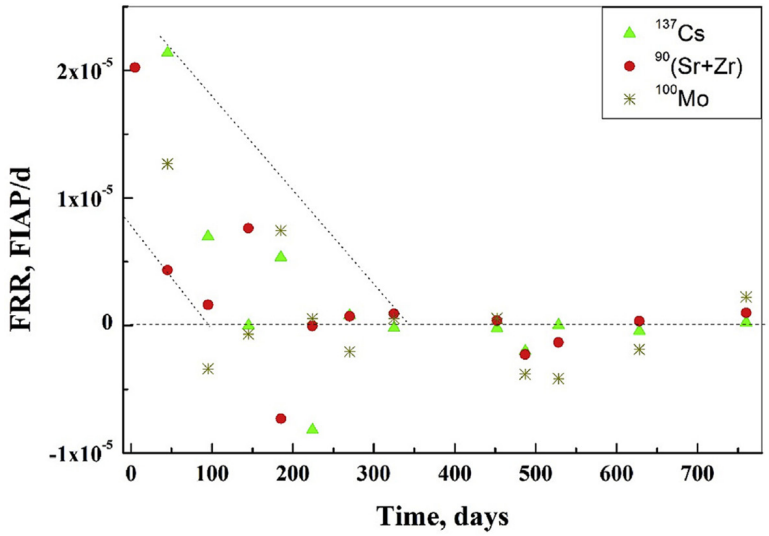

Fig. 5-3: Fractional release rates (FRR) of ^{137}Cs, ^{100}Mo and $^{90}(Sr+Zr)$ in solution in units of FIAP/day

Ekeroth et al. (2020)

Tab. 5-1: Compilation of representative dissolution rates for UO_2 fuel and MOX fuel and alpha-doped UO_2 for reducing conditions (adapted from Pastina and LaVerne (2021), along with more information)

The reducing agent in the experiments and calculation cases are given in brackets in the first column.

Sample (reducing agent)	**Activity** [Bq g^{-1} UO_2]	**Comments by the authors**	**Reference**
PWR segment (H_2, Fe(s)) 50 MWd/kg_{iHM}	5×10^8	Decreasing rate with proposed rate of 4×10^{-7} a^{-1} based on (Fe(s)) data	Carbol et al. 2005
PWR powder (H_2) 43 MWd kg_{iHM}	3.8×10^8	Less than one monolayer of fuel dissolved based on Sr release. Termination of Cs releases after ~ 350 days (Fig. 2 in Cui et al. 2008)	Spahiu et al. 2004
PWR powder (H_2) 43 MWd kg_{iHM}	3.8×10^8	Decreasing rates over > 1 a. Termination of Sr releases after 408 days (Tab. 3.8 in Carbol et al. 2005)	Spahiu et al. 2002
PWR fragments (H_2) 43 MWd kg_{iHM}	3.8×10^8	U concentrations drop from $3\ 10^{-7}$ to $2\text{-}3 \times 10^{-9}$ M then practically constant over > 2 year in spite of extensive air intrusion. Absence of fuel surface oxidation based on XPS analysis	Ekeroth et al. 2020
MOX fuel fragments (H_2), 47.5 MWd/kg_{iHM}	2.5×10^9	Decrease of U from $5\ 10^{-7}$ to ~ 10^{-9} M in ~ 200 days, of Pu and Np 10 to 100 times lower than U, termination of Cs release after ~ 600 days of a 2'078 day experiment	Carbol et al. 2009a
Fragments from the outer 1 mm of a PWR pellet (H_2), 67 MWd/kg_{iHM}	1.15×10^9	U drops from 10^{-8} to $2\ 10^{-10}$ M in 62 days. 3.4% of Cs inventory released in the first 7 days, out of the 3.5% total Cs release during the 500 day experiment	Fors et al. 2009
PWR fragments (H_2) 43 MWd kg_{iHM}	3.8×10^8	Termination of radionuclide release after 243 days of 1'240 day experiment, UO_2 (am) solubility reached	Puranen et al. 2020
PWR fragments (H_2) 75 MWd kg_{iHM}	1.34×10^9	Termination of Cs and Sr release after ~ 100 days of a 463-day experiment	Puranen et al. 2022
UO_2 un-doped (Fe)	1×10^4	8.3×10^{-8} a^{-1} (min) 1.6×10^{-6} a^{-1} (max)	Zetterström-Evins et al. 2014
UO_2 doped with 5% ^{233}U (Fe)	1.6×10^4	7.5×10^{-8} a^{-1} (min) 1.1×10^{-6} a^{-1} (max)	Zetterström-Evins et al. 2014
UO_2 doped with 10% ^{233}U (Fe)	3.1×10^4	4.4×10^{-8} a^{-1} (min) 1.2×10^{-6} a^{-1} (max)	Zetterström-Evins et al. 2014

Tab. 5-1: Cont.

Sample (reducing agent)	Activity [Bq g^{-1} UO_2]	Comments by the authors	Reference
UO_2 doped with 10% ^{233}U (H_2)	3.3×10^4	Decreasing total U concentrations over 328 days. XPS analysis of the pellet surface after test shows $UO_{2.00}$	Carbol et al. 2009b
Radiolytic model rate combined with surface reaction kinetics for fuel with a burnup of 38 MWd kg_{iHM} (H_2)	5×10^8	Report very low critical H_2 concentrations that stop oxidative dissolution of fuel aged 10^2, 10^3 or 10^4 years.	Jonsson et al. (2007) Trummer & Jonsson (2010)
Radiolytic model combined with surface reaction kinetics for CANDU fuel (H_2)	1.0×10^7	Rate < 3.2×10^{-13} mol m^{-2} a^{-1} after 50 hours (< 10^{-12} a^{-1}). For critical H_2 concentrations, see text.	Liu et al. (2017)

5.5 Rates based on alpha doped UO_2 dissolution under reducing conditions

Since studies with spent fuel use material that has decayed for only one or two decades, the radiation field is quite different from that of the fuel which will contact water in the repository, because at that time old fuel will emit mainly alpha radiation (Section 5.2) with much lower dose rates. To simulate the radiation field of a few thousand-years-old fuel, UO_2 containing different fractions of short-lived α-emitters, the so-called *α-doped UO_2,* has been used to study the effects of α-radiolysis on the corrosion behaviour of aged spent fuel. The doping level is reported as the content of the α-emitter (% ^{233}U or ^{238}Pu) or as the specific activity (MBq/g). By using the calculated activity decay in the spent fuel of a certain burn-up with time, α-doped samples are also referred to by the equivalent fuel age, e.g., "3'000 y old fuel", which is equivalent to ~ 33 MBq/g or 10% ^{233}U.

The results of static batch leaching under Ar flushing (Rondinella et al. 2004) in carbonate-containing solutions indicated that α-radiolysis enhances uranium dissolution for pellets doped with 10% ^{233}U (3'000 y old fuel), while in the case of lower doping levels such as 1% ^{233}U, corresponding to 3.3 MBq/g, (~ 30'000 y old fuel), it was difficult to observe any effect of the α-radiolysis on the increase of the U concentrations with time. The α-radiolysis of a few tens of microns thick water layer near the UO_2 surface is expected to produce mainly molecular radiolytic products such as H_2O_2 and hydrogen (Spinks and Woods 1990). As already discussed, U(IV) ions in solution or in the UO_2 solid are oxidized very quickly by traces of oxidants such as H_2O_2 and O_2 (Baker and Newton 1961, Newton 1975, Elliot et al. 1986). Any oxidized U(VI) contributes to the increase of U concentrations in the presence of bicarbonate ions, which form strong complexes with U(VI). In spite of the relatively sensitive measurement methods for low uranium concentrations and the absence of any other reductants than radiolytic H_2, no detectable increases were observed during the whole duration of the experiment with the 3.3 MBq/g pellet (Rondinella et al. 2004). The authors therefore proposed a *threshold of α-activity* between 3.3 MBq/g (where no effect on U was observed) and 33 MBq/g (effect observed), below which no effect of α-radiolysis could be observed. Later, Muzeau et al. (2009) observed no U increases with ^{238}Pu-doped pellets of activity 18 MBq/g and proposed this new specific activity level as the lower limit for detecting α-radiolysis enhanced dissolution. This means that the effect of α-radiolysis is expected to be much more limited than that predicted with radiolytic models (see also Section 6.4 on radiolysis effects in the Cigar Lake natural analogue) which rely on *radiolytic yields* or G-values measured in free water irradiated with He-nuclei accelerated to 5 MeV energy. G-values

may however be different when the α-particles are emitted from an UO_2 surface, if one considers all the complex phenomena which occur in such surfaces (Pastina & LaVerne 2021, see also Section 5.6). In any case, the fuel dissolution rates discussed previously do not take into account this threshold phenomenon, hence they are in this respect pessimistic.

Ollila (2006, 2008) & Ollila and Oversby (2005, 2006) studied corrosion of alpha-doped UO_2 under anoxic and reducing conditions. The ^{233}U concentrations of 5% and 10% represent fuel decay times of 10'000 years and 3'000 years, respectively. Note that this material contains no ϵ-particles, thus any reaction of H_2 on the surface must be due only to interfacial effects, e.g. as discussed by Pastina and LaVerne (2021), which have been shown to be much weaker than on a true spent fuel surface (Shoesmith 2007). Their findings indicate that the presence of corroding iron or trace amounts of sulphide in solution cancelled any oxidative effects of radiolysis. Measurements of U release from alpha-doped UO_2 samples yielded dissolution rates of less than 10^{-7} per year. These rates are based on the total amount of U released (including that stripped from the reaction vessel) determined thanks to isotope dilution techniques in spite of the attainment of the solubility limit. Zetterström Evins et al. (2014) continued these studies and extended them by measuring dissolution rates in brackish and saline waters with corroding Fe present. It should be noted that in these experiments, the H_2 concentration in the solution, produced only by Fe corrosion, would have been relatively small. Therefore, the principal reducing agent consuming radiolytic oxidation products in those experiments would be Fe^{2+}. The dissolution rates were similar to those measured in the presence of H_2, but slightly higher, typically in the range 10^{-6} to 10^{-7} a^{-1}. Grambow et al. (2017) noted that less than a monolayer of UO_2 must have been involved in the reaction to explain these results.

Odorowski et al. (2017) leached highly doped pellets (385 MBq/g UO_2) in Callovo-Oxfordian simulated groundwater and in the presence of metallic Fe foil under an Ar atmosphere from the start. The results showed very low uranium concentrations in solution, corresponding to the solubility of $UO_2 \cdot xH_2O$ after more than one-year of leaching. The analysis of the uranium sorbed or precipitated during the test through autoclave and iron foil acid stripping indicated that very little total U was released during the whole test (~ 10 µmol). Most of it was sorbed on the Ti walls of the autoclave, corresponding to the calculated values of K_d for sorption of U(IV) on TiO_2. Akaganeite (Fe(III)oxyhydroxide) was detected on the MOX pellet surface, indicating that Fe (II) ions released from the foil reached the surface of the pellet. The authors conclude that Fe (II) produced by iron corrosion completely cancels the oxidative dissolution of these highly doped pellets. In her Ph. D. thesis, Odorowski (2015) reports similar data for the leaching of an unirradiated MOX pellet with alpha activity 1.3×10^9 Bq/g, i.e., with a very high alpha dose rate, in the presence of an iron foil. The same unirradiated MOX pellet dissolved relatively quickly in an aerated or Ar purged atmosphere (Odorowski et al. 2016). In the Disco project this same research group reported similar effects of iron foils for a fresh MOX pellet with 27% Pu, i.e., with a very high α-activity. Even in this case, Fe precipitation on the MOX surface was observed. However, in this case, magnetite, a solid containing both Fe (II) and Fe (III), precipitated instead of akageneite which contains only Fe (III). These experimental results indicate that even Fe (II) ions diffusing to the fuel surface from corroding metallic iron can neutralize completely radiolytic oxidants produced within ~ 35 µm from the fuel surface.

5.6 Fuel dissolution mechanism under reducing conditions and its application to models

Many studies have attempted to calculate UO_2 and spent fuel dissolution rates with radiolytic models. These calculations rely on the knowledge developed over decades in the study of radiolysis reactions in solution and on UO_2 surface reaction rates derived from chemical and electrochemical studies of UO_2 dissolution kinetics. The approaches and findings are summarised in Spahiu (2021, Section 16). A common feature of most of these models is the explicit inclusion of the effect of H_2 on spent fuel dissolution rates by ε-particle catalysis. It was first demonstrated in the electrochemical studies of Broczkowski et al. (2005), that the ε-particles are galvanically coupled to the UO_2 matrix, i.e., they enforce negative corrosion potentials to the fuel surface in the presence of dissolved H_2. The most important process in the action of H_2 is the reduction of the oxidized U atoms on the fuel surface by electrons taken from dissolved H_2 via ε-particle mediation. It was shown that this process is diffusion controlled[7] (Jonsson et al. 2007, Trummer et al. 2008, 2009). The experimental determination of kinetic constants for other important interfacial reaction rates resulted in advanced models such as the KTH steady state model (Jonsson et al. 2007, Roth and Jonsson 2008, Eriksen et al. 2008) and the UWO, Canada model (Wu et al. 2012, Liu et al. 2016, Liu et al. 2017).

The steady state model predicts that as little as 0.1 bar H_2 (named *critical H_2 concentration*) will effectively inhibit the oxidative dissolution of the spent fuel aged 100 years or more, while in the presence of 1 μM Fe^{2+}, even 0.01 bar H_2 will be sufficient to stop oxidative fuel dissolution (Jonsson et al. 2007). The effect of Fe (II) ions in bulk solution was introduced in the model by considering an appropriate function of the rate constant that reduces the H_2O_2 concentration at the fuel surface. Critical hydrogen concentrations that completely cancel oxidative fuel dissolution as a function of fuel age (α dose rate) are reported in Trummer and Jonsson (2010). For fuel with a burnup of 38 MWd/kg_{iHM} and 1'000 years old, the critical H_2 concentration is 3×10^{-8} M while for the alpha dose rate of a 10'000-y old fuel, the critical H_2 concentration is 5.4×10^{-9} M, corresponding to hydrogen partial pressures of 3.8×10^{-5} bar and 6.8×10^{-6} bar, respectively.

Liu et al. (2016) determined, through modelling, the separate effects of radiolytic H_2 (internal to a fuel crack) from that produced by iron corrosion (external) on the suppression of spent fuel corrosion for different fracture or crack geometries, α-radiation dose rates and concentrations of external H_2. The hydrogen produced by α-radiolysis was found more important in suppressing fuel dissolution deep in the fractures than external H_2. Critical H_2 concentrations for the dissolution of 1'000 y old CANDU fuel with burnup 9.2 MWd/kg_{iHM} were 5.7 10^{-6} M for fuel fractures as compared to 3.3 10^{-7} M for planar fuel surfaces. The consumption of H_2O_2 by Fe (II) in bulk solution was introduced based on published rate constants. Later, the model was successfully tested with experimental data on α-doped UO_2 dissolution, and also used to investigate the influence of oxygen from H_2O_2 decomposition and radiolytic H_2 accumulation in a closed system on fuel dissolution (Liu et al. 2017). The calculations showed that although the radiation dose rate, the surface coverage of ε-particles and the H_2O_2 decomposition ratio all influenced the short-term corrosion rate, the radiolytically produced H_2 had an overwhelming influence in reducing the rate below 3.3 10^{-13} mol m^{-2} a^{-1} (< $10^{-12}a^{-1}$) after about 50 hours.

At present there is substantial progress in modelling the effects of dissolved hydrogen on spent fuel dissolution, mainly based on the action of ε-particles, which are known hydrogen catalysts, but they are not present in α-doped UO_2. Recently an interesting study was published discussing the complicated interfacial processes that occur on the surface of alpha emitting actinide oxides (Pastina and Laverne 2021). These authors noted that, in addition to the reaction of H_2 on ϵ-particles, there are several additional mechanisms that may also play a role in keeping the spent

[7] Diffusion limited (or controlled) rate is the term used in kinetics for particles which react immediately when they diffuse through solution to contact each other, i.e., diffusion is the rate limiting step.

fuel surface in a reduced state. These include the formation of radiolytic species (including defects and excited states) in the solid and in the first water layers in contact with its surface, leading to the formation of excess H_2 by processes occurring at the surface of spent fuel and in confined water volumes. They suggest that the long-term fractional dissolution rate (10^{-7} a^{-1}) used in most long-term safety assessments is an overestimate because this rate assumes that there is a net UO_2 oxidation rate caused by radiolysis.

Studies related to the long-term solid-state structural stability of UO_2 have dealt with the topics of alpha-radiation damage, self-irradiation enhanced diffusion and helium build-up. Spahiu et al. (2021, Section 17) has noted, based on the work of Ferry et al. (2008), that the atom mobility arising from α-decay effects in spent fuel is so low that the release of fission products to grain-boundaries should not be significant even over the long-term. In addition, the helium produced by alpha-decay is not sufficient to produce micro-cracking of grains in UO_2 fuel for several hundred thousand years (Ferry et al. 2010).

5.7 Estimated range of dissolution rate of spent fuel

Derivation of a dissolution rate of spent fuel for a repository safety assessment cannot realistically be made based only on direct measurement of radionuclide release rates from spent fuel samples under repository-relevant conditions, as most of the measurements result in zero or less-than zero rate values due to detection limit issue. However, the experimental data indicate that the dissolution rate of the fuel matrix under reducing conditions is very low. Thus, the rate recommended to be used in safety assessment is based on multiple lines of arguments, including:

- conditions in the repository, which ensure that H_2 concentrations in bentonite pore water will remain high for hundreds of thousands of years
- reaction of H_2 with ϵ-particles in the fuel, which will maintain the reduced state of the fuel surface at a composition close to $UO_{2.00}$
- spent fuel dissolution studies in solutions containing H_2 which yield greatly decreasing rates over periods of months, followed by immeasurably low release rates after the solubility of UO_2 (am) is reached. Similar results are reported from studies of fuel leaching in presence of metallic Fe in an initially Ar atmosphere, where H_2 and Fe(II) are produced *in situ* by Fe corrosion.
- low dissolution rates of alpha-doped UO_2 (representative of aged spent fuel) in reducing solutions, combined with chemical and isotope dilution measurement techniques.
- experimental findings from the DISCO project, which show that fuel dissolution rates of doped fuel (Cr and MOX) are in the same range as those of standard UO_2 fuel (Evins et al. 2021)
- natural analogue studies which illustrate that uraninite remains stable over geologic time frames
- upper limit of analytical uncertainties in direct measurements (see Section 14 in Spahiu 2021)
- modern modelling approaches using experimentally determined interfacial reaction rates for fuel dissolution under reducing conditions, which support very low rates and at the same time clarify the mechanism of reductant action on the fuel surface

Based on these arguments, the spent fuel dissolution rate proposed for use in safety assessment calculations is 10^{-7} a^{-1}, with upper and lower limits of 10^{-6} a^{-1} respectively 10^{-8} a^{-1}.

5.8 Conditions for which the fuel dissolution rates are valid

The fuel dissolution rates proposed in this section, with their uncertainty range, should be valid for all relevant fuel types and water compositions under the reducing conditions expected in the Swiss repository.

The fuel to be disposed of consists predominantly of UO_2 fuel and to some extent also of MOX fuel (Mixed Oxide; Tab. 2-1). UO_2 fuel doped with Cr (see Section 2.1) is also present in the inventory. The burnup ranges and other fuel properties are described in Section 2.

The water composition influences both the radiolytic reactions and the kinetics of matrix dissolution. The most important factors are the redox conditions and the composition of the groundwater; including its pH, ionic strength, and the concentration of major components (such as carbonates, sulphates, chloride, etc.) and minor components (such as trace metal ions, bromide, etc.), which affect the radiolytic reaction chains and the dissolution process. In addition, the temperature may also affect the fuel dissolution rate.

5.8.1 Fuel type and burnup

The analysis of data from high temperature oxidation of spent fuel as a function of burnup shows that the increase of fission products and minor actinides contents with burnup makes fuel oxidation more difficult (Hanson 1998, Cobos et al. 1998). The available fuel leaching studies (Jegou et al. 2004, Hanson 2008, Clarens et al. 2008, Ekeroth et al. 2009) which cover a large range of fuel burnups show no significant influence of the burnup on the oxidative dissolution of the UO_2 fuel matrix. They indicate that the increase of UO_2 doping levels by fission products and actinides successfully compensates the increased radiation field and surface area of the high burnup fuel. Dedicated studies of HBU (High Burn-Up) UO_2 fuel or MOX fuel under reducing conditions show no measurable influence of the increased burnup (Fors et al. 2009, Carbol et al. 2009a, Puranen et al. 2022). The results of the EC-Project DISCO show that Cr-doped UO_2 fuel behaves quite similarly to UO_2 fuel under reducing conditions (Barreiro-Fidalgo et al. 2020). For all these reasons the data provided in the literature review in this section are considered to be valid also for the higher burnup fuels (Section 2.1, Table 2.1) in the Swiss fuel inventory.

5.8.2 Redox conditions

After canister failure, hydrogen production through water radiolysis and corrosion of the iron canister will continue for tens of thousands of years. As long as there is corroding iron, both hydrogen and Fe(II) concentrations will be sufficient to assure reducing conditions. Because the water invading the failed canister from the bentonite buffer contains sulphate, microbial sulphate reduction might potentially result in the precipitation of Fe(II)-sulphide. However, based on the arguments discussed in Section 3.6, this scenario is very unlikely, and therefore sulphate reduction was excluded from the calculations presented in Section 3.7. After completion of the canister corrosion process, hydrogen concentrations may decrease but hydrogen will still be produced by water radiolysis when all metallic iron has corroded. By that time, however, the intensity of alpha radiation will be too low to induce oxidative fuel dissolution under the reducing conditions expected in the repository. In the longer term, at thermodynamic equilibrium the Fe(II) concentrations and the redox potential of the water inside the canister will be determined by equilibrium with magnetite and siderite.

Other environmental parameters (temperature, pH etc.) affect in various degrees the dissolution rate under oxidising conditions, but are discussed below only for reducing conditions.

5.8.3 pH

The pH of the groundwater affects the solubility of UO_2(s), which is the main component of the fuel matrix. The solubility of UO_2 increases at low pH, especially at pH values lower than 3. Spent fuel experiments carried out in the interval $4 < pH < 9.6$ show that in this interval, the dissolution rate is largely independent of pH (Röllin et al. 2001) under reducing conditions. Below pH 4, an increase of the dissolution rate was observed, due to the increased solubility of UO_2. Measurements in fresh concrete water (pH 13.5) with or without the presence of Bure clay indicate a limited (if any) effect of high pH waters on the fuel dissolution rate (Loida et al. 2006, Loida et al. 2012). Since the pH of the water inside the canister is calculated to lie within the restricted pH-range of 7.2 – 8.4 (see Tab. 3-8), no pH-related effect is predicted for the Swiss repository environment.

5.8.4 Ionic strength, major and minor groundwater components

Most of the spent fuel dissolution data discussed here were obtained in dilute simulated groundwaters. An increase of the ionic strength affects, in principle, solubilities and other thermodynamic data, as well as kinetic constants. The predicted composition and characteristics of a typical water in contact with the fuel is given in Section 3.7. Taking into account the variability of Opalinus Clay and bentonite porewaters (Section 3.2.3), ionic strengths will be low to moderate and limited to 0.3 – 1.1 M (Tab. 3-6). The dominating background electrolytes are NaCl and to a lesser extent Na_2SO_4.

Data from leaching of alpha-doped pellets under anoxic and reducing conditions in 0.5 and 1 M NaCl solutions, as well as (Na,Ca)Cl solutions with ionic strength of 0.625 M, show no influence of the increased salinity on the dissolution rates (Ollila 2008). Furthermore, during spent fuel leaching in the presence of metallic iron or hydrogen, very low dissolution rates are measured, without any marked influence of the high ionic strength (Grambow et al 1996a, Grambow et al 2000, Carbol et al. 2005). In view of the above discussion, the fuel dissolution rates suggested in this section are considered to be valid in groundwater of up to 1 M ionic strength, while no major influence is expected even at higher ionic strengths.

Carbonate, and to a much lesser extent sulfate, forms strong U(VI) complexes and enhances fuel oxidative dissolution rates (Shoesmith 2000, de Pablo et al. 1999). On the other hand, U(IV) carbonate complexes only form at much higher carbonate concentrations than those of typical Swiss groundwaters (Ciavatta et al. 1983, Grenthe et al. 2020). Experimental fuel leaching data under reducing conditions show no marked influence of carbonate up to concentrations of 0.01 M (Rollin et al. 2001). No experimental fuel data are available for higher carbonate concentrations, but some precaution is necessary at carbonate concentrations higher than 0.1 M, in view of the potential solubility increase of UO_2 due to the formation of U(IV)- tetra and -pentacarbonate complexes. The fuel dissolution rates suggested in this section are considered to be valid for HCO_3^- concentrations below 0.01 M, and some caution is necessary at higher carbonate concentrations. The computed carbonate concentrations of the bentonite pore waters discussed in Section 3.2.3 vary from 0.001-0.005 M range and are thus always within the range of validity.

In most spent fuel leaching tests under reducing conditions, the presence of major groundwater cations such as Ca and Mg has been avoided, in order to prevent precipitation of potential sparingly soluble U(VI) solids which would make data interpretation difficult. The presence of Ca and Si in the groundwater has a beneficial effect, as these elements significantly decrease the rate of oxidative dissolution of spent fuel (Tait et al. 1997, Santos et al. 2006, Cui et al. 2003) and for this reason they are not discussed further.

5.8.5 Minor groundwater components, bromide

The beneficial effect of molecular hydrogen in homogeneous radiolysis is based on its reaction with the OH· radical, which converts the very oxidizing radical (OH·) to water and a very reducing radical (H·): H_2 + OH· = H_2O+ H·. Bromide ions are strong reductants and react ~ 250 times faster with the OH-radical than OH· with the H_2 molecule. It is reported that bromide scavenges the OH· radical, thus decreasing the beneficial effect of hydrogen on homogeneous water radiolysis (Metz et al. 2007). This competition could potentially cancel any beneficial effect of molecular hydrogen in bulk solution for radical-rich β, γ-radiations. However, β, γ- radiations are expected to have decayed to negligible levels after a few hundred years and at the time of canister failure in the repository, α-radiation dominates in spent fuel. The study of Bauhn et al. (2017) showed that the production of oxidants by homogeneous α-radiolysis of ^{238}Pu solutions under 10 bar H_2 was unaffected by the presence of bromide, i.e. bromide does not have the same detrimental effect on dissolution rate of UO_2 in the case of alpha radiolysis of hydrogen-saturated solutions as in the case of β-, γ- radiolysis. The reason is that the OH· radicals in the case of alpha radiation are produced in narrow and dense tracks in the solution, and quickly recombine. In addition, the produced oxygen and hydrogen peroxide under 10 bar Ar or H_2 atmospheres were quite similar. Finally, as discussed in Section 5.4, experimental data from fuel leaching clearly indicate that the interfacial processes at the spent fuel surface in the presence of dissolved hydrogen neutralise also the oxidants produced in bulk solution by β- and γ-radiolysis (Loida et al. 2007).

5.8.6 Temperature

The temperature affects radiolytic and dissolution/precipitation reactions. Dissolution of fuel at higher temperatures is only an issue in case of very early (a few years to a few hundred years) canister failure. As discussed above, very early canister failure is associated with a high hydrogen partial pressure, ensuring reducing conditions. At later times, the temperature in the canister is expected to have decreased to near ambient.

Available data with fresh fuel at 70 °C in the presence of 1, 5, and 50 bar H_2 (Ekeroth et al. 2020, Cui et al. 2008, Spahiu et al. 2000, 2004) do not indicate elevated dissolution rates, but rather higher rates of reduction and precipitation of U(VI) and other oxidized radionuclides. There are no published data for temperatures over 70 °C for fuel leaching under reducing conditions, and thus the fuel dissolution rates suggested in this section are considered to be valid for temperatures up to 70 °C. In general, a temperature increase causes faster kinetics and may increase the rate of oxidative fuel dissolution, which should be considered if radionuclide release occurs under oxidizing conditions. As discussed above, a temperature increase causes also faster kinetics for interfacial reactions involving H_2, i.e., reduction of U(VI) and other oxidized nuclides.

5.9 Estimated range of corrosion rate for Zircaloy and stainless steel from the spent fuel assemblies

A congruent release of the inventory of radionuclides in Zircaloy will be considered for safety assessment calculations (see also section 4.7 for the IRF of ^{14}C). The corrosion rates for Zircaloy corrosion derived by Nagra (2023c) are 6 nm/yr (reference), 10 nm/yr (upper bound), and 2 nm/yr (lower bound).

For the stainless steel parts of the fuel assemblies, the corrosion rates are even lower amounting in 0.4 nm/yr (reference), 1 nm/yr (upper bound), 0.2 nm/yr (lower bound) according to Nagra (2023c). The activity of the inventory of the Zircaloy and the stainless is part of the MIRAM-RBG Database (Nagra 2023a).

6 Natural analogues of UO_2 spent nuclear fuel

6.1 Introduction

Natural analogues can provide important information on the long-term stability of UO_2 spent fuel, particularly on its resistance against radiolytic oxidation. This information is complementary to that obtained from laboratory experiments, as the study of analogues is the only mean to obtain data that might give clues on spent fuel dissolution over geological timescales. Nevertheless, it should be remembered that the analogy is always limited, as the geochemical conditions leading to formation and alteration of uranium deposits and the materials involved always differ from those of a man-made engineered repository.

The best analogues of spent fuel to be disposed of in underground repositories are without doubt sedimentary uranium ore deposits formed under reducing conditions that have not suffered later overprinting at high p, T conditions. This includes mild diagenesis but excludes metamorphic events. Ideal candidates are those deposits that experienced temperatures not exceeding, say, 150 °C, which is about the upper limit in the expected evolution of the Swiss SF/HLW repository.

The so far best studied uranium ore matching the aforementioned criteria is probably the "Cigar Lake" deposit in Canada. Other analogues of interest discussed below are the Oklo natural reactor in the Franceville province (Gabon) and the uraniferous placer gold deposits in South Africa (Witwatersrand type). These three cases have been selected for an in-depth analysis (Sections 6.4, 6.5 and 6.6).

Natural uranium deposits are not perfect replicas of spent fuel under repository conditions. Specifically, except in the unique case of the Oklo natural reactor, they lack the presence of fission products and noble metal inclusions (ε-particles), which play a major role in catalyzing the surface-mediated suppression of radiolytic oxidation via activated H_2. Moreover, the large amounts of metals in close vicinity to UO_2 provided by a steel or copper-coated steel canister, ensuring strictly anoxic conditions and abundant H_2 production for long time spans, were not present in natural U deposits. Consequently, natural uraninites are usually to some extent hyperstoichiometric. These differing features have however, also a positive side, as they increase the conservatism of conclusions that might be drawn from the study of natural U deposits. If one can prove that H_2 was protecting natural uraninite from oxidative dissolution even in the absence of ε-particles and massive metal containers, the same conclusion could be drawn *a fortiori* for spent fuel under repository conditions.

There are two further important differences between the selected natural analogues and a spent fuel repository:

(i) All the analogues are Precambrian and have thus an age exceeding by three orders of magnitude the time required by the regulations for safety assessment calculations (1 Ma). In the Oklo natural reactor, all dose-relevant radionuclides have completely decayed and their fate must be deduced indirectly by studying their stable isotopes or (in the case of minor actinides) the final decay products. The Precambrian age of spent fuel natural analogues also leads to long-term phenomena that may be negligible during the much shorter evolution of the repository, e.g. radiogenic Pb loss and its re-precipitation. Moreover, metamictization (i.e. conversion from a crystalline to amorphous structure) is also typical of Precambrian UO_2 due to the prolonged cumulative radiation damage (Ewing & Haaker 1980, Wu et al. 2021).

(ii) The bulk geochemistry of natural analogues differs markedly from that of a repository with large amounts of engineered barrier materials (Fe, Cu, clays, cement). Typically, uranium ore deposits are rich in sulphides and contain elements in high concentrations that are absent or minor in a radioactive waste repository (e.g. Mn, Co, Ni, Cu, Zn, Pb, P, V, As) implying that the aqueous and alteration chemistry may differ considerably in the two environments.

In all the aforementioned analogues, uraninite (cubic fcc UO_{2+x}) is the main primary phase, as in the case of spent UO_2 and MOX fuels. Two main questions related to the long-term stability and dissolution rates of spent fuel under repository conditions may be addressed through the study of natural analogues:

(I) How extensive was aqueous alteration of primary uraninite in the U ore deposits under reducing conditions, particularly with respect to their replacement by U(IV) silicates (mainly coffinite)?

(II) How resistant was the primary UO_2 against radiolysis-induced or external[8] oxidative dissolution? Can any protective mechanism be inferred from the available data?

These two questions are addressed below with the help of geochemical data gained from the study of the three natural analogues (Cigar Lake, Oklo and Witwatersrand) after a brief general introduction to the mineralogy of uranium deposits and to the role of "coffinitization".

6.2 Mineralogy of uranium ores

Despite the genetic diversity of uranium ore deposits, which may be of volcanic, magmatic or sedimentary origin, the main exploited mineral is always uraninite, cubic UO_{2+x} with a fluorite structure, including the botryoidal variety known under the miner term "pitchblende" (from the German "Pechblende"). Natural uraninites are always to some degree hyper-stoichiometric, with $0 < x \leq 0.3$ (Lumpkin & Geissler-Wierwille 2020), the value of x reflecting the degree of oxidation. Due to the Precambrian age of most exploited U ores, a significant fraction of the original uranium has decayed to Pb, which is then exsolved and frequently re-precipitated *in situ* as galena, PbS, owing to the incompatibility of lead with the UO_2 lattice. Under reducing conditions, the most widespread alteration product of uraninite is coffinite, $USiO_4*nH_2O$. As conditions become more and more oxidizing, e.g. due to prolonged leaching with O_2-bearing fluids, U(IV) is destabilized and a number of U(VI) solids may form as alteration products. Under acidic conditions, the mixed-valent U-compound ianthinite, $U^{IV}_2(U^{VI}O_2)_4O_6(OH)_4*9H_2O$, schoepite $(U^{VI}O_2)_4O(OH)_6*6H_2O$ and metal-bearing uranyl oxyhydroxides may precipitate, with generic formula $M_n[(U^{VI}O_2)_xO_y(OH)_z](H_2O)_m$ with M= Ca, Sr, Ba, Pb and K (Lumpkin & Geissler-Wierwille 2020). At basic pH-values and sufficient silica concentrations uranyl silicates precipitate, such as soddyite $(U^{VI}O_2)_2SiO_4(H_2O)_2$, uranophane group minerals, $M^{n+}[(U^{VI}O_2)(SiO_4OH)]_n(H_2O)_m$, and weekesite group minerals, $M(U^{VI}O_2)_2(Si_5O_{13})(H_2O)_4$. Other minerals with complex stoichiometry may precipitate in chemically complex environments rich in transition metals and anion-forming non-metals such as S, P, V or As. Such environments are common in ore deposits, which by definition are anomalous concentrations of elsewhere minor elements.

[8] By external, we mean oxidative dissolution of UO_2 by reaction with aqueous solutions containing significant amounts of native dissolved O_2.

6.3 Coffinitization

The geochemical calculations discussed in Section 3.7.3 predict that coffinite (ideal formula: $USiO_4 \cdot nH_2O$, isostructural with zircon) should be more stable than amorphous (hydrous) UO_2 after reaction with silica-bearing bentonite pore water. These results are based on a coffinite solubility product derived from estimated, internally consistent thermodynamic data (p. 307 ff. in Grenthe et al. 2020), not on the alternative data derived by Guo et al. (2015) and Szenknect et al. (2016) which, according to Grenthe et al. (2020), are not internally consistent.

Whether or not coffinite will be the most stable U(IV) solid under repository conditions is however a still unresolved question. Although Szenknect et al. (2020) proved that it is possible to precipitate coffinite during alteration of UO_2 in silica-rich solutions at 25 °C, it is, in general, difficult to synthesize this mineral at low temperatures. Moreover, the experiments of Szenknect et al. (2020) were carried out under anoxic, but still relatively oxidizing conditions (final Eh ≈ - 70 mV); therefore, they could not demonstrate that coffinite is more stable than UO_2 under the strongly reducing conditions expected in the repository after canister failure.

The geological record shows that coffinite is widespread in natural low-temperature environments, albeit mostly in limited amounts partially replacing natural uraninite (UO_{2+x}). Coffinite is abundant in the Grants uranium district (New Mexico), where it occurs as a major U mineral in association with organic matter (Moench 1962, Deditius et al. 2008). Three different generations of coffinite were distinguished in these deposits, all formed either through direct precipitation during reduction of U(VI)-rich fluids, or through recrystallization of previously formed coffinite. As in the case of Szenknect et al. (2020) experiments, these observations do not demonstrate the thermodynamic stability of coffinite towards UO_2, since coffinite was in this case not a product of UO_2 alteration, but the result of direct precipitation from U(VI) rich fluids.

Replacement of UO_{2+x} by coffinite, indicating true destabilization of the primary uranium oxide, is frequently observed in other uranium ores, e.g. at the Port Radium mine, Canada (Wang & Xu 1999), as well as at the Oklo natural reactor in Gabon and at Jachimov mine, Czech republic (Janeczek & Ewing, 1995). Nevertheless, the opposite process (conversion of coffinite to uraninite) is also observed in some cases (Janeczek & Ewing, 1992). This dual behaviour may be explained by the dependency of the UO_2-coffinite equilibrium on redox conditions:

$$UO_2 + Si(OH)_4(aq) \Rightarrow USiO_4 + 2\ H_2O \quad (6.1)$$

$$UO_{2+x} + Si(OH)_4(aq) \Leftrightarrow USiO_4 + 2\ H_2O + x/2\ O_2(g) \quad (6.2)$$

Under strictly anoxic conditions (Reaction 6.1), either stoichiometric UO_2 ($x = 0$) or coffinite is stable at a given temperature and pressure. The reaction arrow pointing to the right corresponds to the calculation presented in Tab. 3-9, which predicts coffinite to be more stable than stoichiometric UO_2 at the silicic acid activity fixed by quartz equilibrium in bentonite pore water. In contrast, the more general Reaction 6.2, involving hyper-stoichiometric UO_{2+x} ($x > 0$), may proceed in both directions depending on redox conditions. At sufficiently high oxygen partial pressure the reaction would proceed to the left, leading to coffinite dissolution and formation of hyper-stoichiometric uranium oxide (up to a limiting value of *x* beyond which U(IV) is completely destabilized).

As already mentioned, an important outcome of the available uranium ore literature is that uraninite replacement by coffinite is always partial, in spite of the great age of the ores (mostly Precambrian). Only a small fraction of the primary UO_2 is usually converted to coffinite during alteration with Si-bearing fluids, suggesting that the complete transformation of spent fuel during repository evolution is an unlikely process. The small degrees of "coffinitization" may be tentatively explained by the low UO_2 dissolution rates under reducing conditions, rather than by

a limited availability of dissolved silica. In silicic rock environments at near-neutral pH values, silica concentrations are usually fixed in the range 10^{-4} - 10^{-3} M by equilibrium with SiO_2 phases (quartz, chalcedony, amorphous silica), which is several orders of magnitude higher than dissolved uranium concentrations. If conditions remain reducing, the only source of U available for coffinitization is the primary U(IV)O_2, which however generates dissolved concentrations only in the nanomolar level. Therefore, even if supersaturated and rich in silica, such solutions can produce coffinite only at very low rates. It is then the availability of U, not of Si, that determines coffinite production rates. As observed in the Grant district ores, large amounts of coffinite can only be generated when primary UO_2 is mobilized as U(VI) through oxidative dissolution in Si-rich environments and then reprecipitated in a reducing environment.

A simple calculation illustrates this point. We assume that a block of 0.1 m^3 UO_2(am) is in contact with a saturated solution ([U] = 3×10^{-9} M) filling an inert medium with 50% porosity. At 1 cm distance secondary coffinite precipitates, fixing the U concentration at a lower value owing to its larger stability ([U] = 8.9×10^{-10} M, see Tab. 3-9). The rate of UO_2 to coffinite conversion is assumed to be limited by the steady state diffusive flux set by the concentration gradient between the two uranium equilibrium concentrations (which is linear for 1D diffusion). The block initially contains 4063 moles of UO_2. It can be calculated from the Fick's 1st law that 150'000 years would be required to convert just 1 mol of UO_2 into coffinite under such conditions. This corresponds to a fractional UO_2 dissolution rate of 1.64×10^{-9} a^{-1}. This simple calculation shows that, due to the very low and only slightly different solubilities of the two compounds, the mass fluxes for the replacement of UO_2 to coffinite will be so small that even geological time scales are not sufficient for a complete conversion. This scoping calculation can be extrapolated to the case of spent UO_2 fuel in the Swiss repository, as similar U concentration gradients would be established when coffinite starts to precipitate at the expense of the dissolving UO_2 spent fuel matrix.

In some cases, coffinite is not detected despite seemingly favourable conditions for its formation. At Poços de Caldas, the U(VI) dissolved in sulphate-rich groundwater was re-precipitated as "pitchblende" (hydrous UO_2) at the reducing side of the redox front, together with secondary pyrite (Waber et al. 1990). The formation of pyrite was explained by present-day populations of sulphate-reducing bacteria near the redox fronts (West et al. 1990). Apparently, no coffinite was formed despite the quite high Si concentrations in the present-day groundwaters (8 – 54 mg/L, see Table 3.4 in Chapman et al.1990). This may be related to the comparatively oxidizing conditions even in the most reduced "hypogene" zone of the ore, as testified by the quoted stoichiometries of U oxides ($UO_{2.25}$ to U_3O_7, see p.22 in Chapman et al. 1990). Under such conditions, uraninite becomes hyper-stoichiometric and more stable than coffinite (i.e. Reaction 6.2 would proceed to the left).

6.4 Cigar Lake deposit

The best-studied natural analogue for long-term spent fuel behaviour under repository conditions is the hydrothermal Cigar Lake deposit. It is a 1.3 Ga old, massive high-grade uranium ore located in Northern Saskatchewan (Canada) and one of the largest uranium deposits worldwide. Precipitation of U(IV) minerals (mainly uraninite, pitchblende and small amounts of coffinite) occurred at the interface between Precambrian graphite-rich metapelites and porous overlying sandstones as U(VI)-rich hydrothermal solutions percolating through the permeable sandstones reacted with the graphite (Cramer & Smellie 1994, Smellie & Karlsson 1996). Intense hydrothermal activity altered the surrounding formations, giving rise to Fe(III)-oxide bearing illitic clay layers. The geological setting of the ore is shown schematically in Fig. 6-1.

Bruno & Spahiu (2014) summarised the geochemical evidence collected at the Cigar Lake and drew important conclusions relevant to radioactive waste disposal. The most striking observation is that the uranium oxide ore remained essentially in its original reduced state in spite of a prolonged hydrothermal activity persisting for millions of years and calculations indicating that

radiolytic oxidation would have dissolved all uranium in about 100 million years (Christensen 1994). Surface oxidation and uranium remobilization remained negligible however in spite of the undoubtedly strong alpha radiolysis induced by the high abundance of ^{235}U in Precambrian times. Significant concentrations of dissolved hydrogen (about 8×10^{-4} M) were detected by chemical analyses of present-day ground water permeating the uranium ore, suggesting that it had a protective effect preventing radiolytic oxidation. The present-day U concentrations are in the order of 3×10^{-8} M to 1×10^{-7} M, indicating equilibrium with slightly oxidized UO_{2+x}.

Given the lack of U remobilization and the low degree of UO_2 oxidation, the Fe(III) minerals disseminated in the clay surrounding the ore (mainly haematite) were first thought to arise from reaction of Fe(II)-rich ground water with the radiolytic oxidants produced by the U(IV) minerals. It was postulated that dissolved Fe(II) would consume the radiolytic oxidants, thereby preventing the oxidation of UO_2. However, this model had to be discarded since mass balance calculations based on radiolysis rates inferred from the observed H_2 always predicted a large excess of radiolytic oxidants: the amounts of Fe(III) minerals observed are by far insufficient to explain the stability of the UO_2 ore body. Alternative models, based on pyrite oxidation or a reduced effectiveness of alpha doses to water due to grain size effects,[9] also came to the same conclusion, predicting an excess of radiolytic oxidants as well.

Therefore, Bruno & Spahiu (2014) proposed an alternative explanation for the absence of oxidation in the Cigar lake uranium ore. It relies on the cumulative effect of the following two factors:

(I) *Low efficiency of water radiolysis reactions at solid-water interfaces*: Reaction yields (G-values) used in radiolysis models are usually derived from experiments with direct irradiation of homogeneous aqueous solutions. Bruno & Spahiu (2014) argue that G-values are smaller when the solution is irradiated from a solid surface. The main evidence for this argument comes from experimental evidence. In tests conducted under anoxic conditions with solutions containing UO_2, the amount of oxidized U(VI) produced was much less than expected based on G-values obtained from He ions bombardment in homogeneous solution (see Section 5.5 on threshold of alpha activity).

(II) *Recombination reactions of radiolytic oxidants*: Bruno & Spahiu (2014) argue that, in spite of the absence of catalysing ε-particles, recombination reactions involving activated hydrogen such as $H_2O_2 + H_2(aq) \Rightarrow H_2O + OH^-$ may have taken place at Cigar Lake via chain reactions mediated by the UO_2 surface. In tests with ^{233}U-enriched UO_2 (simulating the high dose rates of young spent fuel) such non-catalysed recombination reactions are not detected because they are masked by the large excess of radiolytic oxidants. Some (not yet conclusive) evidence for such a process comes from experiments on noble metal free UO_2 combined with modelling (Wren et al. 2005, see also Badley & Shoesmith 2022).

Bruno & Spahiu (2014) conclude that "*the long-term stability of the UO_2 matrix ... is warranted by the recombination of the radiolytically generated oxidants and reductants*".

[9] I.e. assuming that only a fraction of the alpha radiation produced within the uraninite/pitchblende grains would reach the water depending on particle size. In large particles, a larger fraction of the emitted alpha radiation is absorbed within the solid. In this case, water radiolysis would be weaker, reducing the required amounts of Fe(III) minerals or oxidised pyrite needed to explain the lack of UO_2 oxidation.

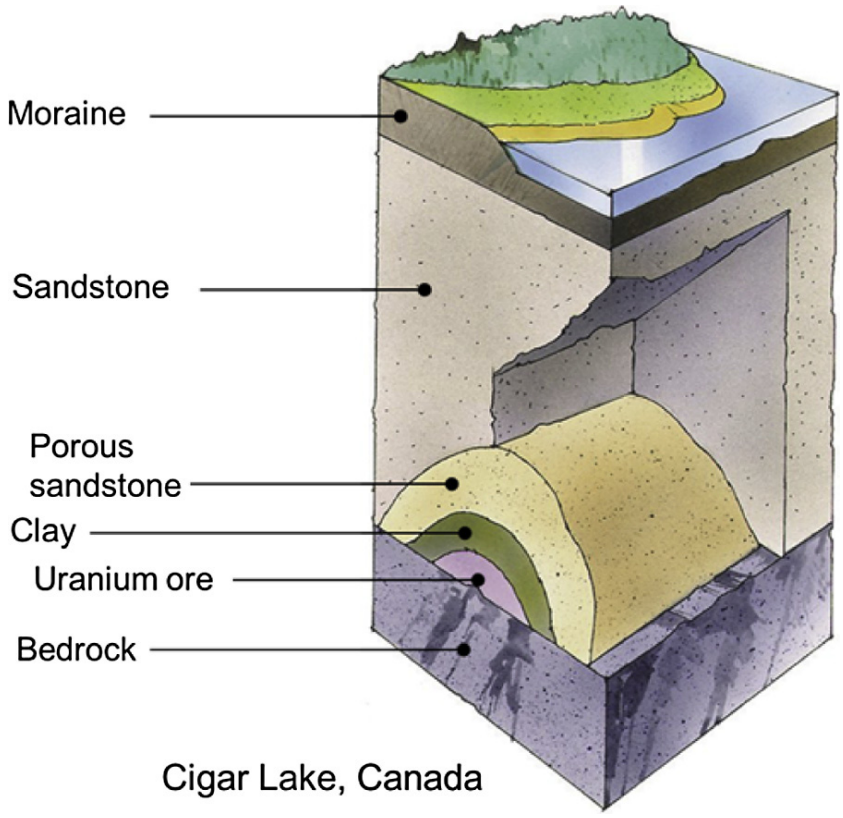

Fig. 6-1: Sketch showing the geological setting of the Cigar Lake uranium ore
Reproduced from Bruno & Spahiu (2014) with permission from the publisher

6.5 The Oklo natural reactor

Because of the time-dependent evolution of the isotopic composition of uranium in Earth history, criticality was a realistic possibility in Precambrian uraninite deposits, as natural concentrations of fissionable ^{235}U exceeded 3% at that time. Indeed, several natural fission reactors have been identified in the high-grade uranium ores of the palaeoproterozoic Franceville basin in Gabon (Lumpkin & Geisler-Wierwille 2020). The first and best-studied of these was discovered in the early seventies of the past century in the Oklo uranium mine, based on anomalously low present-day ^{235}U contents[10] and isotopic Nd-signatures typical of spent UO_2 fuels (Neuilly et al. 1972).

The uranium ore deposits of the Franceville basin are about 2 Ga old and formed through reduction of U(VI) bearing fluids (percolating through permeable sandstones and conglomerates) by hydrocarbon-rich sediments (Gauthier-Lafaye et al. 1996). The U ore is mainly composed of uraninite in direct contact with organic matter filling the porosity of the sandstones and has a grade varying from 0.1% to 10 – 20%. It is always associated with calcite and sulphide-bearing fractures. Criticality was reached in regions of highest U enrichment and open porosity. In this environment the pore water acted as moderator (thermalisation of neutrons). Temperatures during diagenesis apparently never exceeded 200 °C at moderate pressures (~ 300 bar), thus preserving

[10] The present-day deficiency of ^{235}U is a signature of the "burning" of this fissile isotope through the fission reaction, which is localized in the core of the natural reactors. In some locations outside the core, however, slight enrichment of ^{235}U w.r. to present-day abundance was observed (Neully et al. 1972). This was interpreted as the result of ^{239}Pu breeding (via neutron capture by ^{238}U) followed by its migration in the altered zone and subsequent decay to ^{235}U.

fairly well the geochemical conditions of the reactor. Large scale remobilization and dispersion of fission products did not occur. Nevertheless, fluid inclusion studies in quartz overgrowths revealed locally higher temperatures (up to 500 °C) in regions directly affected by the fission reaction.

The first studies mainly focussed on the determination of the "operating conditions" of the natural reactors. Later studies were more concerned with issues related to the geochemical features of the reactors and the post-criticality dispersion of actinides and fission products. According to Gauthier-Lafaye et al. (1996) following the thermal pulse induced by the nuclear reaction, a hydrothermally altered zone rich in clay minerals, phosphates (apatite) and (Fe-)-oxyhydroxides formed around the reactor cores. These secondary minerals replace most of the quartz building up the original sandstones.

Most important for the questions addressed in this chapter are the observations related to the uranium ore minerals. Within the reactor zones, which represent the spent fuel analogue, uraninite remains the dominating phase along with minor coffinite (Gauthier-Lafaye et al. 1996), forming massive bodies with up to 80% UO_2. The environmental conditions remained reducing most of the time thanks to the large amounts of associated hydrocarbons. In other words, the organic matter takes the "role" of the metallic canister in the chemical analogy. However, the microscopic-petrographic analyses reveal a complex history, with repeated fracturing, reprecipitation and partial dissolution of the uraninite grains after the ore formation and the fission reactions, and uraninites have hyperstoichiometry coefficients ranging from 0.00 to 0.25 (Eberly et al. 1994). Nevertheless, the fact that the uraninite remained mostly preserved over almost 2 Ga, in spite of the well-documented tectonic and hydrothermal activity, is a proof that extensive radiolytic oxidation of UO_2 leading to massive UO_2 dissolution and re-precipitation as U(VI) minerals could not take place.

Dubessy et al. (1988) investigated fluid inclusions within and outside the reactor zones at Oklo. In the reactor zones, they detected H_2-rich fluid inclusions coexisting with O_2. The H_2 was interpreted to be possibly a product of water radiolysis. Combined with the good preservation of uraninite, this evidence suggests that the produced radiolytic H_2 was chemically activated and protected the UO_2 from oxidation. Coffinitization was in general minor, except for the Bangombé reactor, where coffinite locally replaces the uraninite pervasively (Gauthier-Lafaye et al. 1996). Among the various natural reactors, this is the one located closest to the surface and thus subject to recent highly oxidizing weathering.

Contrary to other uranium ores, the Oklo natural reactor provides more similarities to LWR spent fuel and its disposal, especially the production of fission products and minor actinides. This led for instance to the detection of noble metal particles in the reactor core zone (Utsunomiya & Ewing 2006) that bear strong similarities with the well-known ε-particles in LWR fuels, known to catalyse the chemical activation of H_2 and thus enhance its protective effect against radiolytic oxidation of the fuel (see Chapter 5).

Natural reactors also provide a means of studying the mobility of fission products generated by the nuclear reaction. Although most of the long-lived dose-relevant radionuclides have decayed[11] (including ^{129}I, half-life = 1.61E7 a), the process can be traced back using stable isotopes of the same elements or stable daughter isotopes. Several relevant studies have been conducted (see Hidaka 2020 and references therein). Radiogenic Pb from U decay is also a useful element as it mimics the behaviour of elements incompatible with the UO_2 lattice structure. Pb/U isotopic ratios measured in uraninite grains give insight on the extent of Pb loss and the age(s) of such events, which are mostly episodic. It turns out that a major loss of Pb occurred in conjunction with the magmatic intrusion of dolerite 850 Ma ago. Typically, Pb was expelled from the UO_2 structure

[11] The age of the reactor is about 2E9 a, i.e. a period 2'000 times longer than required for safety assessment calculations. In this time, even ^{129}I (half-life = 1.61E7 a) will have decayed completely.

and re-precipitated almost in-situ as galena, PbS. Fig. 6-2, which was taken on a sample from the reactor with the lowest Pb/U ratios and thus highest Pb loss, shows such a mobilization pattern: the central part of the UO_2 grain (primary UO_2) has apparently lost all radiogenic Pb, which re-precipitated as tiny inclusions in newly formed UO_2. The image shows that recrystallization of UO_2, a process postulated in Bradbury et al. 2014, is a realistic process, at least at the elevated temperatures (up to 500 °C) characterizing the Oklo environment.

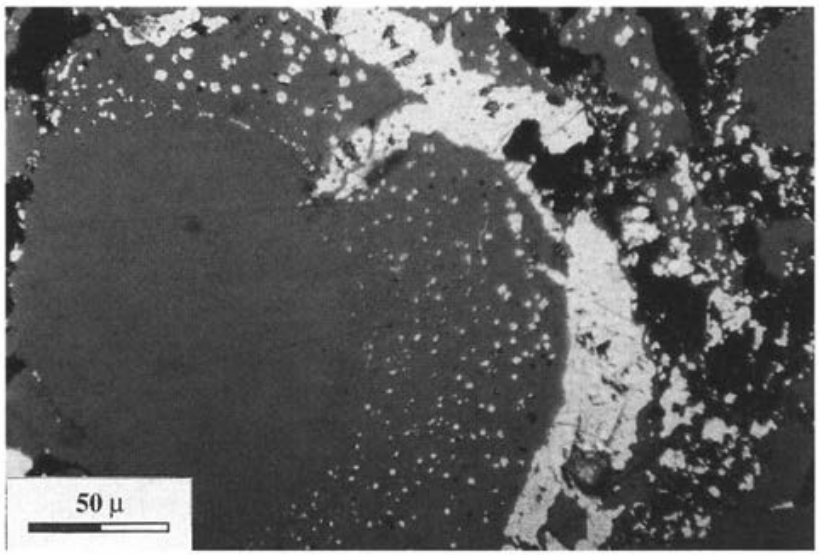

Fig. 6-2: Reflected light image of a composite uraninite grain (dark grey) from Oklo's Reactor 13, showing expulsion of radiogenic Pb and its re-precipitation as galena inclusions inside recrystallized UO_2 (white spots) and outside of it (white patches)

The central uniform dark grey region devoid of galena is probably primary uraninite, from which all the Pb has been expelled (from Gauthier-Lafaye et al. (1996), reprinted with permission from the publisher).

In spite of the preservation of large fractions of primary uraninite, the study of fission products and their stable decay products revealed extensive mobilization, which was however only partial and differed among chemical groups of chemical elements. In an isotopic study of the reactor zones RZ 10 and RZ 13 in the Oklo natural analogue (Hidaka & Holliger 1998), all fissiogenic rare earth elements were found to be well retained in the uranium matrices of the corresponding reactor zones (more than 90%), while less than 20% of fissiogenic alkalis and alkaline earth were retained (e.g. Cs, Sr). The calculated fission product yield curves and the measured data coincide very well for all rare earth elements (see their Fig. 7). This same isotopic study of the sulphide corroded metal particle residues in the Oklo reactor zones RZ-10 and RZ-13 (Hidaka & Holliger 1998) indicates that ^{99}Tc was incorporated in the metallic particles during its decay ($t_{1/2}$ 2.13 × 10^5 y) to ^{99}Ru, because the isotopic ratio $^{99}Ru/^{101}Ru$ in the metallic particles was more than two times higher than that of the surrounding rock. It also shows that samples from RZ 10 and RZ 13 retained more than 90% of the fissiogenic Ru, Rh, Pd and Te. In contrast to REEs, fission gases and volatile radionuclides such as iodine were quantitatively expelled, and also the major part of the fissiogenic Rb, Sr, Ba, Cs, Mo and Ag were removed (Gauthier-Lafaye et al. 1996) and partly reprecipitated in secondary phases such as apatite and illite.

It is however not possible to extrapolate these finding to the behaviour in the Swiss repository, as there are important differences between the two environments. Specifically, the almost total loss of some fission products observed at Oklo can be explained by:

(a) the more extensive radiation damage of the uraninite lattice due to the much longer ageing time, compared to the time required for the complete decay of dose-relevant nuclides in the Swiss repository

(b) the hydrothermal alteration at higher temperatures than those in the planned Swiss repository near-field after canister failure

In summary, the Oklo analogue provides evidence for the long-term stability of UO_2 even in the absence of a metallic buffer system and after repeated thermal/tectonic events. Specifically, coffinitization was very limited and there are indications that the H_2 produced by radiolysis was sufficient to protect uraninite from extensive oxidative dissolution. The protection will be more effective under the more reducing and more H_2-rich conditions expected in the Swiss HLW/SF repository. In contrast, the results concerning fission product mobilization are hardly transferable to the Swiss repository, due to the more advanced radiation damage in the UO_2 structure and high hydrothermal alteration temperatures experienced by the Oklo natural reactors.

6.6 Witwatersrand Au-U placer deposits

Precambrian placer Au-U deposits (Armstrong 1981) provide further evidence for the long-term stability of UO_2. These deposits are exploited as a major source of gold and originated through erosion, transport and deposition of gold and other primary minerals, forming sands and conglomerates, at times where the atmosphere was CO_2-rich and almost anoxic. The outstanding examples are the Witwatersrand uranium-bearing quartz-pebble conglomerates. They contain abundant detrital uraninite and pyrite grains that must have been exposed to the O_2-deficient Precambrian atmosphere. For such grains to survive fluvial transport along hundreds/thousands of kilometers, oxygen partial pressures must have necessarily been far below today's levels. The occurrence of such deposits is therefore taken as major evidence that the Earth's atmosphere was essentially anoxic before about 2'000 Ma (Grandstaff 1976 & 1980).

Attempts were made to correlate the resistance of uraninite to chemical oxidation and physical transport during their genesis as a function of pO_2, carbonate concentration and pH. Such models (Grandstaff 1976 & 1980, Johnson et al. 2014) are empirical and require a number of hardly verifiable assumptions. In spite of these limitations, the main conclusion from such model calculations is that the uraninite particles could withstand exposure to pO_2 of up to 10^{-7} bar for several hundred thousand years at carbon dioxide partial pressures of 10^{-1} bar, at a time where the ^{235}U natural isotope abundance was comparable to that in enriched uranium used in nuclear power reactors (about 3%)[12]. Under present-day pCO_2 conditions, this estimate increases to $pO_2 = 10^{-5}$ bar.

The mere fact that such old uraninite grains survived in-situ for such long time spans until the present is a strong (though indirect) indication for the existence of powerful mechanisms protecting the UO_2 surface from radiolytic oxidation. It may be argued that the same recombination reactions identified as the possible reason for the long-term stability of the Cigar lake ore were operating also during and after the diagenesis of the placer deposits.

[12] The alpha irradiation rate from pre-Cambrian natural uranium was thus higher than for modern natural uranium, however still much weaker than the irradiation from spent fuel at the expected failure times.

6.7 Conclusions from natural analogues

As discussed above, the study of uraninite deposits and of the natural reactor discovered at Oklo (Gabon) provide important information on the long-term stability of UO_2 spent fuel under repository conditions.

Perhaps the most important result is the evidence of UO_2 resistance against radiolytic oxidation. The Cigar lake uraninite ore remained essentially in its original reduced state in spite of strong alpha radiolysis and a prolonged hydrothermal activity persisting for millions of years. Bruno & Spahiu (2014) conclude that "*the long-term stability of the UO_2 matrix ... is warranted by the recombination of the radiolytically generated oxidants and reductants*".

The Oklo analogue provides evidence for the long-term stability of UO_2 and limited radionuclide release even in the absence of a metallic redox buffer system and in spite of repeated thermal/tectonic events. There are indications that the H_2 produced by radiolysis was sufficient to protect uraninite from extensive oxidative dissolution. The protection will be more effective under the more reducing and more H_2-rich conditions expected in the Swiss HLW/SF repository.

In this line of argument, also the integrity of the uraninite grains in the Witwatersand Au-U placer deposits is a strong (though indirect) indication of the existence of powerful mechanisms protecting the UO_2 surface from radiolytic oxidation.

The observations from natural analogues are complementary to the data obtained from laboratory experiments, as they give clues on spent fuel dissolution over geological timescales, although it should be remembered that the analogy is always limited due to the different conditions in a geological environment compared to a spent fuel repository as discussed above.

Therefore, in line with the conclusion derived in chapter 5 of this report, observations from natural analogues are in support of the low spent fuel dissolution rates selected for use in safety assessment calculations (see Chapter 7).

7 Reference values for safety assessment

7.1 Summary of recommended IRF values for radionuclides for fuel from Swiss power reactors

The proposed IRF values of radionuclides for the Swiss reactors for the safety assessment of SGT E3 are given in Section 4.7 and summarised in Tab. 4-2. For convenience, they are provided here again (Tab. 7-1; for detailed information regarding their derivation see Chapter 4).

Tab. 7-1: Average FGR and reference and upper bound IRF (aqueous release) values (%) of radionuclides for spent fuel from the Swiss reactors

Red shading represents IRF values that are correlated with FGR (see Section 4). Blue shading indicates IRF values not correlated with FGR.

	Beznau		**Gösgen**		**Leibstadt**	**Mühleberg**
	UO_2	**MOX**	**UO_2**	**MOX**	**UO_2**	**UO_2**
FGR (avg.)	1.8	2	14	16	4	3
Cs IRF (ref.)	1.1	1.2	8	9	2.3	1.7
Cs IRF (upper bound)	2.2	2.4	16	18	4.6	3.4
^{129}I (ref.)	1.8	2	14	16	4	3
^{129}I (upper bound)	3.6	4	28	32	8	6
^{36}Cl	5.4	6	42	48	12	9
^{79}Se (ref.)	0.5	0.5	0.5	0.5	0.5	0.5
^{79}Se (upper bound)	1	1	1	1	1	1
^{14}C (ref.)	3	3	3	3	3	3
^{14}C (upper bound)	5	5	5	5	5	5
^{126}Sn	0.1	0.1	0.1	0.1	0.1	0.1
^{90}Sr (ref.)	0.05	0.05	0.05	0.05	0.05	0.05
^{90}Sr (upper bound)	0.25	0.25	0.25	0.25	0.25	0.25
^{107}Pd (ref.)	0.01	0.01	0.01	0.01	0.01	0.01
^{107}Pd (upper bound)	0.1	0.1	0.1	0.1	0.1	0.1
^{99}Tc (ref.)	0.01	0.01	0.01	0.01	0.01	0.01
^{99}Tc upper bound)	0.1	0.1	0.1	0.1	0.1	0.1

Instant release fraction (IRF) for ^{14}C from Zircaloy (see Section 4.7) are 0.01% (reference), 0.1% (upper bound) and 0.001% (lower bound).

7.2 Estimated range of dissolution rate of spent fuel for safety assessment

A summary of the studies performed to derive the dissolution rate of spent fuel is given in Chapter 5 and rates are derived and justified in Chapter 5.8.

The low fractional dissolution rates recommended to be used in safety assessment is based on multiple arguments, including:

- Conditions in the repository will ensure that H_2 concentrations in pore water will remain high for hundreds of thousands of years after containment failure.
- Catalytic activation of H_2 at the surface of ϵ-particles in the spent fuel will prevent U(IV) oxidation and maintain the reduced state of the fuel surface at a composition close to $UO_{2.00}$.
- Spent fuel dissolution experiments in solutions purged with H_2 under strictly anoxic conditions yield decreasing aqueous concentrations of uranium over periods of months, eventually reaching the solubility of UO_2 (am). This is followed by immeasurably low release rates.
- Similar results are reported from studies of fuel leaching in the presence of metallic Fe in an initially Ar atmosphere, where H_2 and Fe(II) are produced *in situ* by Fe corrosion.
- Dissolution rates of alpha-doped UO_2 (with alpha doses representative of aged spent fuel) in reducing solutions, combined with radiation chemistry experiments, yield low dissolution rates.
- Experimental findings from the DISCO project indicate that the dissolution rates of non-conventional UO_2 fuels (Cr-doped, MOX) are in the same range as for standard UO_2 fuel.
- Natural analogue studies show that uraninite remains stable over geologic time frames.
- Upper limit of experimental and analytical uncertainties in fuel dissolution measurements allow to set the selected maximum rate.
- The results of advanced models using experimentally determined interfacial reaction rates for fuel dissolution under reducing conditions, support the very low experimentally determined rates, at the same time clarifying the nature of reaction mechanisms on the fuel surface.

Based on these arguments, the spent fuel dissolution rate proposed for use in safety assessment calculations is given in Tab. 7-2.

Tab. 7-2: Spent fuel dissolution rates for safety assessment calculations

	Fractional dissolution rate [a^{-1}]
Reference rate	**10^{-7}**
Upper limit	10^{-6}
Lower limit	10^{-8}

7.3 Corrosion rates for Zircaloy and stainless steels

The corrosion rates for Zircaloy and the stainless-steel parts of the fuel assemblies as defined in Section 5.9 are summarised in Table 7-3.

Tab. 7-3: Corrosion rates for safety assessment calculations

(Nagra 2023c)

	Zircaloy corrosion rates [nm/a]	**Stainless steel parts of SF assemblies** [nm/a]
Reference rate	**6**	**0.4**
Upper bound	10	1
Lower bound	2	0.2

Assuming a cladding thickness of ~ 600[13] µm and corrosion from both sides the radionuclide release rates from Zircaloy are accordingly

Reference: $6\ \text{nm a}^{-1} \ / \ 3 \times 10^5\ \text{nm} = 2.0 \times 10^{-5}\ \text{a}^{-1}$

Upper bound: $10\ \text{nm a}^{-1} \ / \ 3 \times 10^5\ \text{nm} = 3.3 \times 10^{-5}\ \text{a}^{-1}$

Lower bound: $2\ \text{nm a}^{-1} \ / \ 3 \times 10^5\ \text{nm} = 6.7 \times 10^{-6}\ \text{a}^{-1}$

[13] The minimum cladding thickness of the spent fuel assemblies used in the Swiss reactor corresponds to 600 µm according to SF Compos and according to Adolfson et al. (2010).

8 References

Adolfsson, Y., Bäckström, O. & Zander, K. (2010):. Säkerhetsredovisning för drift av slutförvarsanläggning för använt kärnbränsle (SR-Drift) kapitel 8 - Säkerhetsanalys. SKB Report No. 2006114-R-006. June 2010.

Aitchison, I. & P.H. Davies. Role of microsegregation in fracture of cold-worked Zr2.5Nb pressure tubes. (1993): J. Nucl. Mater. 203, 206-220.

Albinsson, Y., Jensen, A.Ö., Oversby, V.M.M. & Werme, L.O. (2003): Leaching of spent fuel under anaerobic and reducing conditions, MRS Symp. Proc. 757, 407-413 (2003).

Arborelius, J., Bachman, K, Hallstadius, L. et al. (2006): Advanced doped UO2 pellets in LWR applications. J. Nuc. Sci. Tech. 43(9), pp. 967-976.

Areva (2010): Spaltgasfreisetzungsdaten aus dem Kernkraftwerk Gösgen für Studien zur Endlagerung abgebrannter Brennelemente. Nagra Arbeitsbericht NAB 10-32.

Areva (2012): Spaltgasfreisetzungsdaten aus dem Kernkraftwerk Beznau, Block 1 und 2 für Studien zur Endlagerung abgebrannter Brennelemente. Nagra Arbeitsbericht 12-01.

Armstrong, F.C., ed. (1981): Genesis of Uranium- and Gold-Bearing Precambrian Quartz-Pebble Conglomerates, Proceedings of Workshop, October 13-15, 1975, Golden, Colorado. Geological Survey Professional Paper 1161-A-BB. U.S. Geological Survey.

ASTM International C-776-06 (2006): Standard specification for sintered uranium dioxide pellets, September 2006.

Badley, M. & Shoesmith, D. (2022): The Corrosion/Dissolution of Used Nuclear Fuel in a Deep Geological Repository. Technical Report NWMO-TR-2022-09, Nuclear Waste Management Organization, Toronto, Canada.

Baker, F.B. & Newton, T.W. (1961): The reaction of U(IV) with hydrogen peroxide. J. Phys. Chem. 65, pp.1897-1899.

Barner, J.O. (1985): Characterization of LWR spent fuel MCC-Approved Testing Material – ATM-101 PNL-5109 (Battelle Northwest Laboratory, Rev.1.

Barreiro-Fidalgo, A., Roth, O., Puranen, A., Evins, L.Z. & Spahiu, K. (2020): Aqueous leaching of ADOPT and standard UO_2 spent nuclear fuel under H_2 atmosphere, Proc. 3rd Annual Meeting EC-project Disco, pp. 37-43.

Barreiro-Fidalgo, A., Roth, O, Evins, L.Z., & Spahiu, K. (2021): Aqueous leaching of Cr_2O_3-doped UO_2 spent nuclear under oxidizing conditions, MRS Advances 6, 103-106.

Bauhn, L., Ekberg, C., Fors, P. & Spahiu, K. (2017): The effect of bromide on oxygen yields in homogeneous α-radiolysis, MRS Advances, Energy and Sustainability, Vol. 2, Issue 13, pp.711-716.

Bauhn, L., Hansson, N., Ekberg, C., Fors, P., Delville, R. & Spahiu, K. (2018b): The interaction of molecular hydrogen with a-radiolytic oxidants on a $(U,Pu)O_2$ surface. J. Nucl. Mater. 505, pp. 54-61.

Berman, R.G., & Brown, T.H. (1984): A thermodynamic model for multicomponent melts, with application to the system CaO-A12O3-SiO2, Geochim. Cosmochim. Acta 48, 661–678.

Besmann, T.M. (2012): Computational Thermodynamics: Application to Nuclear Materials. In: Comprehensive Nuclear Materials, R.J.M. Konings, Ed., Volume 1, Ch. 1.17: Basic Aspects of Radiation Effects in Solids/Basic Aspects of Multi-Scale Modeling, 455-470, Elsevier Ltd.

Bestel, M., Glaus, M.A., Frick, S., Gimmi, Th., Jurany, F., Van Loon, L.R. & Diamond L.W. (2018): Combined tracer through-diffusion of HTO and 22Na through Na-montmorillonite with different bulk dry densities. Appl. Geochem 93, 158-166.

Blackburn P.E. (1973): Oxygen pressures over fast breeder reactor fuel (I) A model for UO2±x. J. Nucl. Mater. 46, 244-252.

Bleier, A., K.H. Neeb, R.H. Kroebel &H.W. Wiese (1987): Carbon-14 inventories and behaviour in LWR spent fuel rods during reprocessing, Societe Francaise d'Energie Nucleaire (SFEN), 75 - Paris; 391 p; 1987; p. 1089-1094; Societe Francaise d'Energie Nucleaire; Paris (France); International Conference on nuclear fuel reprocessing and waste management; Paris (France); 23-27 Aug 1987.

Bonin, B., Colin, A. & Dutfoy, A. (2000): Pressure building during early stages of gas production in a radioactive waste repository, J. Nucl. Mater., 281 p. 1-14.

Bonka, H, Brusserman, G. & Schwarz, G. (1974): Umweltbelastung durch Radiokohlenstoff aus Kerntechnikenanlagen, Reactortagung, Berlin.

Bradbury, M.H. & Baeyens, B. (1997): A mechanistic description of Ni and Zn sorption on Na montmorillonite. 2. Modelling. J. Contam. Hydrol. 27, 223-248.

Bradbury, M.H. & Baeyens, B. (2002): Porewater chemistry in compacted re-saturated MX-80 bentonite: Physico-chemical characterisation and geochemical modelling. Nagra Technical Report NTB 01-08.

Bradbury M.H., Berner U., Curti E., Hummel W., Kosakowski G. & Thoenen T. (2014): The Long Term Geochemical Evolution of the Nearfield of the HLW Repository. Nagra Technical Report NTB 12-01.

Broczkowski M.E., Keech P.G., Noel J.J. & Shoemsith D.W. (2010): Corrosion of uranium dioxide containing simulated fission products in dilute hydrogen peroxide and dissolved hydrogen. J Electrochem Soc 157 (8) C275-C281.

Broczkowski, M., Noël, J. & Shoesmith, D. (2005): The inhibiting effects of hydrogen on the corrosion of uranium dioxide under nuclear waste disposal conditions. J. Nucl. Mater. 346, pp. 16-23.

Brunauer, S., Emmett, P. & Teller, E. (1938): Adsorption of gases in multimolecular layers, J. Am. Chem. Soc. 60, pp. 309-319.

Bruno, J. & Spahiu, K. (2014): The long-term effect of hydrogen on the UO_2 spent fuel stability under anoxic conditions: Findings from the Cigar Lake Natural Analogue study. Applied Geochemistry, 49, 178-183.

Bush, R.P., Smith, G.W. & White, F. (1984): Nuclear Science and Technology, Carbon-14 Waste Management, Rep. EUR 8749, Office for Official Publications of the European Communities, Luxembourg (1984).

Capouet M., Boulanger, D., Vandoorne, T., Gaggiano, R., Norris, S., Williams, S., Schumacher, S. Rübel, A., Nummi, O., Poskas, P., Narkuniene, A., Grigaliuniene, D., Vokál, A., Mibus, J., Rosca-Bocancea, E., Hart, J., Ferrucci, B., Levizzari, R., Luce, A., Diaconu, D., Cuñado Peralta, M., Owada, H., Kienzler, B., Wieland, E., Van Loon, L. & Walker, R. (2017): Knowledge Supporting Safety Assessments of ^{14}C, EU CAST Project Report (D6.2).

Carbol, P., Cobos-Sabate, J., Glatz, J.-P., Ronchi, C., Rondinella, V., Wegen, D.H., Wiss, T., Loida, A., Metz, V., Kienzler, B., Spahiu, K., Grambow, B., Quinones, J. & Esparaza, A.M. (2005): The effect of dissolved hydrogen on the dissolution of ^{233}U doped UO_2 (s). SKB Technical Report 05-09; Swedish Nuclear Fuel and Waste Management Co.

Carbol, P., Fors, P., Gouder, T. & Spahiu, K. (2009b): Hydrogen suppresses UO_2 corrosion. Geochim. Cosmochim. Acta 73, pp. 4366-4375.

Carbol, P., Fors, P., Van Winckel, S. & Spahiu, K. (2009a): Corrosion of irradiated MOX fuel in presence of dissolved H_2. J. Nucl. Mater. 392, 45-54. https://doi.org/10.1016/j.jnucmat.2009.03.044.

Carbol, P., Wegen, D.H., Wiss, T., Fors, P., Jegou, C. & Spahiu, K. (2020): Spent nuclear fuel as waste material, in: "Comprehensive Nuclear Materials", 2nd edition, Konings R.J.M. and Stoller R.E. Editors in Chief, Elsevier, Amsterdam.

Catlow C.R.A. (1977): The thermodynamics of mixed oxide reactor fuels, J. Nucl. Mater. 67 pp. 236-238.

Cera, E., Bruno. J., Duro, L. & Eriksen, T. (2006): Experimental determination and chemical modelling of radiolytic processes at the spent fuel/water interface. Long contact time experiments, SKB Technical Report TR-06-07, Svensk Kärnbränslehantering AB.

Chapman, N.A., McKinley, I.G., Shea, M.E. & Smellie, J.A.T. (1990): The Poços de Caldas project: Summary and implications for radioactive waste management. Technical Report NTB 90-33, Nagra, Wettingen, Switzerland and TR 90-24, Swedish Nuclear Fuel and Waste Management Co (SKB), Stockholm, Sweden.

Christensen, H. (1994): Oxidation by water radiolysis products. In: Cramer, J.J., Smellie, J.A.T. (Eds.), Final Report of the AECL/SKB Cigar Lake Analog Study. AECL Tech Rep (AECL-10851), Pinawa and SKB Tech Rep TR-94-04.

Ciavatta, L., Ferri, D., Grenthe, I., Salvatore, F. & Spahiu, K. (1983): Studies on metal carbonate equilibria: 4. Reduction of the tris(carbonato)dioxouranate(VI) ion, $UO_2(CO_3)_3^{4-}$, in hydrogen carbonate solutions., Inorg. Chem., 22 pp. 2088-2092.

Clarens, F., Serrano-Purroy, D., Martínez-Esparza, A., Wegen, D., Gonzalez-Robles, E., de Pablo, J., Casas, I., Giméne,z J., Christiansen, B. & Glatz, J.-P. (2008): RN Fractional Release of High Burn-Up Fuel: Effect of HBS and estimation of accessible grain boundary, Mater. Res. Soc. Symp. Proc. 1107, pp. 439-446.

Cobos, J., Papaioannou, D., Spino, J. & Coquerelle, M. (1998) : Phase characterisation of simulated high burn-up UO_2 fuel, J. Alloys and Compounds 271-273, pp. 610-615.

Cramer, J. & Smellie, J. (1994): Final report of the AECL/SKB Cigar Lake Analog Study. SKB Report 94-04. SKB, Stockholm, Sweden.

Cui, D., Low, J., Rondinella V. & Spahiu, K. (2010): Catalytic effects of nanostructured fission-product particles at repository environment, Applied Catalysis B: Environmental 94, 173-178.

Cui, D., Low, J. & Spahiu, K. (2011): Environmental behavior of spent nuclear fuel and canister materials, Energy and Environmental Science 4, 2537.

Cui, D., Devoy, J. & Spahiu, K. (2003): The surface precipitation during the UO_2 leaching process, In: Scientific Basis for Nuclear waste management XXVI, Mat. Res. Soc. Symp. Series, vol. 757, (Finch, R. J. and Bullen, D.B. eds.), pp. 359-364.

Cui, D., Ekeroth, E., Fors, P. & Spahiu, K. (2008). Surface mediated processes in the interaction of spent fuel or α-doped UO_2 with H_2, Mat Res Soc Symp. Proc Vol. 1104, pp 87-99.

Cui, D. & Spahiu, K., (2002): The reduction of U (VI) on corroded iron under anoxic conditions, Radiochimica Acta, 90, pp. 623-628. https://doi.org/10.1524/ract.2002.90.9-11_2002.623

Cui, D., Eriksen, T, & Eklund, U.-B. (2001): On metal aggregates in spent fuel – synthesis and leaching of Mo-Ru-Pd-Rh alloy. MRS Symp. Proc. 663, 427-434.

Curti, E. & Kulik, D.A. (2020): Oxygen potential calculations for conventional and Cr-doped UO_2 fuels based on solid solution thermodynamics. J. Nucl. Mater. 534, 152140.

Curti, E. (2021): Thermodynamic modelling of "inside canister" conditions during UO_2 spent fuel dissolution in a failed steel container. Deliverable D5.6, DISCO project, grant agreement 755443, Horizon 2020 Framework Programme, European Commission.

Curti, E. (2022): Bentonite Pore Waters (BPW) for the Sectoral Plan, phase SGT-3: model development, testing and final calculations. Nagra Arbeitsbericht NAB 22-43.

Curti, E., Thoenen, T., Kosakowski, G., Miron, D., Baeyens, B., Van Loon, L.R. & Leupin, O. (2023): The chemical near-field evolution with the HLW repository. Nagra Technical Report NTB 23-02.

Curti, E., Froideval-Zumbiehl, A., Günther-Leopold, I., Martin, M., Bullemer, A., Linder, H., Borca, C.N. & Grolimund, D. (2014): Selenium redox speciation and coordination in high-burnup UO_2 fuel: Consequences for the release of ^{79}Se in a deep underground repository, Journal of Nuclear Materials 453 (2014) 98–106.

Davis, W. Jr. (1979): Carbon-14 production in nuclear reactors, in Management of Low-level Radioactive Waste, Vol. 1, Eds. M.W. Carter A.A. Moghissi and B. Kahn, Pergamon Press, New York.

de Pablo, J., Casas, I., Gimenez, J., Molera, M. Rovira, M., Duro, L. & Bruno, J. (1999): The oxidative dissolution of uranium dioxide I. The effect of temperatura in hydrogen carbonate media, Geochim. Cosmochim. Acta, 63, pp. 3097-3103.

Deditius, A.P., Utsunomiya, S. & Ewing, R.C. (2008): The chemical stability of coffinite, $USiO_4 \cdot nH_2O$; $0 < n < 2$, associated with organic matter: A case study from Grants uranium region, New Mexico, USA. Chem. Geology 251, 33-49.

Diomidis, N., Cloet, V., Leupin, O.X., Marschall, P., Poller, A. & Stein, M. (2016): Production, consumption and transport of gases in deep geological repositories according to the Swiss disposal concept. Technical Report NTB 16-03.

Dubessy, J., Pagel, M., Beny, J.M., Christensen, H., Bernard, H., Kosztolanyi, C. & Poty, B. (1988): Radiolysis evidence by H_2-O_2 and H_2-bearing fluid inclusions in three uranium deposits. Geochim. Cosmochim. Acta 52, 1155-1167.

Eberly, P., Janeczek, J. & Ewing, R. (1994): Petrographic analysis of samples from the uranium deposit at Oklo, republic of Gabon. Radiochim. Acta 66/67, 445-461.

Ekeroth, E., Granfors, M., Schild, D. & Spahiu, K. (2020): The effect of temperature and fuel surface area on spent nuclear fuel dissolution kinetics under H_2 atmosphere. J. Nucl. Mater. 531, id. 151081.

Ekeroth, E., Cui, D., Low, J., Granfors, M., Zwicky, H.U., Spahiu, K. & Zetterström Evins, L. (2012): Mater. Res. Soc. Symp. Proc., 1475 (2012) p. 125-130.

Ekeroth, E., Low, J., Zwicky, H.-U. & Spahiu, K. (2009): Corrosion studies with high burn-up LWR fuel in simulated groundwater. MRS Symp. Proc. 1124, pp. Q02-07.

Elliot, A.J., Padamshi, S. & Pika, J. (1986): Free radical redox reactions of uranium ions in sulphuric acid solutions, Canad. J. Chem. 64 pp. 314-320.

EPRI (1995): Characterization of C-14 generated by the nuclear power industry, EPRI TR-105715.

Eriksen T.E., Jonsson, M. & Merino, J. (2008): Modelling time resolved and long contact time dissolution studies of spent nuclear fuel in 10 mM carbonate solution-A comparison between two models and experimental data, J. Nucl. Mater. 375, pp. 331-339.

Evins, L.Z. & Jensen, K.A. (2012): Review of spatial relations between uraninite and coffinite - Implications for alteration mechanisms., Mater. Res. Soc. Symp. Proc. Vol. 1475, , 89-96. DOI: 10.1557/opl.2012.559.

Evins, L.Z., Valls, A. & Duro, L. eds. (2021): Deliverable D1.25, Final Conference Proceedings, DISCO project, Grant Agreement: 755443, European Commission, Bruxelles.

Ewing, R.C. & Haaker, R.F. (1980): The metamict state: implications for radiation damage in crystalline waste forms. Nuclear and Chemical Waste Management 1, 51-57.

Farrell, J., Bostick, W.D., Jarabek, R.J. & Fiedor, J.N. (1999): Uranium removal from ground water using zero valent iron media, Groundwater, 37 (1999) 618-624. https://doi.org/10.1111/j.1745-6584.1999.tb01150.x

Ferry, C., Piron, J.-P. & Ambard, A. (2010) : Effect of helium on the microstructure of spent fuel in the repository, J. Nucl. Mater. 407, p. 100-109.

Ferry, C., Piron, J.-P., Poulesquen, A. & Poinssot, C. (2008): Radionuclides release from spent fuel under disposal conditions: re-evaluation of the Instant Release Fraction, MRS Symp. Proc. 1107, pp 447-454.

Ferry, C., Poinssot, C., Broudic, V., Cappelaere, C., Desgranges, L., Garcia, P., Jegou, C., Lovera, P., Marimbeau, P., Piron, J.-P., Poulesquen, A., Roudil, D., Gras, J.-M, Bouffioux, P. (2005): Synthesis on the spent fuel long term evolution. Report CEA-R-6084, Commissariat à l´Énergie Atomique, Saclay, France.

Fidalgo, A.B., Roth, O., Puranen, A., Evins, L.Z. & Spahiu, K. (2020): Aqueous leaching of ADOPT and standard UO_2 spent nuclear fuel under H_2 atmosphere. MRS Advances 5, 167–175 (2020). https://doi.org/10.1557/adv.2020.69.

Fiedor, J.N., Bostick, W.D., Jarabek, R.J. & Farrell, J. (1998): Understanding the mechanism of uranium removal from groundwater by zero-valent iron using X-ray photoelectron spectroscopy, Environ. Sci. Technol., 32 (1998) 1466-1473. https://doi.org/10.1021/es970385u.

Fors, P., Carbol, P., Van Winckel, S. & Spahiu, K. (2009): Corrosion of high burn-up structured UO_2 fuel in presence of dissolved H_2, Journal of Nucl. Mater. 394, 1-8.

Fors, P. (2009): The effect of dissolved hydrogen on spent nuclear fuel corrosion, Ph. D. Thesis, Chalmers University of Technology, Gothenburg, Sweden.

Gauthier-Lafaye, F., Holliger, P. & Blanc, P.L. (1996): Natural fission reactors in the Franceville basin, Gabon: A review of the conditions and results of a "critical event" in a geologic system, Geochim. Cosmochim. Acta 60(23), 4831-4852.

Giroud, N., Tomonaga, Y., Wersin, P., Briggs, S., King, F., Vogt, T. & Diomidis, N. (2018): On the fate of oxygen in a spent fuel emplacement drift in Opalinus Clay. Appl. Geochem. 97, 270–278. https://doi.org/10.1016/j.apgeochem.2018.08.011.

Gonzalez-Robles, E., Fuss, M., Bohnert, E., Müller, N., Herm, M., Metz, V. & Kienzler, B. (2015): Study of the release of the fission gasess (Xe and Kr) under anoxic conditions in bicarbonate water, Mater. Res. Soc. Symp. Proc. Vol. 1744 © 2015 Materials Research Society DOI: 10.1557/opl.2015. 4.

Gonzalez-Robles, E., Metz, V., Wegen, D.H., Herm, M., Papaioannou, D., Bohnert, E., Gretter, R., Müller, N., Nasyrow, R., de Weerd, W., Wiss, T. & Kienzler, B. (2016): Determination of fission gas release of spent nuclear fuel in puncturing test and in leaching experiments under anoxic conditions, J. Nucl. Materials, 479, 67-75.

Grambow, B., Bruno, J., Duro, L., Merino, J., Tamayo, A., Martin, C., Pepin, G., Schumacher, S., Smidt, O., Ferry, C., Jegou, C., Martinez-Esparza, A., Loida, A., Metz, V., Kienzler, B., Bracke, G., Pellegrini, D., Mathieu, G., Wasselin-Turpin, V., Serres, C., Wegen, D., Jonsson, M., Johnson, L., Lemmens, K., Liu, J., Spahiu, K., Ekeroth, E., Casas, I., de Pablo, J., Watsson, C., Robinson, P. & Hodgkinson, D. (2010): Final activity report: EU-project MICADO (Model uncertainty for the mechanism of dissolution of spent nuclear fuel in a waste repository), 60 p.

Grambow, B., Loida, A., Dressler, P., Geckeis, H., Gago, J., Casas, I., de Pablo, J., Gimenez, J. & Torrero, M.E. (1996a). Long-term safety of radioactive waste disposal: chemical reaction of fabricated and high burnup spent UO_2 fuel with saline brines. Final report. Wissenschaftliche Berichte FZKA 5702, Forschungszentrum Karlsruhe.

Grambow, B., Loida, A., Martinez-Esparza, A., Diaz-Arcoas, P., De Pablo, J., Paul, J-L., Marx, G., Glatz, J-P., Lemmens, K., Ollila, K. & Christensen, H. (2000): Source term for performance assessment of spent fuel as a waste form, European Commission, Nuclear Science and Technology, EUR 19140 EN.

Grambow, B., Vandenborre, J., Suzuki-Muresan, T., Philippini, V., Abdelouas, A., Deniard, P. & Jobic, S., (2017). Solubility equilibrium and surface reactivity at solid/liquid interfaces of relevance to disposal of nuclear waste. J. Chem. Thermodyn. 114, 172-181. https://doi.org/10.1016/j.jct.2017.05.038.

Grambow, G., Smailos, E., Geckeis, H., Müller, R. & Hentschel, H., (1996b). Sorption and reduction of uranium (VI) on iron corrosion products under reducing saline conditions, Radiochimica Acta, 74 (1996) 149-154. https://doi.org/10.1524/ract.1996.74.special-issue.149.

Grandstaff, D.E. (1976): A Kinetic Study of the Dissolution of Uraninite. Econ. Geology 71, 1493-1506. Precambrian Research 13, 1-26.

Grandstaff, D.E. (1980): Origin of uraniferous conglomerates at Elliot Lake, Canada and Witwatersrand, South Africa: Implications for oxygen in the precambrian atmosphere.

Gray W.J., Strachan, D.M. & Wilson, C.N. (1992): Gap and grain boundary inventories of Cs, Tc, and Sr in spent LWR fuel, Mat. Res. Soc. Symp. proc. Vol. 257, pp. 353-360.

Grenthe, I., Gaona, X., Plyasunov, A.V., Rao, L., Runde, W.H., Grambow, B., Konings, R.J.M., Smith, A.L. & Moore, E.E. (2020): Second update on the chemical thermodynamics of uranium, neptunium, plutonium, americium and technetium. Maria-Eleni Ragoussi (Project Co-ordinator and Volume Editor) Jesus S. Martinez and Davide Costa, Eds. Chemical Thermodynamics Vol. 14, OECD Nuclear Energy Agency, Data Bank Boulogne-Billancourt (France).

Grindrod, P., Williams, M., Grogan, H. & Impey, M. (1991): STRENG: A source term model for vitrified high level waste. Nagra Technical Report NTB 90-48.

Gu, B., Liang, L.,Dickey, M., Yin, X. & Dai, S. (1998): Reductive precipitation of uranium (VI) by zero-valent iron, Environ. Sci. Technol., 32 (1998) 3366-3373. https://doi.org/10.1021/es980010o.

Guenther, R., Blahnik, D.E., Campbell, T.K., Jenquin, U.P., Mendel, J.E., Thomas, L.E. & Thornhill, C.K. (1988a): Characterization of spent fuel approved testing material – ATM-103. Pacific Northwest Laboratories Report PNL-5109-103.

Guenther, R., Blahnik, D.E., Campbell, T.K., Jenquin, U.P., Mendel, J.E. & Thornhill, C.K. (1988b): Characterization of spent fuel approved testing material – ATM-106. Pacific Northwest Laboratories Report PNL-5109-106.

Guenther, R., Blahnik, D.E., Jenquin, U.P., Mendel, J.E., thomas, L.E. & Thornhill, C.K. (1991a): Characterization of spent fuel approved testing material – ATM-104. Pacific Northwest Laboratories Report PNL-5109-104.

Guenther, R., Blahnik, D.E., Campbell, T.K., Jenquin, U.P., Mendel, J.E., Thomas, L.E. & Thornhill, C.K. (1991b): Characterization of spent fuel approved testing material – ATM-105. Pacific Northwest Laboratories Report PNL-5109-105.

Guillamont, R., Fanghänel, T., Grenthe, I., Neck, V., Palmer, D. & Rand, M.H. (2003): Update on the chemical thermodynamics of uranium, neptunium, plutonium americium and technetium, OECD-NEA, Chemical Thermodynamics Vol. 5, pp. 182-187, Elsevier.

Guo, X., Szenknect, S., Mesbah, A., Labs, S., Clavier, N., Poinssot, Ch., Ushakov, S.V., Curtius, H., Bosbach, D., Ewing, R.C., Burns, P.C., Dacheux, N. & Navrotsky, A. (2015): Thermodynamics of formation of coffinite, $USiO_4$, PNAS 112, 6551-6555, www.pnas.org/cgi/doi/10.1073/pnas.1507441112

Hanson, B.D. (1998): The burnup dependence of light water reactor spent fuel oxidation, Report PNL-11929, Pacific Northwest National Laboratory, Richland, WA, USA.

Hanson, B. (2008): Examining the conservatisms in dissolution rates of commercial spent nuclear fuel, Proc. 12th Int. High-Level Waste Management Conf., Las Vegas, American Nuclear Society, pp 404-411.

Hanson, B. & Stout, R. (2004): Re-examining the dissolution of spent fuel: A comparison of different methods for calculating rates, Mat. Res. Symp. Proc. Vol. 824, pp.89-94.

Harding J.H. & Pandey R. (1984): Calculation of the oxygen potential in the mixed oxide $(U,Pu)O_{2-x}$, J. Nucl. Mater. 125, pp. 125-137.

Hidaka, H. & Holliger, Ph. (1998) Geochemical and neutronic characteristics of the natural fossil fission reactors at Oklo and Bangombé, Gabon. Geochim. Cosmochim. Acta 62(1), 89-108.

Hidaka, H. (2020): A Review of In Situ Isotopic Studies of the Oklo and Bangombé Natural Fission Reactors Using Microbeam Analytical Techniques. Minerals 10, 1060; doi:10.3390/min10121060.

Hocking, W.H., Duclos, A.M. & Johnson, L. (1994): Study of fission-product segregation in used CANDU fuel by X-ray photoelectron spectroscopy (XPS) II, J. Nucl. Mater. 209, 1-26.

Hofstetter, T.B., Sosedova, Y., Gorski, C., Voegelin, A. & Sander, M. (2014): Redox properties of iron-bearing clays and MX-80 bentonite – electrochemical and spectroscopic characterization, Nagra Technischer Bericht NTB 13-03.

Hummel, W. (2017): Chemistry of selected dose-relevant radionuclides. Nagra Technical Report NTB 17-05.

Hummel, W. & Thoenen, T. (2022): The PSI Chemical Thermodynamic Database 2020. Nagra Technical Report NTB 21-03.

Janeczek, J. & Ewing, R.C. (1995): Mechanisms of lead release from uraninite in the natural fission reactors in Gabon. Geochimica et Cosmochimica Acta. Vol. 59(10), pp. 1917-1931.

Janeczek, J. & Ewing, R.C. (1992): Dissolution and alteration of uraninite under reducing conditions. J. Nucl. Mater. 190, 157-173.

Jeffery, B.M. (1967): Microanalysis of inclusions in irradiated UO2, J. Nucl. Mater. 22, 33-40.

Jenni, A., Wersin, P., Thoenen, T., Baeyens, B., Ferrari, A., Gimmi, T., Mäder, U., Marschall, P., Hummel, W. & Leupin, O. (2019): Bentonite backfill performance in a high-level waste repository: a geochemical perspective. Nagra Technical Report NTB 19-03.

Jegou, C., Caraballo, R., De Bonfils, J., Broudic, V., Peuget, S., Vercouter, T. & Roudil, D. (2010) : Oxidizing dissolution of spent MOX47 fuel subjected to water radiolysis: Solution chemistry and surface characterisation by Raman spectroscopy, J. Nucl. Mater. 399, pp. 68-80.

Jegou, C., Peuget S., Brudic V., Roudil, D., Deschanels, X. & Bart J.M. (2004): Identification of the mechanism limiting the alteration of clad spent fuel segments in aerated carbonated groundwater, J. Nucl. Mater. 326, pp.144-155.

Johnson L.H. & Shoesmith, D.W. (1988): Spent fuel. In: Radioactive Waste Forms for the Future, Eds.: Lutze, W and Ewing, R. C., North-Holland Physics Publishing, The Netherlands, 1988.

Johnson, L. (2014): A model for the release of radionuclides from spent UO_2 and MOX fuel. Nagra Arbeitsbericht NAB 13-37.

Johnson, L. & McGinnes, D.F. (2002): Partitioning of radionuclides in Swiss power reactor fuels. Nagra Technical Report NTB 02-07.

Johnson, L., Ferry, C., Poinssot, C. & Lovera P. (2005): Spent fuel radionuclide source-term model for assessing spent fuel performance in geological disposal. Part I: Assessment of the instant release fraction, J. Nucl. Mater. 346, 56-65.

Johnson, L., Günther-Leopold, I., Kobler Waldis, J., Linder, H.P., Low, J., Cui, D., Ekeroth, E., Spahiu, K. & Evins, L.Z. (2012): Rapid aqueous release of fission products from high burn-up LWR fuel: Experimental results and correlations with fission gas release, J. Nucl. Mater. 420, 55-6.

Johnson, L. & Tait, J.C. (1997): Release of segregated nuclides from spent fuel. SKB TR 9718, Svensk Kärnbränslehantering AB.

Johnson, L. (1982): The dissolution of irradiated UO_2 fuel in groundwater. Report AECL - 6837. Atomic Energy Canada Limited, Pinawa, Manitoba, Canada.

Jonsson, M., Nielsen, F., Roth, O., Ekeroth, E., Nilsson, S. A model for the release of radionuclides from spent UO_2 and MOX fuel. Hossain, M.M. (2007). Radiation induced spent nuclear fuel dissolution under deep repository conditions. Environ. Sci. & Technol., 41, pp 7087-7093.

Kamimura, K. (1992): FP gas release behaviour of high burnup MOX fuels for thermal reactors. Proc. Of Technical Committee Meeting on Fission Gas Release and Fuel Rod Chemistry Related to Extended Burnup, Pembroke, Ontario, Canada, 28 April-1 May 1992, IAEA-TECDOC-697, p. 82.

Kaye, M.H. Lewis, B.J. & Thompson, W.T. (2007): Thermodynamic treatment of noble metal fission products in nuclear fuel, J. Nucl. Mater. 366, 8-27.

Kienzler, B., Duro, L, Lemmens, K., Metz, V., De Pablo, J., Valls, A., Wegen, D.H., Johnson, L. & Spahiu, K. (2017): Summary of the Euratom Collaborative Project FIRST-Nuclides and Conclusions for the Safety Case, Nuclear Technology, (2017).198:3, 260-276.

Kleykamp, H. (1985): The chemical state of the fission products in oxide fuels. Journal of Nuclear Materials, 131, pp 221-246.

Kolár, M. & King, F. (1996): Modelling the consumption of oxygen by container corrosion and reaction with Fe(II). MRS Symp. Proc. 412, pp 547-554.

Kulik D.A., Fernandes M.M. and Baeyens B. (2018): The 2SPNE SC/CE sorption model in GEM-Selektor v.3.4 code package (ClaySor): Implementation, tests, and user guide. Nagra Arbeitsbericht NAB 18-27.

Kulik, D.A., Wagner, Th., Dmytrieva, S.V., Kosakowski, G., Hingerl, F.F., Chudnenko, K.V. & Berner, U. (2013): GEM-Selektor geochemical modeling package: revised algorithm and GEMS3K numerical kernel for coupled simulation codes. Computational Geosciences 17, 1-24.

Lassman, K.A., Schubert, A., van de Laar, J. & Walker, C.T. (2002): On the diffusion coefficient of cesium in UO2 fuel, Fission gas behavior of water reactor fuels, Seminar Proc. 26-29, September 2000, NEA, pp. 321-334

Latta, D.E., Mishra, B, Cook, R.E., Kemner, K.M. & Boyanov, M.I., (2014). Stable U (IV) complexes form at high-affinity mineral surface sites, Environ. Sci. Technol., 48 (2014) 1683-1691. https://doi.org/10.1021/es4047389.

Ledergerber, G., Valizadeh, S., Wright, J., Limbäck, M., Hallstadius, L., Gavillet, D., Abolhassani, S., Nagase, F., Sugiyama, T., Wiesenack, W. & Tverberg, T. (2010): Proceedings of 2010 LWR Fuel Performance/TopFuel/WRFPM, Orlando, Florida, USA, September 26-29, 2010, Paper 0044.

Lemmens, K., Gonzalez-Robles, E., Kienzler, B., Curti, E., Serrano-Purroy, D., Sureda, R., Martínez-Torrents, A., Roth, O., Slonszki, E., Mennecart, T. Günther-Leopold, I., Hozer, Z. (2017): Instant release of fission products in leaching experiments with high burnup nuclear fuels in the framework of the Euratom project FIRST- Nuclides, J. Nucl. Mater.484, 307-323.

Leupin, O.X., Zeyer, J., Cloet, V., Smith, P., Bernier-Latmani, R., Marschall, P., Papafotiou, A., Schwyn, B. & Stroes-Gascoyne, S. (2016): An assessment of the possible fate of gas generated in a repository for low- and intermediate-level waste. Nagra Technical Report NTB 16-05.

Lewis, B.J., Hunt, C.E.L. & Iglesias F.C. (1990): Source term of iodine and noble gas fission products in the fuel-to-sheat gap of intact operating nuclear fuel elements, J. Nucl. Mater. 172 (1990) 197-205.

Liu, N., Qin Z., Nöel J.J. & Shoesmith, D.W. (2017): Roles of radiolytic and externally generated H_2 in the corrosion of fractured spent fuel. J. Nucl. Mater., 494, pp. 87-94.

Liu, N., Wu L., Qin Z. & Shoesmith, D.W. (2016): Roles of radiolytic and externally generated H_2 in the corrosion of fractured spent fuel. Environ. Sci.&Technol. 50, pp. 12348-12355.

Loida, A., Gens, R., Bube, C., Lemmens, K., Cachoir, C., Mennecart, T. & Kienzler, B. (2012) : Corrosion behavior of spent fuel in high pH solutions-Effect of hydrogen, MRS Symp. Proc. 1475 pp. 119-124.

Loida, A., Grambow, B. & Geckeis, H. (2001): Spent fuel corrosion behavior in salt solution in the presence of hydrogen overpressure, Proc. of ICEM'01: The 8th Internat. Conf. on Radioactive Waste Management and Environmental Remediation, Bruges, B, September 30 – October 4, 2001.

Loida, A., Kelm, M., Kienzler, B., Geckeis, H. & Bauer, A. (2006): The effect of near field constraints on the corrosion behaviour of high burnup spent fuel. Mat. Res. Soc. Symp. Proc. Vol. 932, pp. 473-480.

Loida, A., Metz, V., Kienzler, B. & Geckeis, H. (2005): Radionuclide release from high burnup spent fuel during corrosion in salt brine in the presence of hydrogen overpressure. J. Nucl. Mater. 346 pp. 24-31.

Loida, A., Metz, V. & Kinzler, B. (2007): Alteration behavior of high burnup spent fuel in salt brine under hydrogen overpressure and in presence of bromide MRS. Symp. Series, 985 pp. 15-20.

Lumpkin, G.R. & Geisler-Wierwille, Th. (2020): Minerals and Natural Analogs. In: Comprehensive Nuclear Materials, 2nd Edition, R.J.M. Konings and R.E.Stoller Eds., Vol. 6, Section 6.19, pp. 504-536.

Mäder, U. & Wersin, P. (2022): Pore water composition in Opalinus Clay. Nagra Arbeitsbericht NAB 22-47.

Matzke H. (1995): Oxygen potential measurements in high burnup LWR UO_2 fuel, J. Nucl. Mater. 223, 1-5.

Mazurek, M. & de Haller, A. (2017): Pore-water evolution and solute-transport mechanisms in Opalinus Clay at Mont Terri and Mont Russelin (Canton Jura, Switzerland). Swiss J. Geosci. 110, 129-149. DOI 10.1007/s00015-016-0249-9.

McCollom, T.M. & Seewald, J.S. (2001): A reassessment of the potential for reduction of dissolved CO_2 to hydrocarbons during serpentinization of olivine. Geochim. Cosmochim. Acta 65, 3769-3778.

Miron, D. The fate of hydrogen and the effect of microbial acitivity on tunnel backfill (work title). Nagra Arbeitsbericht. In prep.

Mennecart, T., Lemmens, K., Cachoir, C. (2014) : Characterisation and leaching test for the experimental determination of IRF radionuclides from belgian high burnup spent nuclear fuel. In: B. Kinzler, V. Metz, a. Valls (Eds), Final workshop proceedings of the collaborative project "Fast-Instant release of safety relevant nuclides from spent nuclear fuel, KIT Scientific Report 7716, pp.147-156.

Metz, V., Bohnert, E., Kelm, M., Schild, D., Reinhardt, J., Kienzler, B. & Buchmeiser, M. (2007): Gamma-radiolysis of NaCl brine in the presence of UO_2(s): Effects of hydrogen and bromide, MRS. Symp. Proc. 985, pp. 33-40.

Metz, V. (2021): Spent nuclear fuel experiments: Final results of dissolution experiments. DISCO Project, Grant Agreement: 755443, Deliverable D3.3, European Commission, Bruxelles.

Moench, R.H. (1962): Properties and paragenesis of coffinite from the Woodrow mine, New Mexico, Am. Min. 47, 26-33.

Müller-Vonmoos, M. & Kahr, G. (1983): Mineralogische Untersuchungen von Wyoming Bentonit MX-80 und Montigel. Nagra Technischer Bericht NTB 83-12.

Muzeau, B., Jégou, C., Delaunay, F., Broudic, V., Brevet, A., Catalette, H., Simoni, E. & Corbel, C., 2009. Radiolytic oxidation of UO_2 pellets doped with alpha emitters ($^{238/239}$Pu), J. All. Comp. 467, pp. 578-589.

Nagra (2002): Project Opalinus Clay Models, Codes and Data for Safety Assessment. Nagra Technical Report NTB 02-06.

Nagra (2005): Spent fuel evolution under disposal conditions. Synthesis of results from the EU spent fuel stability (SFS) project. Nagra Technical Report NTB 04-09.

Nagra (2014): Modellhaftes Inventar für radioaktive Materialien MIRAM 14. Nagra Technischer Bericht NTB 14-04.

Nagra (2023a): Modellhaftes Inventar für radioaktive Materialien MIRAM RBG. Nagra Technischer Bericht NTB 22-05.

Nagra (2023b): Treatment of ^{14}C in the post-closure safety assessments for SGT Stage 3. Nagra Arbeitsbericht NAB 24-07.

Nagra (2023c): Definition of reference corrosion rates for performance and safety assessments in the framework of the General Licence Application. Nagra Arbeitsbericht NAB 23-22.

Nagra (2024): Design and performance assessment of SF/HLW disposal canisters for RBG. Nagra Technical Report NTB 24-20.

Nakamura, A. & Fujino, T. (1987): Thermodynamic study of UO2+x by solid state EMF technique, J. Nucl. Mater. 149 80-100.

Neeb, K-H. (1997): The Radiochemistry of Nuclear Power Plants with Light Water Reactors, Walter de Gruyter, Berlin-New York.

Neuilly, M., Bussac, J., Frejacques, C., Nief, G., Vendryes, G. & Yvon, J. (1972): Sur l'existence dans un passe reculé d'une reaction en chaine naturelle de fission, dans le gisement d'uranium d'Oklo (Gabon). C.R. Acad. Sci. Paris Série D, tome 275 (23 octobre 1972), 1847-1849.

Newton T.W. (1975): ERDA Critical Review Series, The kinetics of the oxidation-reduction reactions of uranium, neptunium, plutonium and americium in aqueous solutions (TID-26506), NTIS, Springfield VA USA.

Nilsson, K., Roth, O. & Jonsson, M. (2017): Oxidative dissolution of ADOPT compared to standard UO2 fuel, J. Nucl. Mater. 488, 123-128.

Nordström, E. (2009): Fission Gas Release Data for Ringhals PWRs, SKB Technical Report TR 09-26, Svensk Kärnbränslehantering AB, Stockholm, Sweden.

Odorowski, M. (2015): Etude de l'altération de la matrice (U,Pu)O_2 du combustible irradié en conditions de stockage géologique :Approche expérimentale et modélisation géochimique, Ph. D. Thesis, Mines Paris Tech, France.

Odorowski, M., Jegou, C., de Windt, L., Broudic, V., Jouan, G., Peuget, S. & Martin, C. (2017): Effect of metallic iron on the oxidative dissolution of UO2 doped with a radioactive alpha emitter in synthetic Callovo-Oxfordian water, Geochim. Cosmochim Acta 219, pp.1-21.

Odorowski, M., Jegou, C., de Windt, L., Broudic, V., Peuget, S., Magnin, M., Tribet, M. & Martin, C. (2016): Oxidative dissolution of unirradiated Mimas MOX fuel (U/Pu oxide) in carbonated water under oxic and anoxic conditions. J. Nucl. Mater. 468 p. 17-25.

Olander, D.R. (1976): Fundamental aspects of nuclear reactor fuel elements. Technical Report TID-26711-P1, California, Univ. Berkley, USA. https://doi.org/10.2172/7343826.

Oldberg, K. (2009): Distribution of fission gas release in 10 × 10 fuel, SKB Technical Report TR-09-25, Svensk Kärnbränslehantering AB, Stockholm, Sweden.

Olin, Å., Noläng, B., Osadchii, E., Öhman, L. & Rosen E. (2005): Chemical thermodynamics. Vol. 7. Chemical thermodynamics of selenium. Amsterdam: Elsevier.

Ollila, K. (2006): Dissolution of unirradiated UO_2 and UO_2 doped with ^{233}U in 0.01 M NaCl under anoxic and reducing conditions, Posiva Report 2006-08. 87 p. Posiva Oy, Olkiluoto, Finland.

Ollila, K. & Oversby, V.M.M. (2005): Dissolution of unirradiated UO_2 and UO_2 doped with ^{233}U under reducing conditions. SKB TR-05-07, Svensk Kärnbränslehantering AB.

Ollila, K. & Oversby, V.M. (2006): Testing of uranium dioxide enriched with ^{233}U under reducing conditions, MRS Symp. Proc. Vol. 932, pp. 167-173.

Ollila, K. (2008): Dissolution of unirradiated UO_2 and UO_2 doped with ^{233}U in low- and high-ionic-strength NaCl under anoxic and reducing conditions, Posiva Working Report 2008–50. Posiva Oy, Olkiluoto, Finland.

Ollila, K., Albinsson, Y., Oversby, V.M. & Cowper, M. (2003): Dissolution rates of unirradiated UO_2, UO_2 doped with ^{233}U, and spent fuel under normal atmospheric conditions and under reducing conditions using an isotope dilution method, SKB Technical Report TR-03-13, Swedish Nuclear Fuel and Waste Management Co.

O'Loughlin, E.J., Kelly, S.D., Cook, R.E., Csencsits, R. & Kemner, K.M. (2003): Reduction of uranium (VI) by mixed iron (II)/iron (III) hydroxide (green rust): formation of UO_2 nanoparticles, Environ. Sci. Technol., 37 (2003) 721-727. https://doi.org/10.1021/es0208409.

Ozrin, V.D. (2011): A model for evolution of oxygen potential and stoichiometry deviation in irradiated UO2 fuel, J. Nucl. Mater. 419 371-377.

Pan, Z., Bártová, B., LaGrange, T., Butorin, S.M., Hyatt, N.C., Stennett, M.C., Kvashnina, K.O. & Bernier-Latmani, R. (2020): Nanoscale mechanism of UO_2 formation through uranium reduction by magnetite, Nature communications, 11 (2020) 1-12. https://doi.org/10.1038/s41467-020-17795-0

Park, K. & Olander, D.R. (1992): Defect models for the oxygen potentials of gadolinium- and europium-doped urania, J. Nucl. Mater. 187, pp. 89-96.

Park, K. (1994), The oxygen potential of neodymia doped Urania based on a defect structure, J. Nucl. Mater. 209, pp. 259-262.

Pastina. B. & LaVerne, J.A. (2021): An alternative conceptual model for the spent nuclear fuel–water interaction in deep geologic disposal conditions, Appl. Sci., 11, 8566-8586. https://doi.org/10.3390/app11188566. xxx

Piro, M.H.A., Sunderland, D., Livingstone, S., Sercombe, J., Revie, W., Quastel, A., Terrani, K. & Judge, C. (2017): A review of pellet-clad interaction behavior in zirconium alloy fuel cladding, in: Saleen Hashmi (Ed.), Reference Module in Materials Science and Materials Engineering, Elsevier Oxford, pp. 1-68.

Puigdomenech, I., Trotignon, L., Kotelnikova, S., Pedersen, K., Griffault, L., Michaud, V., Lartigue, J-E., Hama, K., Yoshida, H., West, J., Bateman, K., Milodowski, A., Banwart, S., Rivas Perez, J. & Tullborg, E-L., (2000): O_2 consumption in a granitic environment, MRS. Symp. Proc., 608 pp. 179-184.

Puranen, A., Barreiro-Fidalgo A, Evins, L.Z. & Spahiu, K. (2017): Spent fuel leaching in the presence of corroding iron, MRS Advances, Energy &Sustain. 2 (12) pp. 681-686.

Puranen, A., Barreiro-Fidalgo, A., Evins, L.Z. & Spahiu, K. (2020): Spent fuel leaching and the impact of iron corrosion-the effects of hydrogen generation and formation of iron corrosion products. J. Nucl. Mater. 542, paper 152423.

Puranen, A., Evins, L., Barreiro, A., Roth, O. & Spahiu, K. (2022): Very high burnup spent fuel corrosion and leaching under hydrogen conditions, submitted to J. Nucl. Mater., under review.

Puranen, A., Granfors, M. & Roth, O., (2014): Aqueous leaching of Se-79 from spent nuclear fuel, in Final Workshop Proceedings of the Collaborative Project Fast/Instant release of Safety-relevant Radionuclides from Spent Nuclear Fuel, B. Kienzler, V. Metz, A. Valls (eds.) 1-2 Sept. 2104, KIT Scientific Report 7716.

Puranen, A., Roth, O., Evins, L., Spahiu, K. (2018): Aqueous leaching of high burnup UO2 fuel under hydrogen Conditions, MRS Advances © Materials Research Society DOI: 10.1557/adv.2018.273.

Rai, D., Felmy, A.R. & Ryan J.L. (1990): Uranium (IV) hydrolysis constants and solubility product of $UO_2.xH_2O$(am), Inorg. Chem. 19, pp. 260-264.

Rand, M., Fuger, J., Grenthe, I., Neck, V. & Rai, D. (2009): Chemical thermodynamics of thorium, OECD NEA, Paris.

Rest, J., Cooper, M.W.D., Spino, J., Turnbull, J.A., Van Uffelen, P., Walker, C.T. (2019): Fission gas release from UO2 nuclear fuel: A review, J. Nucl. Mater. 513,310-345.

Robinson, P. (2022): STMAN 5: User guide and theoretical background for version 5.10. Nagra Arbeitsbericht NAB 22-10.

Rollin, S., Spahiu, K. & Eklund, U.B. (2001): Determination of dissolution rates of spent fuel in carbonate solutions under different redox conditions with a flow-through experiment. J. Nucl. Mater. 297, 231-243.

Rondinella, V.V., Cobos, J. & Wiss, T. (2004): Leaching behaviour of low-activity alpha-doped UO_2, MRS Symp. Proc. 824, pp. 167-173.

Rondinella, V. & Wiss, T. (2010): The high burnup structure in nuclear fuel, Materials today, 13 pp. 24-32.

Roth, O. & Jonsson, M. (2008): Oxidation of UO_2(s) in aqueous solutions, Centr. Eur. J. Chem. 6, 1-14.

Roth, O., Low, J., Granfors, M. & Spahiu, K., (2013): Effect of matrix composition on instant release fractions from high burn-up fuel, Mater. Res. Soc. Symp. Proc. Vol. 1518, pp. 145-150.

Roth, O., Low, J. & Spahiu, K. (2014): Effects of matrix composition and sample preparation on instant release fractions from high burnup spent fuel, Mater. Res. Soc. Symp. Proc. Vol. 1665, pp. 261-266.

Roth, O., Cui, D., Askeljung, C., Puranen, A., Evins, L.Z. & Spahiu, K. (2019): Leaching of spent nuclear fuels in aerated conditions: Influences of sample preparation on radionuclide release patterns. J. Nucl. Mater. 527, 151789.

Roudil, D., Jégu, C., Broudic, V., Muzeau, B. & Deschanels, X. (2007): Gap and grain boundary inventories from pressurized water reactors spent fuels. J. Nucl. Mater. 362, pp. 411-415.

Santos, B.G., Noel, J.J. & Shoesmith, D.W. (2006): The influence of calcium ions on the development of acidity in corrosion products deposits on SIMFUEL, UO_2, J. Nucl. Mater. 350 pp. 320-331.

Scott T., Allen G., Heard, P. & Randell, M. (2005): Reduction of U (VI) to U (IV) on the surface of magnetite, Geochim. Cosmochim. Acta, 69 (2005) 5639-5646. https://doi.org/10.1016/j.gca.2005.07.003.

Senger R., Papafotiou, A. & Marschall, P. (2014): Thermo-hydraulic simulations of the near-field of a SF/HLW repository during early- and late-time post-closure period. Nagra Arbeitsbericht NAB 14-11.

Shoesmith, D.W. (2013): The chemistry/electrochemistry of spent nuclear fuel as a waste form, Chapter 11 in: Burns, P.C., Simon, G.E. (Eds.), “Uranium: Cradle to Grave”, Mineralogical Society of Canada, Quebec.

Shoesmith, D.W. (2007): Used fuel and uranium dioxide dissolution studies- a review, NWMO TR-2007-03, 22 St. Clair Avenue East Fourth Floor, Toronto, ON M4T 2S3, Canada.

Shoesmith, D.W. (2000): Fuel corrosion processes under waste disposal conditions. J. Nucl. Mater. 282 pp. 1-31.

Shoesmith, D.W., Sunder S., Johnson L.H. & Bailey M.G. (1985): Oxidation of CANDU fuel by the alpha radiolysis products of water, MRS. Symp. Proc. 50, pp. 309-316.

SKB (2010a): Fuel and canister process report for the safety assessment SR-Site, SKB-TR-10-46.

SKB (2010b): Data report for the safety assessment SR-Site, SKB Technical Report TR-10-52.

Smellie, J. & Karlsson, F. (1996): A reappraisal of some Cigar Lake issues of importance to performance assessment, SKB Technical Report TR-96-08. SKB, Stockholm, Sweden.

Spahiu, K. (2021): Spent fuel as a waste form. State of the knowledge report (SoK), EURAD, Spent Nuclear Fuel Domain 3.1.1.

Spahiu, K., Cui, D. & Lündström, M. (2004): The fate of radiolytic oxidants during spent fuel leaching in the presence of dissolved near field hydrogen, Radiochim. Acta 92, 625-629.

Spahiu, K., Werme, L. & Eklund, U.-B. (2000): The influence of near field hydrogen on actinide solubilities and spent fuel leaching, Radiochim. Acta 88 pp. 507-511.

Spahiu, K., Eklund, U.B., Cui, D. & Lundstrom, M. (2002): The influence of near field redox conditions on spent fuel leaching. In Scientific Basis for Nuclear Waste Management XXV; McGrail, B.P., Cragnolino, G.A., Eds.; Materials Research Soc: Warrendale, PA, USA, 2002; Volume 713, pp. 633-638.

Spinks, J.W.T. & Woods, R. J. (1990): An introduction to radiation chemistry. Third edition, New York: John Wiley & Sons Inc.

Stroes-Gascoyne, S., Lucht, L.M., Borsa, J., Delaney, T.L., Haveman, S.A. & Hamon, C.J. (1995): Radiation resistance of the natural microbial population in buffer materials. Mat. Res. Soc. Symp. Proc. Vol. , 353**,** 345-352**.**

Stroes-Gascoyne, S., Tait, J.C., Porth, R.J., Mcconnell, J.L. & Lincoln, W.J. (1994): Release of ^{14}C from the gap and and grain-boundary regions of used CANDU fuels to aqueous solutions. Waste Management 14, 385-392.

Szenknect, S., Mesbah, A., Cordara, T., Clavier, N., Brau, H. P., Le Goff, X., Poinssot, C., Ewing, R.C. & Dacheux, N. (2016): First experimental determination of the solubility constant of coffinite, Geochim. Cosmochim. Acta, 18136-53.

Szenknect S., Alby D., López García M., Wang C., Podor R., Miserque F., Mesbah A., Duro L., Zetterström Evins L., Dacheux N., Bruno J. & Ewing R.C. (2020): Coffinite formation from UO_{2+x}. Scientific Reports, 10:12168, https://doi.org/10.1038/s41598-020-69161-1.

Tait, J.C., Cornett, R.J.J., Chant, L.A., Jirovec, J., Mcconnell, J. & Wilkin, D.L. (1997): Determination of Cl impurities and 36Cl instant release from used CANDU fuels, Mat. Res. Soc. Symp. Proc. 465, 503-510, Materials Research Society, Pittsburgh, PA.

Tait, J.C. & Luht, J.M. (1997): Dissolution rates of uranium from unirradiated UO_2 and uranium and radionuclides from used CANDU fuel using a single pass flow-through apparatus, Ontario Hydro Report No. 06819-REP-01200-006-ROO.

Thom, J. & Anderson, G.M. (2008): The role of thermochemical sulfate reduction in the origin of Mississippi Valley-type deposits. I. Experimental results. Geofluids 8, 16-26.

Thomas, L.E, Beyer, C.E & Charlot, L.A, (1992): Microstructural analysis of LWR spent fuels at high burnup. Journal of Nuclear Materials, 188, pp 80-89.

Thompson, W.T., Lewis, B.J. Piro, M.H. Corcoran, E.C. Kaye, M.H., Higgs, J.D., Akbari, F. & Thompson, D.M. (2012): RMC Fuel Thermochemical Treatment, an online appendix to B.J. Lewis, W.T. Thompson, F.C. Iglesias, Fission Product Chemistry in Oxide Fuels in: R.J.M. Konings (Eds.), Comprehensive Nuclear Materials, Elsevier Ltd..

Truche, L., Berger, G., Destrigneville C., Pages, A., Guillaume, D., Giffaut, E. & Jacquot, E. (2009): Experimental reduction of aqueous sulphate by hydrogen under hydrothermal conditions: Implication for the nuclear waste storage. Geochim. Cosmochim. Acta 73, 4824-4835.

Trummer, M., Nillson, S, & Jonnsson, M. (2008): On the effects of fission product noble metal inclusions on the kinetics of radiation induced dissolution of spent nuclear fuel. J. Nuc, Mater. 378, pp. 55-59.

Trummer, M., Roth, O. & Jonnsson, M. (2009): H2 inhibition of radiation induced dissolution of spent nuclear fuel. J. Nuc. Mater. 383(3): pp. 226-230.

Trummer, M. & Jonsson, M. (2010): Resolving the H_2 effect on radiation induced dissolution of UO_2-based spent nuclear fuel. J. Nucl. Mater. 396, 163-169. https://doi.org/10.1016/j.jnucmat.2009.10.067.

Une K., Tominaga Y., Kashibe S. (1991): Oxygen Potentials and Lattice Parameter of Irradiated BWR Fuels, J. Nucl. Sci. Technol. 28(5), 409–417.

Une, K. & Oguma, M. (1983): Oxygen potentials of $(U,Nd)O_{2\pm x}$ solid solutions in the temperature range 1000 – 1500 °C, J. Nucl. Mater. 118 189-194.

Utsunomiya, S. & Ewing, R.C. (2006): The fate of the epsilon phase (Mo-Ru-Pd-Tc-Rh) in the UO_2 of the Oklo natural fission reactors. Radiochim. Acta 94, 749-753, DOI 10.1524/ract.2006.94.9.749.

Van Loon, L.R., Glaus, M.A. & Müller, W. (2007): Anion exclusion effects in compacted bentonites: towards a better understanding of anion diffusion. Appl. Geochem. 22, 2536-2552.

Waber, N., Schorscher, H.D. & Peters, T. (1990): Mineralogy, petrology and geochemistry of the Poços de Caldas analogue study sites, Minas Gerais, Brazil. I: Osamu Utsumi uranium mine, Technical Report NTB 90-20, Nagra, Wettingen, Switzerland and TR-90-11, Swedish Nuclear Fuel, Waste Management Co (SKB), Stockholm, Sweden.

Walker, C.T., Rondinella, V.V., Papaioannou, D., Van Winckel, S., Goll, W. & Manzel R. (2005): On the oxidation state of UO2 nuclear fuel at a burn-up of around 100 MWd/kgHM, J. 1244 Nucl. Mater. 345, 192-205.

Walker, C.T., Bagger, C. & Mogensen, M. (1996): Observations on the release of cesium from UO_2 fuel, J. Nucl. Mater. 240, 32-42.

Wang, Y. & Xu, H. (1999): Proceedings of the ICEM ’99conference , Nagoya (JP), 26-30 September 1999, Report SAND99-2626C, Sandia National Lab.

Werme L.O. & Spahiu, K., (1998): Direct disposal of spent nuclear fuel: comparison between experimental and modelled actinide solubilities in natural waters. J. Alloys and Compounds, 271-273, pp.194-200.

West, J.M., Vialta, A. & McKinley, I.G. (1990): Microbiological analysis at the Osamu Utsumi mine and Morro do Ferro analogue study sites, Poços de Caldas, Brazil. Nagra Technical Report NTB 90-28.

Wilson, C.N. (1987): Results from Cycles 1 and 2 of NNWSI Series 2 Spent Fuel Dissolution Tests, HEDL-TME 85-22 UC-70, Westinghouse Hanford Company.

Wilson, C.N. (1990): Results from NNWSI series 2 bare fuel dissolution tests. Report PNL-7169, Pacific Northwest Laboratories, Richland WA (1990).

Wilson, C.N. & Shaw, H.F. (1987): Experimental study of the dissolution of spent fuel at 85 °C in natural groundwater. In Scientific Basis for Nuclear Waste Management X, (J.D. Bates and W.B. Seefeldt, Editors), Mat. Res. Soc. Symp. Proc., Boston, USA, 1986. 84, 123-130.

Wilson, C.N. (1990): Results from Nevada Nuclear Waste Storage Investigation (NNWSI series 3 bare fuel dissolution tests, Pacific Northwest Laboratories Report PNL-7170, Richland WA.

Wren, J.C., Shoesmith, D.W. & Sunder, S. (2005): Corrosion behaviour of uranium dioxide in alpha radiolytically decomposed water. J. Electrochem. Soc. 152: B470-B481.

Wu, L., Beauregard, Y., Qin, Z., Rohani, S. & Shoesmith, D.W. (2012): A model for the influence of steel corrosion products on nuclear fuel corrosion under permanent disposal conditions. Corrosion Science, 61, 83-91.

Wu, B., Bonnetti, Ch., Liu, Y., Zhang, Z.-S., Guo, G.-L., Li, G.-L, Hu,Y.-Q & Yan, Z.-Y. (2021): Uraninite from the Guangshigou Pegmatite-Type Uranium Deposit in the North Qinling Orogen, Central China: Its Occurrence, Alteration and Implications for Post-Caledonian Uranium Circulation. Uraninite from the Guangshigou Pegmatite-Type Uranium. Minerals 11, 729. https://doi.org/10.3390/min11070729.

Zehavi, D. & Rabani, J. (1972): Oxidation of aqueous bromide ion by hydroxyl radicals. Pulse radiolytic investigation, J. Phys. Chem. 76 pp. 312-319.

Zetterström-Evins, L., Juhola, P. & Vahanen, M. (2014): REDUPP Final Report; Posiva Working Report 2014-12, Posiva Oy: Eurajoki, Finland, 2014.

Zwicky, H.U. (2008): Isotopic data of sample F3F6 from a rod irradiated in the Swedish boiling water reactor Forsmark 3. In: Compilation of data in support of the OECD/NEA expert group on assay data of spent nuclear fuel and the spent fuel isotopic composition Database SF Compo. Remingen, Switzerland.

App. A Derivation of the fission gas release for NPP Mühleberg

The complete distribution of FGR for fuel assemblies from Mühleberg has not been modelled as indicated in chapter 2.3.2.4. However, the average burn-up of Mühleberg fuel assemblies is about 47 MWd/kgU and it is known that the fuel assemblies at Mühleberg are the same as the ones used at Leibstadt. Since both FGR and IRF are correlated with LHP (see Section 2 and Fig. 2-8), this report aims to quantify LHP in NPP Mühleberg and use it to select an appropriate analogy, for which FGR and IRF are already known.

A.1 Linear Heat Power

Linear Heat Power (LHP) is merely the thermal power generated by the fuel per unit length (thus having units of W/m). This quantity is typically defined when applying the heat conduction equation to the fuel (Duderstadt and Hamilton, 1976), as it leads to the solution for the temperature drop across the fuel ΔT_{FUEL} (defined as the difference between the centerline fuel temperature and surface temperature), which is independent of the fuel rod radius and is only dependent on LHP (q') and the thermal conductivity of the fuel (k_F):

$$\Delta T_{FUEL} = \frac{q'}{4\pi\,\overline{k_F}} \tag{A.1}$$

This expression for the temperature drop across the fuel makes LHP a useful core parameter, though it should be noted that eq. A.1 assumes uniform heat generation (q' within the fuel from Duderstadt and Hamilton, 1976).

The thermal conductivity of the fuel k_F is strongly dependent of temperature, hence eq. A.1 refers to the *average* thermal conductivity, defined as:

$$\overline{k_F} \equiv \frac{1}{T_{CL}-T_{surf}} \int_{T_{surf}}^{T_{CL}} dT\; k_F(T) \tag{A.2}$$

Here, T_{CL} refers to the centerline temperature and T_{surf} refers to the fuel surface temperature.

During steady-state operation of the reactor at a given (three-dimensional) power distribution in the core, $\overline{k_F}$ is constant (as both T_{CL} and T_{surf} are steady state) and typically equal to 0.02 – 0.03 W/cm·K for UO_2 ceramics. However, it is important to note that the value changes with fuel burnup as a result of the material changes within the fuel.

These equations provide the basis for one-dimensional (radius being the only spatial dimension) thermal conductivity analysis, as it is taught in reactor analysis textbooks (Duderstadt and Hamilton, 1976). However, in reality, the power generation is not constant. Axially, each fuel rod features an (approximately sinusoidal) power distribution. Furthermore, there is a power distribution between individual fuel assemblies, affected by their position in the core, enrichment, burnup, and control rod operation. This results in a complex three-dimensional distribution of power, and thus also LHP, in the core.

The core-average LHP can be calculated using easy to obtain (and often publicly available) parameters:

$$\overline{q'} = \frac{Q_{core}}{N_{FA}\cdot N_{rods}\cdot \overline{l_{rod}}} \tag{A.3}$$

Here, Q_{core} is the total thermal power of the core in [MW], N_{FA} is the number of fuel assemblies [-], N_{rods} is the (average) number of fuel rods per assembly [-], and $\overline{l_{rod}}$ is the average length of fuel rods [m]. The denominator represents the total length of active fuel, producing heat. For boiling water reactors (BWR), it is important to consider the presence of partial length rods, as they affect the average fuel rod length.

However, the correlations between LHP and FGR – such as in the study from Oldberg (2009) for the definition of the analog NPP – typically consider the *maximum* LHP instead, the determination of which would require the knowledge of the three-dimensional power distribution in the core.

Since the detailed power distribution is not available, this work compares the core-average LHP values based on publicly available data, assuming that that the power distribution is similar in the considered NPP. That is, the ratio between the core-average LHP values for two NPPs is assumed to be the same as the ratio between their maximum LHP values.

A.2 Analog NPP

While the FGR and IRF are correlated to LHP, the relationship is not linear. For example, the IRF shown in Fig. 4-7 and Fig. 4-8 features an *elbow* – a point at which the gradient changes. This makes extrapolation challenging and undesirable, especially when going beyond the elbow point.

Instead, this work aims to determine the LHP in NPP Mühleberg and find an analog NPP (same reactor type), which has a similar LHP, but for which the FGR and IRF are known. For this purpose, the FGR release study from Oldberg (2009) is used, in which the fuel from Leibstadt NPP Leibstadt, Oskarshamn-1 (O1), and Oskarshamn-3 (O3) is evaluated. During its lifetime, O3 was uprated from 3'292 MW_{th} to 3'900 MW_{th}. This affects the LHP, as the same length of fuel rods is now producing more thermal power. The SKB study considers both power ratings. Only NPP Leibstadt and O3 will be considered here.

The LHP reported in Oldberg (2009) refers to maximal values. Using the assumption introduced in the last section, a comparison on the basis of average LHP can be made. However, these values must first be calculated – using eq. A.3 – for the NPPs in question.

For O3, the thermal power is taken directly from Oldberg (2009), the number of fuel assemblies and the active core height are taken from Nilsson (2007). For NPP Leibstadt (KKL), the thermal power and active core height are taken from Oldberg (2009), the number of fuel assemblies is taken from the webpage of Leibstadt. For NPP Mühleberg (KKM), all parameters are taken from Bykov (2014). The LHP is calculated for GNF2 and GE14 fuel assembly types. For all plants, the description of fuel assembly types – including the number and length of the partial length rods – is taken from Nuclear Engineering International (2019).

Using these values and eq. 3, the core-average LHP was calculated. This is summarized in Tab. A-1.

Tab. A-1: Core-average linear heat power for different NPPs and FA types

NPP	**Thermal power** [MW]	**FA Design**	**Average linear power** [kW/m]
KKM	1'097	GE14	13.98
KKM	1'097	GNF2	14.17
O3	3'292	SVEA96Op2	14.10
O3	3'900	SVEA96Op2	16.39
KKL	3'600	SVEA96Op2	16.08

It can be seen that the core-average LHP for O3 running at 3'292 MWth (cases 2 and 4 in Oldberg, 2009) is very close to the LHP in KKM with both FA types. As such, their maximum LHP values are comparable, and the FGR and IRF values determined for O3 (at this power) should also be applicable to KKM.

Therefore, it can be concluded that KKM was operated at at approximately 12% lower average linear power ratings than those at Leibstadt. Therefore, the adoption of the average FGR of Leibstadt fuel of 4% would be expected to be an overestimate for Mühleberg fuel. This can be confirmed by comparing the LPR values of fuel assemblies at Mühleberg to the LPR values for Cases 2 and 4 in Oldberg (2009), which are for fuel assemblies from the Oskarshamn 3 reactor. This comparison demonstrates that the LPR values for fuel assemblies are the same for Mühleberg and Oskarshamn 2 and 4 cases. From the results it can be concluded that the average FGR of Mühleberg fuel assemblies would be 2.5 to 3.5%, thus a value of 3% is assumed.

A.3 References

Bykov, V. (2014): “Enhancement and validation of the NPP Mühleberg MCNP activation simulations for Swiss decommissioning planning.” MSc Thesis. ETH Zurich. DOI: 10.3929/ethz-a-010261946.

Duderstadt, J. J. & Hamilton, E. (1976): Nuclear Reactor Analysis. John Wiley & Sons, Inc., January 1976. ISBN: 0-471-22363-8.

Nilsson, L. (2006): "2007:05 Development of an Input Model to MELCOR 1.8.5 for Oskarshamn 3 BWR.” SKI. Issue: December.

Oldberg, K. (2009): Distribution of fission gas release in 10 × 10 fuel, SKB Technical Report TR-09-25, Svensk Kärnbränslehantering AB, Stockholm, Sweden.

Entergy Nuclear Operations, Inc.: Appendix E. Letter to USNRC. BVY 14-009. URL: https://www.nrc.gov/docs/ML1408/ML14080A141.pdf.

URL: https://www.stralsakerhetsmyndigheten.se/en/publications/reports/safety-at-nuclear-power-plants/2007/200705/.

Leibstadt Nuclear Power Plant: “Technical Description”. URL: https://www.kkl.ch/fileadmin/seiteninhalt/Dateien/01_Unternehmen/E_Publikationen/technische_beschreibung_kkl_en.pdf.